A Numerical Method for the Prediction of Combustion Instabilities

Daniel Fredrich

Imperial College London
Department of Mechanical Engineering
Exhibition Road
London, SW7 2AZ

Submitted in part fulfilment of the requirements for the degree of
Doctor of Philosophy in Mechanical Engineering of Imperial College London
and the Diploma of Imperial College London

January 2020

Declarations

Copyright

Originality

I hereby declare that except where specific reference is made to the work of others, the contents of this thesis are original and have not been submitted in whole or in part for consideration for any other degree or qualification in this, or any other university. This thesis is my own work and contains nothing which is the outcome of work done in collaboration with others, except as specified in the text and Acknowledgements.

Daniel Fredrich
January 2020

Für Frank, Ilona und Lena.

Acknowledgements

I would like to thank my supervisor W.P. Jones for giving me the opportunity to pursue a Ph.D. in London. His guidance and support throughout made this work possible. Special thanks to A.J. Marquis for his invaluable technical and personal advice that helped keep me going over the past 4 years and to V.N. Prasad without whom I never would have started this adventure. I would like to acknowledge Siemens Industrial Turbomachinery Ltd. for the project funding and the UKCTRF for providing computational time on the ARCHER UK National Supercomputing Service through Grant no. EP/K026801/1 and EP/R029369/1.

Furthermore, I am very grateful to my (ex-)colleagues and good friends Fabian, Fabien, Paul, Dongwon, Panos, Steven, Amira, Timothy, Gareth, Stathis, Aliki, Azur and everyone else from the offices 220 and 674/675 for keeping me sane and making my time in London so worthwhile. A big thank you to the Tresette society members Simon, Thomas, Giovanni, Hugo and Georgia (Hon.) for our regular meetings and everything else. Thanks also to the Men's 1st Basketball Team and the rest of the Imperial Basketball society, as well as the Silverton crew - Ines, Clara, David, Cyprien, Heather, Annie, Michael and Michelle (Hon.) - for putting up with me and my often nocturnal working habits.

Last but not least, I cannot express how grateful I am to my parents and my sister for their constant support and unconditional love.

Related work

Journal papers

Fredrich, D., Jones, W. P., and Marquis, A. J. (2020). Prediction of longitudinal and azimuthal instabilities in a gas turbine combustor. *Proc. Combust. Inst.* In review.

Fredrich, D., Jones, W. P., and Marquis, A. J. (2020). Self-excited thermo-acoustic and hydrodynamic instabilities in gas turbines. *Combust. Flame* In review.

Fredrich, D., Jones, W. P., and Marquis, A. J. (2020). Thermo-acoustic instabilities in the PRECCINSTA combustor investigated using a compressible LES-pdf approach. *Flow, Turbul. and Combust.* In review.

Fredrich, D., Jones, W. P., and Marquis, A. J. (2019). The stochastic fields method applied to a partially premixed swirl flame with wall heat transfer. *Combust. Flame*, 205:446–456.

Fredrich, D., Jones, W. P., and Marquis, A. J. (2019). Application of the Eulerian subgrid Probability Density Function method in the Large Eddy Simulation of a partially premixed swirl flame. *Combust. Sci. Technol.*, 191(1):137–150.

Noh, D., Karlis, E., Navarro-Martinez, S., Hardalupas, Y., Taylor, A., Fredrich, D., and Jones, W. (2019). Azimuthally-driven subharmonic thermoacoustic instabilities in a swirl-stabilised combustor. *Proc. Combust. Inst.*, 37(4):5333–5341.

Conference papers

Fredrich, D., Jones, W. P., and Marquis, A. J. (2019). Thermo-acoustic instabilities in the PRECCINSTA combustor investigated using a compressible LES-pdf approach. *11th Mediterranean Combustion Symposium (MCS)*, 16-20 June, Tenerife, Spain.

Fredrich, D., Jones, W. P., and Marquis, A. J. (2019). LES-pdf Simulation of Combustion Dynamics in a Partially Premixed Swirl Combustor. *9th European Combustion Meeting (ECM)*, 14-17 April, Lisbon, Portugal.

Fredrich, D., Jones, W. P., and Marquis, A. J. (2018). Large Eddy Simulation of an Oscillating Flame using the Stochastic Fields Method. *12th International ERCOFTAC Symposium on Engineering Turbulence Modelling and Measurements (ETMM)*, 26-28 September, Montpellier, France.

Fredrich, D., Jones, W. P., and Marquis, A. J. (2017). Application of the Eulerian subgrid Probability Density Function method in the Large Eddy Simulation of a partially premixed swirl flame. *10th Mediterranean Combustion Symposium (MCS)*, 17-21 September, Naples, Italy.

Fredrich, D., Gallot-Lavallée, S., Jones, W. P., and Marquis, A. J. (2017). Large Eddy Simulation of a Gas Turbine Model Combustor using the Eulerian Subgrid Probability Density Function Method. *8th European Combustion Meeting (ECM)*, 18-21 April, Dubrovnik, Croatia.

Abstract

This thesis describes one of the first computational works to investigate the physical feedback mechanisms associated with self-excited, combustion-driven instabilities in gas turbines. For this purpose, a novel numerical method based on large eddy simulation is devised. The method (called BOFFIN) uses a fully compressible formulation to account for acoustic wave propagation and applies a transported probability density function approach for turbulence-chemistry interactions. The latter is solved by the Eulerian stochastic fields method and is complemented by two different 15-step / 19 species chemical reaction schemes. This approach is shown to be flame burning regime independent and therefore highly applicable in the context of partially premixed gas turbine combustion.

Combustion instabilities are a phenomenon often encountered in the late design stages of modern gas turbine combustors. Under certain conditions, these types of instabilities can develop into sustained limit-cycle oscillations with potentially severe consequences on a combustor's operating behaviour. In order to study the various physical feedback mechanisms driving such limit-cycle oscillations, two different test cases are simulated in the present work. Firstly, the combined effects of thermo-acoustic and hydrodynamic instabilities are examined in the lab-scale PRECCINSTA model combustor. Secondly, the superposition of a longitudinal and azimuthally spinning instability mode is investigated in the industrial SGT-100 combustor.

Amongst the different feedback mechanisms identified and studied in these cases are: mass flow rate and equivalence ratio oscillations, as well as hydrodynamic phenomena such as flame angle oscillations, periodic vortex shedding and a precessing vortex core. It is further demonstrated that in addition to reproducing longitudinal instability modes, the applied LES approach is capable of accounting for modes acting in the transverse direction. Overall, the findings of this research project strongly suggest that BOFFIN is a reliable and accurate method for the prediction of self-excited combustion instabilities in gas turbines.

Table of contents

List of figures

List of tables

Nomenclature

Roman letters, upper case

A_r	pre-exponential constant of reaction r
C_{1-5}	coefficients 1-5
C_d	*sgs* micro-mixing constant
C_p	heat capacity at constant pressure
C_s	Smagorinsky parameter
C_v	vortex strength
D	diffusivity
$E_{a,r}$	activation energy of reaction r
F	fuel
FI	flame index
$\mathcal{F}$	joint *pdf*
G	filter function
$J_{h,i}$	heat diffusion flux
$J_{\varphi,i}$	species diffusion flux
L	length dimension
L_x	characteristic size
Le	Lewis number
Ma	Mach number
$\mathcal{M}$	average Mach number
N	number of stochastic fields
N_r	number of elementary reactions
N_s	number of scalars
N_{sp}	number of chemical species
Ox	oxidiser
P	products
P_α	fine-grained one-point *pdf* of α
Pr	Prandtl number

$\widetilde{P}_{sgs}$	filtered joint *sgs pdf*
P_{th}	thermal power
R	specific gas constant
R^0	universal gas constant
Re	Reynolds number
R_n	burner nozzle equivalent radius
R_p	pressure pulse characteristic dimension
R_v	vortex radius
S	swirl number
T	temperature
T_{ad}	adiabatic flame temperature
T_∞	far-field temperature
$\mathbb{T}$	transverse term
T_0	reference temperature
U_∞	bulk flow velocity
W	mean molar mass of a mixture
$dW_i^n(t)$	Wiener process of the n-th field
X_φ	mole fraction of φ
Y_φ	mass fraction of φ

Roman letters, lower case

c	speed of sound
e_{ij}	rate of strain tensor
f	general function
f	frequency
g_j	body forces per unit volume
h	height
h_s	(static) enthalpy
h_t	total enthalpy
Δh_φ^0	species formation enthalpy
k	axial wave number
k_r	reaction rate coefficients
m	azimuthal wave number
$\dot{m}$	mass flow rate
m_φ	mass of φ
n	total number of moles

n_φ	specific mole number of φ
p	pressure
p_∞	far-field pressure
p^*	normalised pressure
p_0	reference pressure
$\dot{q}$	heat release rate
r	radial distance or component
r_r	reaction rate
t	time
t_p	oscillation period
u_x	axial velocity component
u_θ	azimuthal velocity component
u_i	velocity in i-direction
$\mathbf{x}$	spatial location
x	axial component (cylindrical coordinates)
x_i	spatial coordinate in i-direction
y^+	dimensionless wall distance

Greek letters, upper case

Δ	filter width
Ω	computational domain
Φ	equivalence ratio
Ψ	stream function
Θ	viscous dissipation
Υ'	flow disturbance quantity
$\check{\Upsilon}_m$	azimuthal disturbance amplitude

Greek letters, lower case

α	scalar
α_p	pressure relaxation coefficient
β_r	temperature exponent of reaction r
β_t	transverse damping parameter
δ	Dirac-function
δ_a	pressure pulse amplitude
δ_{ij}	Kronecker delta

η_i^n	dichotomic random vector of the *n*-th field
η_p	pressure relaxation factor
γ	isentropic expansion factor
λ	thermal conductivity
μ	dynamic viscosity
$\nu_{\varphi,r}$	molar stoichiometric coefficients in reaction *r*
ω	disturbance frequency
$\dot{\omega}_\alpha$	scalar source term
$\dot{\omega}_h$	enthalpy source term
$\dot{\omega}_\varphi$	chemical source term
ϕ	general scalar
ϕ_α	α-th general scalar
φ	species
ψ_α	sample space of α
ρ	density
σ	Schmidt number
τ_{ij}	viscous stress tensor
τ_{sgs}	*sgs* micro-mixing time scale
θ	azimuthal component
$\upsilon_{F/Ox/P}$	coefficients for fuel/oxidiser/products
ξ_α^n	*n*-th stochastic field of α

Sub- and superscripts

ad	adiabatic
ax	axial
α	α-th scalar
b	backward
f	forward
h	enthalpy
ht	heat transfer
i,j,k	i,j,k-direction
n	*n*-th stochastic field
φ	φ-th species
r	chemical reaction
rad	radial
sgs	sub-grid scale

t	transverse j,k-direction
tot	total

Operators

$\bar{\cdot}$	spatial filter
$\tilde{\cdot}$	Favre filter
$\hat{\cdot}$	steady-state solution or time average
$\cdot'$	perturbation or fluctuation
$\nabla\cdot$	nabla operator
$\langle\cdot\rangle$	time-averaged value
$\lvert\cdot\rvert$	absolute value
$\lvert\lvert\cdot\rvert\rvert$	Frobenius norm

Acronyms / Abbreviations

3D	Three-Dimensional
AP	Air Plenum
ARM	Augmented Reduced Mechanism
BOFFIN	Boundary-Fitted Flow Integrator
CC	Combustion Chamber
CDS	Central Difference Scheme
CFD	Computational Fluid Dynamics
CH_4	Methane
C-N	Crank-Nicholson
CO_2	Carbon Dioxide
CO	Carbon Monoxide
CPUh	Central Processing Unit Hours
CVC	Central Vortex Core
DLE	Dry Low Emissions
DLR	German Aerospace Center
DMD	Dynamic Mode Decomposition
DNS	Direct Numerical Simulation
E-M	Euler-Maruyama
EU	European Union
EVC	Exit Vortex Core
FDF	Flame Describing Function

FTF	Flame Transfer Function
FVM	Finite Volume Method
H_2	Hydrogen
H_2O_2	Hydrogen Peroxide
HO_2	Hydroperoxyl
HRR	Heat Release Rate
IEA	International Energy Agency
IRZ	Inner Recirculation Zone
ISL	Inner Shear Layer
JANAF	Joint-Army-Navy-Air-Force
LDV	Laser Doppler Velocimetry
LES	Large Eddy Simulation
LMSE	Linear Mean Square Estimation
MPI	Message Passing Interface
NO	Nitric Oxide
NO_x	Nitrogen Oxides
NSCBC	Navier-Stokes Characteristic Boundary Conditions
O_2	Oxygen
OH	Hydroxide
OH*	Hydroxyl Radical
ORZ	Outer Recirculation Zone
OSL	Outer Shear Layer
sdes	Stochastic Differential Equations
pdf	Probability Density Function
$Ph_{1\text{-}8}$	Phases 1-8
PIV	Particle Image Velocimetry
PLIF	Planar Laser-Induced-Fluorescence
POD	Proper Orthogonal Decomposition
PRECCINSTA	Prediction And Control Of Combustion Instabilities In Industrial Gas Turbines
PSD	Power Spectral Density
PVC	Precessing Vortex Core
QSS	Quasi-Steady-State
Raman	Laser Raman Scattering
RANS	Reynolds-Averaged Navier-Stokes
RMS	Root Mean Square

SAS	Scale-Adaptive Simulation
sgs	Sub-Grid Scale
SGT	Siemens Gas Turbine
TurChemi	Turbulence And Chemistry Interaction
TVD	Total Variation Diminishing
URANS	Unsteady Reynolds-Averaged Navier-Stokes

Chapter 1

Introduction

Chapter 1 introduces the basic principles of combustion-driven instabilities in gas turbines and touches on the background and motivation for ongoing research efforts in this field. The highly complex physical mechanisms associated with such instabilities, as well as state-of-the-art modelling strategies applied to study them, are discussed thereafter. Finally, the main objectives of the present work are specified and the thesis structure is outlined.

1.1 Background and motivation

Today's provision of a reliable and environmentally friendly energy supply has become a pre-eminent challenge as the global energy demand remains subject to continuous growth[1]. Meanwhile, fossil resources are projected to face limited availability in the foreseeable future and the international view on sustainable power generation is experiencing a considerable shift. This has widely led to stricter government policies and legislation concerning the regulation of pollutant and noise emissions, combined with large-scale subsidies promoting the deployment of new technologies such as electric cars. Yet, despite substantial investment efforts into the exploitation of renewable energy sources, coverage of the rapidly growing energy demand continues to rely heavily on the combustion of fossil fuels[2]. Ongoing research and development activities are therefore inevitable to reduce the fuel consumption and emissions of modern carbon-based power generation devices without compromising their overall efficiency and costs. In order to cope with these highly ambitious goals, the physical nature of combustion needs to be understood to a better extent.

---

[1] IEA, World Energy Outlook 2018. https://www.iea.org/weo2018/

[2] IEA, Global Energy & CO2 Status Report 2018. https://www.iea.org/geco/

The work carried out as part of this thesis aims at devising an accurate computational tool capable of facilitating the design process of low-emission gas turbine combustion systems for aero-engines and stationary power plants. Up to now, the development of such systems has primarily been based on long-lasting experimental test campaigns, which typically require a large number of physical prototypes. These campaigns often entail significant expenses and may not always provide the desired measurement data. High operating temperatures and pressures inside the test rig, limited optical access, improper acoustic boundary conditions and non-negligible experimental uncertainties are only a few potential factors that can affect the complexity and accuracy of the performed measurements.

Computational methods for the simulation and analysis of fluid flows - commonly referred to as computational fluid dynamics (CFD) - present a promising alternative to complement the research and development of modern combustion systems. CFD tools can readily enable the optimisation of certain parameters, e.g. the fuel-oxidiser mixing quality, improved wall cooling and other design features, in addition to providing insight into a system's characteristic flow properties including the quantification of exhaust gas emissions. As such, these tools are of growing importance when it comes to reducing the development lead time and costs of industrial applications. Nevertheless, as there are still a number of remaining uncertainties in terms of the modelling and numerical accuracy of CFD, further prototype testing will still be required to qualify a newly-developed combustion systems for installation in a gas turbine.

Industrial and academic research institutions are collaborating on improving existing and developing novel, more advanced CFD tools. The fundamental basis of these activities is the direct numerical simulation (DNS) of fluid flows using the conservation laws of mass, momentum, and energy, which are known to govern fluid motion. For this purpose, all existing length and time scales of a given flow field - including its smallest turbulent structures - need to be directly resolved. Unfortunately, even the world's fastest and most powerful high performance computers, to this day, cannot fully cope with these immense computational requirements, limiting the use of DNS to mostly academic or low Reynolds number flow problems. In order to obtain valuable information on the higher Reynolds number fluid flows typically encountered in practical applications, so-called Reynolds-averaged Navier-Stokes (RANS) methods have been introduced. RANS is based on the decomposition of all flow quantities into time-averaged mean values and their respective statistical deviations. These decomposed quantities are then inserted back into the system of governing equations, giving rise to additional unknown terms that require modelling. Although RANS holds a clear advantage over DNS in terms of the associated computational costs, its predictive capabilities are unquestionably inferior due to the added averaging and modelling procedures involved.

Large eddy simulation (LES), on the other hand, offers a compromise between the computational costs of RANS and the predictive qualities of DNS. It has shown a promising development curve over the past few decades and is now applied to industrial-scale problems involving complex geometries under realistic conditions, see e.g. the review by Gicquel et al. (2012). In LES, governing transport equations describing the flow field are spatially filtered to separate the energy containing large-scale flow structures from the much smaller dissipative turbulent motions. The resulting sub-grid scale (*sgs*) contributions are closed through additional turbulence and combustion models. In most cases, these *sgs* contributions are expected to be small compared to RANS when a sufficiently fine domain discretisation is achieved. Moreover, for inert flows away from solid boundaries, results are known to be relatively insensitive to the models used to represent the *sgs* stresses. Unlike conventional RANS, which still remains the industry-wide standard CFD method, LES can provide time-resolved, three-dimensional data and thus allow for a deeper insight into the unsteady flow-flame dynamics of full-scale combustion devices, even extending to the quantification of thermo-acoustic behaviour.

1.2 Combustion instabilities

Since first encountered in liquid propellant rocket engines more than 50 years ago, Crocco (1969); Crocco and Cheng (1956), combustion-driven instabilities have been a major focal point of combustion research with steadily growing interest in the recent past. Evermore stringent emissions regulations in the civil aviation and stationary power generation industries have led to the development of new combustor concepts operating under lean, partially premixed conditions. As a result, a significant reduction of pollutant emissions such as nitrogen oxides (NO_x) and carbon monoxide (CO) has been achieved. One major drawback of these low-emission combustors, however, is their susceptibility to self-excited combustion instabilities, Lefebvre (1999); Lieuwen and Yang (2005), which are typically only detected during late-stage prototype testing. This will then either trigger a costly, iterative redesign process, or lead to the *a posteriori* installation of preventive measures through retrofit solutions, often at the expense of the combustor's thermal efficiency. Modern swirl-stabilised combustor configurations, in particular, suffer from the potential onset of both thermo-acoustic and hydrodynamic instabilities as described in the following.

1.2.1 Underlying physical phenomena

Initial works by Fleifil et al. (1996) and Dowling (1999) have investigated combustion-driven instabilities for fundamental test cases involving laminar premixed flames. It was shown that acoustic waves generated from unsteady combustion may be reflected inside of a given geometry (e.g. due to a large pressure reflection coefficient), propagate back upstream and subsequently exert kinematic effects on the flame's 'surface area', thereby modulating its rate of heat release. Within the much more complex environment of gas turbine combustors, these types of instabilities are usually characterised by high-amplitude oscillations of the pressure and heat release rate and arise when a resonant feedback loop between the combustion chamber acoustics and the unsteady reactive flow field is established. The time and volume integral of the pressure × heat release rate must therefore be greater than zero in order to satisfy the well-known Rayleigh (1877, 1878) criterion. If this is satisfied, an increase of the oscillation amplitude will occur until the acoustic energy added to the system equals its energy losses. The ensuing state of zero growth rate, commonly referred to as limit-cycle oscillation, is controlled and driven by a variety of complex, highly non-linear physical mechanisms. Operating in such limit-cycle conditions may lead to major problems ranging from higher sound and pollutant emissions to increased heat fluxes at the walls, local flame extinction and flashback, or in severe cases even component failures.

One of the main drivers known to trigger and sustain thermo-acoustic instabilities in partially premixed combustion systems are equivalence ratio oscillations. This particular feedback mechanism was first described by Lieuwen and Zinn (1998) and stems from a fluctuating supply of fresh reactants into the main flame zone, generating unsteady heat release by modulating the reaction rate per unit flame 'area'. The resulting pressure disturbance at the flame front propagates up- and downstream in the form of an acoustic wave, where it can perturb the fuel and oxidiser supply rates. Different acoustic impedances of the respective inflow streams may then periodically vary the mixture's local equivalence ratio closing the feedback loop. A convective time delay between the point of fuel injection and the flame front can be introduced governing the phase lag between the pressure and heat release rate fluctuations, Straub and Richards (1999). The exact role of equivalence ratio oscillations in sustaining thermo-acoustic instabilities has since been studied extensively, e.g. by Ćosić et al. (2015); Hermeth et al. (2013); Kim et al. (2010b); Stöhr et al. (2017).

A second major category of physical phenomena contributing to the generation of unsteady heat release in swirling flames are hydrodynamic instabilities, which have recently been reviewed by Candel et al. (2014). These can be linked to two different types of periodic mechanisms: (*i*) perturbations of the turbulent burning velocity due to flame angle oscillations induced by temporal fluctuations of the swirl number, Kim et al. (2010a); Palies et al. (2010); Schuller et al. (2003); Straub and Richards (1999) and (*ii*) modulation of the flame's 'surface area' via the interaction of large-scale coherent structures, i.e. toroidal vortex shedding, Poinsot et al. (1987); Sterling and Zukoski (1987); Venkataraman et al. (1999); Yu et al. (1991) or precessing vortex cores (PVC), Moeck et al. (2012); Paschereit et al. (2000); Syred (2006); Wang et al. (2007) with the turbulent flame front. The latter can also play an important role in flame lift-off, Hermeth et al. (2014) and flashback, Schönborn et al. (2014) events, and influence the mixing process between fuel and oxidiser, Froud et al. (1995).

The above feedback mechanisms (excluding the PVC) are often associated with longitudinal instability modes. However, other types of modes known to act in the transverse direction have been identified in the past. These transverse modes typically involve higher frequencies on the order of $\sim \mathcal{O}(10^3)$, O'Connor et al. (2015), and non-axisymmetric flow patterns, as opposed to the rather low-frequency, axisymmetric behaviour of their longitudinal counterparts. They can be further classified into three different sub-categories depending on their specific mode shape: (*i*) radial (or tangential) standing modes, with pressure nodes that are fixed in space, (*ii*) azimuthally spinning (or turning) modes, where the entire pressure structure is spinning at the sound speed, and, (*iii*) rotating modes, which are essentially standing modes that rotate about the central burner axis at the azimuthal convective speed, Wolf et al. (2012). A combined longitudinal-transverse mode - termed slanted mode - was also described by Bourgouin et al. (2015).

Transverse combustion instabilities have predominantly been studied for annular-type combustion chamber configurations in various experimental e.g., Bourgouin et al. (2013); Mazur et al. (2019); Prieur et al. (2017); Worth and Dawson (2013), numerical e.g., Bauerheim et al. (2015); Fureby (2010); Laera et al. (2017); Staffelbach et al. (2009); Wolf et al. (2012) and theoretical e.g., Ghirardo and Juniper (2013); Magri et al. (2016); Méry (2017); Moeck et al. (2019); Noiray and Schuermans (2013); Pankiewitz and Sattelmayer (2002); Stow and Dowling (2009) works. In such annular configurations, acoustic waves travelling in the transverse direction have been found to periodically modulate the local flame response of each individual combustor around the chamber's circumference. The resulting spatial non-uniformity in heat release drives the underlying pressure oscillation. Wolf et al. (2012) and Smith et al. (2018) have recently shown that in addition to directly interacting with the flame, these pressure disturbances can also induce fluctuations of the longitudinal velocity (i.e. mass flow rate) in each single combustor unit, and thereby provoke an unsteady heat release response. Transverse acoustic forcing has previously been applied to single or multiple flame set-ups in order to reduce the problem size by representing only a sector of the full annular geometry, see e.g. Hauser et al. (2011); Malanoski et al. (2013); Saurabh and Paschereit (2017). In contrast, transverse modes in can-annular or single can-type combustion chambers have received much less attention in the past. Notable studies of can-annular configurations include the works of Farisco et al. (2017); Ghirardo et al. (2019); Kaufmann et al. (2008); Moon et al. (2019). Swirl-stabilised, single can combustors have been investigated by e.g., Berger et al. (2017); Selle et al. (2006); Zellhuber et al. (2014). Finally, a general review of transverse combustion instabilities in air-breathing systems can be found in O'Connor et al. (2015).

1.2.2 Numerical modelling strategies

Advanced computational methods - essentially LES - are potentially capable of facilitating the prevention of both thermo-acoustic and hydrodynamic instabilities in the initial design stages of modern combustion systems. While early pioneering works have mainly focused on the simulation of rocket motors, e.g. Baum and Levine (1982) and ramjets, e.g. Kailasanath et al. (1991); Menon and Jou (1991), more recent works have also targeted swirl-stabilised gas turbine combustors in particular, Huang and Yang (2009). Detailed reviews of numerical prediction and control methods for combustion instabilities can be found in Dowling and Morgans (2005) and Poinsot (2017). Generally, two different modelling strategies exist.

In the first approach, so-called open-loop - or coupled - LES methods, 'conventional' incompressible LES is combined with low-order modelling techniques from acoustic theory, see e.g. Angelberger et al. (2000); Giauque et al. (2005); Han et al. (2015); Noiray et al. (2008); Paschereit et al. (2002); Polifke et al. (2001). The frequency and amplitude of potential limit-cycle oscillations in any combustor geometry can thereby be systematically determined. For this purpose, a system's heat release response to incoming velocity fluctuations is obtained in LES by externally forcing the inflow velocity at different frequencies and amplitudes. The resulting flame transfer function (FTF) for linear analysis, Bloxsidge et al. (1988) or flame describing function (FDF) for weakly non-linear analysis, Dowling (1997) is then evaluated with a low-order acoustic network model or alternatively a Helmholtz solver providing the corresponding growth rates and frequencies for each forcing amplitude. Whilst this approach is considered useful for predicting the overall acoustic behaviour of a specific combustor geometry, and thus attractive for industrial use, it provides only limited insight into the physically complex, non-linear feedback mechanisms associated with the instabilities. One example of the method's limitations is its inability to predict transverse acoustic modes, since these are created inside the combustion chamber itself, Poinsot and Veynante (2005).

A fully compressible LES formulation, see e.g. Erlebacher et al. (1992), is therefore required when dealing with self-excited thermo-acoustic phenomena in order to allow for the propagation of acoustic waves represented by temporal fluctuations in the pressure field. In this second approach, inherent coupling mechanisms between the flame, flow and acoustics inside a combustion chamber can be directly accounted for. Such unforced LES computations often prove challenging, however, as they require careful consideration of all geometrical parts making up the domain as well as accurate boundary conditions including acoustic impedances at all inlets and outlets. Hence, there are only a very limited number of computational studies in the open literature utilising compressible LES to study self-excited combustion instabilities in gas turbine combustors: Chen et al. (2019a,b); Franzelli et al. (2012); Lourier et al. (2017); Martin et al. (2004); Noh et al. (2019); Roux et al. (2005); Schmitt et al. (2007); Schulz et al. (2019); Staffelbach et al. (2009); Tachibana et al. (2015).

1.3 Objectives and thesis structure

The overall aim of the present work is to devise a reliable and accurate LES method for predicting the onset and subsequent development of self-excited combustion instabilities in gas turbine combustion chambers. The prospective method will be derived from the existing, in-house code BOFFIN-LESi (**BO**undary-**F**itted **F**low **IN**tegrator), which is based on an incompressible formulation and applies a transported probability density function (*pdf*) approach for turbulence-chemistry interaction. Three specific objectives have been set out:

(i) To develop a fully compressible LES method for turbulent, reacting flows in complex geometries - this includes the implementation of effective boundary conditions and subsequent computation of simple acoustic flow problems for validation purposes.

(ii) To successfully capture self-excited limit-cycle oscillations in gas turbine combustion chambers without applying any artificial external forcing - the method's predictive capabilities are to be assessed by comparison with available measurement data.

(iii) To verify existing knowledge on combustion-driven instabilities, while attempting to further study the underlying physics of longitudinal and transverse, thermo-acoustic and hydrodynamic instability modes and their governing feedback mechanisms.

This thesis is divided into six chapters with the following structure. Directly succeeding the present introduction (Chapter 1), an overview is given on the theory and mathematical modelling associated with large eddy simulations of compressible, turbulent, reacting flows. The focus here lies on the specific formulation of the derived LES-*pdf* method called BOFFIN. The use of non-reflective outflow boundary conditions is then described and verified based on two non-reacting, inviscid flow problems with simple geometries. Chapter 3 aims at assessing the predictive capabilities and determining the feasibility of the applied combustion model based on the well-known PRECCINSTA combustor. An incompressible solver formulation is invoked to provide a benchmark for the ensuing compressible simulation presented in Chapter 4. The latter focuses on the combined effects of thermo-acoustic and hydrodynamic instabilities studied in the same test case. Subsequently, an analysis of the superposition between a longitudinal and azimuthal instability mode in the industrial SGT-100 combustor is carried out in Chapter 5. The final conclusions drawn from this work are summarised in Chapter 6 including a brief outlook on possible directions for future work.

Chapter 2

Large eddy simulation of compressible turbulent reacting flows

The highly turbulent behaviour of swirl-stabilised flames involving fast chemical reactions and sophisticated geometrical features strongly limits our current understanding of the complex flow physics encountered in modern low-emission gas turbine combustors. A potentially powerful numerical simulation tool capable of providing better insight into the physical processes associated with these turbulent reacting flows is large eddy simulation. The concept behind LES methods is the direct computation of large-scale, energetic turbulent motions, whereas the effects of motions whose 'size' is smaller than a defined filter width are modelled. A major outstanding challenge in the development of such methods for turbulent combustion is the interaction between turbulence and chemistry on the small, unresolved *sgs* (or subfilter) scales. These turbulence-chemistry interactions arise because of the highly non-linear chemical reaction rates that appear in the form of filtered source terms in the LES scalar equations, for which detailed modelling is required. Various combustion models addressing this closure problem have been proposed in the past, though most of them have been formulated for one specific burning regime only. An overview of the different modelling techniques can be found, amongst others, in a review by Pitsch (2006). The combined LES-*pdf* approach devised in the current work is presented below.

2.1 Fundamental governing equations

In the field of continuum mechanics, the evolution of any given fluid flow can be described by a set of coupled non-linear partial differential equations (*pdes*) based on the laws of mass, momentum and energy conservation. Additionally, in the case of reacting flows, these *pdes* are typically complemented by the following thermochemical relations.

2.1.1 Thermochemical relations

When dealing with multi-component mixtures, it is often useful to define the dimensionless mass fraction Y_φ for each of the N_{sp} chemical species involved:

$$Y_\varphi = \frac{m_\varphi}{\sum_{\varphi=1}^{N_{sp}} m_\varphi} = n_\varphi W_\varphi \tag{2.1}$$

where m_φ represents the mass of species φ. Division of the species mass fraction by the respective molar mass W_φ provides the specific mole number n_φ, which can be used to introduce another important quantity known as the mole fraction X_φ:

$$X_\varphi = \frac{n_\varphi}{n} = \frac{n_\varphi}{\sum_{\varphi=1}^{N_{sp}} n_\varphi} \tag{2.2}$$

where n is the total number of moles in the mixture. Within the framework of subsonic flows (Mach < 1), it is common practice to consider each component as an ideal gas. The thermodynamic state of a system can then be described by the ideal gas law:

$$p = \rho R T \tag{2.3}$$

Here, the pressure p is directly coupled to the density ρ and temperature T. The specific gas constant R is defined as the ratio between the universal gas constant R^0 and mean molar mass of the mixture W, which is obtained from the specific mole numbers of all species:

$$W = \frac{1}{\sum_{\varphi=1}^{N_{sp}} n_\varphi} \tag{2.4}$$

The energetic state of a system can be expressed by the (static) enthalpy h_s, defined as the sum of the sensible enthalpy and the chemical enthalpy of formation:

$$h_s = \int_{T_0}^{T} C_p dT + \sum_{\varphi=1}^{N_{sp}} \Delta h_\varphi^0 Y_\varphi \tag{2.5}$$

where C_p is the mixture's mean heat capacity at constant pressure and Δh^0_φ is the formation enthalpy of each species at the reference temperature T_0. The non-linear integral term in Eq. (2.5) can be approximated, e.g. by utilising the JANAF (**J**oint-**A**rmy-**N**avy-**A**ir-**F**orce) polynomials[1].

2.1.2 Physical conservation laws

The universal conservation laws of mass, momentum and energy can now be cast into a set of *pdes* - note that unless otherwise stated, the Einstein summation convention is applied to repeated indices throughout this work[2]. These *pdes* consist of the continuity (2.6), Navier-Stokes (2.7), energy (2.8) and species mass conservation (2.9) equations, see e.g. Williams (2018), which for compressible flows can be written as:

$$\frac{\partial \rho}{\partial t} + \frac{\partial \rho u_i}{\partial x_i} = 0 \tag{2.6}$$

$$\frac{\partial \rho u_i}{\partial t} + \frac{\partial \rho u_i u_j}{\partial x_j} = -\frac{\partial p}{\partial x_i} + \frac{\partial \tau_{ij}}{\partial x_j} + \rho g_i\,, \;\; i = [i, j, k] \tag{2.7}$$

$$\frac{\partial \rho h_s}{\partial t} + \frac{\partial \rho u_i h_s}{\partial x_i} = \frac{\partial p}{\partial t} + u_i \frac{\partial p}{\partial x_i} - \frac{\partial J_{h,i}}{\partial x_i} + \Theta + \rho \dot{\omega}_h \tag{2.8}$$

$$\frac{\partial \rho n_\varphi}{\partial t} + \frac{\partial \rho u_i n_\varphi}{\partial x_i} = -\frac{\partial J_{\varphi,i}}{\partial x_i} + \rho \dot{\omega}_\varphi\,, \;\; \varphi = [1, ..., N_{sp}] \tag{2.9}$$

where t is the time, u_i and x_i denote, respectively, the velocity and spatial coordinate in i-direction, and g_j represents the body forces per unit volume, which will be neglected going forward. The terms representing viscous stress τ_{ij} and viscous heating Θ are defined by:

$$\tau_{ij} = -\frac{2}{3}\mu \frac{\partial u_k}{\partial x_k}\delta_{ij} + \mu \left(\frac{\partial u_i}{\partial x_j} + \frac{\partial u_j}{\partial x_i} \right) \tag{2.10}$$

$$\Theta = -\frac{2}{3}\mu \left(\frac{\partial u_k}{\partial x_k} \right)^2 + \mu \left(\frac{\partial u_i}{\partial x_j} + \frac{\partial u_j}{\partial x_i} \right) \frac{\partial u_i}{\partial x_j} \tag{2.11}$$

respectively. Here, μ is the dynamic viscosity and δ_{ij} denotes the Kronecker delta. Note that viscous heating is neglected in the current formulation. Fick's first law of diffusion, see e.g. Kuo (1986) or Libby and Williams (1994), is typically invoked for the species diffusion flux

---

[1] https://janaf.nist.gov/

[2] no summation is implied by repeated Greek subscripts

$J_{\varphi,i}$ in the species mass conservation equations (2.9) resulting in:

$$J_{\varphi,i} = -\rho D_\varphi \frac{\partial n_\varphi}{\partial x_i} = -\frac{\mu}{\sigma}\frac{\partial n_\varphi}{\partial x_i} \tag{2.12}$$

where an equal diffusivity assumption has been adopted for all species $D_\varphi = D$. This global diffusivity D can then be related to the Schmidt number via $\sigma = \mu/\rho D$, representing the ratio of momentum and molecular diffusion. Soret and Dufour effects have furthermore been neglected in this work. The corresponding heat diffusion flux $J_{h,i}$ in the energy equation (2.8) consists of a heat diffusion term obtained from Fourier's law plus a term including the sum of all species diffusion fluxes with their respective enthalpies:

$$J_{h,i} = -\lambda\frac{\partial T}{\partial x_i} + \sum_{\varphi=1}^{N_{sp}} h_\varphi J_{\varphi,i} = -\frac{\mu}{Pr}\frac{\partial h_s}{\partial x_i} - \mu\left(\frac{1}{\sigma} - \frac{1}{Pr}\right)\sum_{\varphi=1}^{N_{sp}} h_\varphi \frac{\partial n_\varphi}{\partial x_i} = -\frac{\mu}{\sigma}\frac{\partial h_s}{\partial x_i} \tag{2.13}$$

where λ is the thermal conductivity. The first term can be rewritten for the enthalpy and by making use of the Prandtl number $Pr = \mu C_p/\lambda$, which compares momentum and heat transport. The second term is often neglected under the Lewis number unity assumption $Le = \sigma/Pr \approx 1$, see e.g. Poinsot and Veynante (2005).

Finally, the enthalpy source term $\dot{\omega}_h$ in Eq. (2.8) and the chemical source terms $\dot{\omega}_\varphi$ in Eq. (2.9) represent, respectively, heat sources such as radiation or spark induced energy, and the net formation and consumption rate per unit volume of each species through chemical reaction.

2.2 Large eddy simulation

An exact solution to the above set of *pdes* (cf. Eqs. (2.6), (2.7), (2.8) and (2.9)) can only be obtained by means of DNS. For this purpose, even the smallest turbulent structures need to be resolved. Today's computing power cannot cope with these requirements, generally limiting the application of DNS to low Reynolds number flows. LES was consequently introduced to obtain three-dimensional, time-resolved solutions to practical high Reynolds number flow problems. In LES, the separation of large- and small-scale motions is achieved through a spatial filtering operation. Thereby, energy containing large-scale structures can be resolved whereas the influence of the dissipative small-scale structures is captured via sub-grid models, significantly reducing the required computing power.

2.2.1 Filtering operation

The spatial filter of a function $f = f(\mathbf{x},t)$ is defined as its convolution with a filter function G, according to:

$$\overline{f}(\mathbf{x},t) = \int_{\Omega} G(\mathbf{x}-\mathbf{x}';\Delta(\mathbf{x}))f(\mathbf{x}',t)\mathrm{d}\mathbf{x}' \tag{2.14}$$

where the filter function must be positive definite in order to maintain filtered values of scalars such as mass fraction within bound values and to preserve the nature of the source terms associated with chemical reaction (a filter that changes sign may change consumption terms to formation terms). The integration is defined over the entire flow domain Ω and the condition that the filter kernel G should be positive definite implies that it has the properties of a *pdf*. The filter function has a characteristic width Δ which, in general, may vary with the spatial position $\mathbf{x}$. In the present work, a box or 'top hat' filter defined by:

$$\begin{aligned} G(\mathbf{x}-\mathbf{x}') &= \frac{1}{\Delta^3} \text{ for } |\mathbf{x}-\mathbf{x}'| < \frac{\Delta}{2} \\ &= 0 \text{ otherwise} \end{aligned} \tag{2.15}$$

is used. The density variations in the unresolved scales that arise in combusting flows can be treated through the use of density-weighted, or Favre, filtering, defined by $\widetilde{f} = \overline{\rho f}/\overline{\rho}$.

2.2.2 Filtered equations of fluid motion

Application of this density-weighted filtering operation to the conservation equations of mass (2.6) and momentum (2.7) yields:

$$\frac{\partial \overline{\rho}}{\partial t} + \frac{\partial \overline{\rho}\widetilde{u}_i}{\partial x_i} = 0 \tag{2.16}$$

$$\frac{\partial \overline{\rho}\widetilde{u}_i}{\partial t} + \frac{\partial \overline{\rho}\widetilde{u}_i\widetilde{u}_j}{\partial x_j} = -\frac{\partial \overline{p}}{\partial x_i} + \frac{\partial}{\partial x_j}\left[-\frac{2}{3}\mu\frac{\partial \overline{u_k}}{\partial x_k}\delta_{ij} + \mu\left(\frac{\partial \overline{u}_i}{\partial x_j} + \frac{\partial \overline{u}_j}{\partial x_i}\right)\right] - \frac{\partial \tau_{ij}^{sgs}}{\partial x_j} \tag{2.17}$$

The unclosed *sgs* stress tensor $\tau_{ij}^{sgs} = \overline{\rho}\left(\widetilde{u_i u_j} - \widetilde{u}_i\widetilde{u}_j\right)$ remains unknown and requires modelling. Its deviatoric part is determined with the Smagorinsky (1963) model:

$$\tau_{ij}^{sgs} - \frac{\delta_{ij}}{3}\tau_{kk}^{sgs} = -2\mu_{sgs}\left(\widetilde{e}_{ij} - \frac{\delta_{ij}}{3}\widetilde{e}_{kk}\right)$$

which introduces a *sgs* viscosity μ_{sgs} to mimic the diffusion process on the dissipative small-scales according to:

$$\mu_{sgs} = \overline{\rho}(C_s\Delta)^2||\widetilde{e}_{ij}|| \tag{2.18}$$

where $||\widetilde{e}_{ij}|| = \sqrt{2\widetilde{e}_{ij}\widetilde{e}_{ij}}$ is the Frobenius norm of the resolved rate of strain tensor e_{ij} defined by:

$$\widetilde{e}_{ij} = \frac{1}{2}\left(\frac{\partial\widetilde{u}_i}{\partial x_j} + \frac{\partial\widetilde{u}_j}{\partial x_i}\right) \tag{2.19}$$

The Smagorinsky parameter C_s is obtained through the dynamic procedure of Piomelli and Liu (1995) while the filter width Δ is taken as the cube root of the local grid cell volume, which may vary with position. The isotropic parts of the viscous and *sgs* stresses are absorbed into the pressure.

2.2.3 Filtered scalar transport equations

The filtered transport equations for the enthalpy and specific mole number of each species read:

$$\frac{\partial\overline{\rho}\widetilde{h}_s}{\partial t} + \frac{\partial\overline{\rho}\widetilde{u}_i\widetilde{h}_s}{\partial x_i} = \frac{D\overline{p}}{Dt} + \frac{\partial}{\partial x_i}\left(\frac{\mu}{\sigma}\frac{\partial\overline{h}_s}{\partial x_i}\right) - \frac{\partial J^{sgs}_{h,i}}{\partial x_i} + \overline{\rho\dot{\omega}_h} \tag{2.20}$$

$$\frac{\partial\overline{\rho}\widetilde{n}_\varphi}{\partial t} + \frac{\partial\overline{\rho}\widetilde{u}_i\widetilde{n}_\varphi}{\partial x_i} = \frac{\partial}{\partial x_i}\left(\frac{\mu}{\sigma}\frac{\partial\overline{n}_\varphi}{\partial x_i}\right) - \frac{\partial J^{sgs}_{\varphi,i}}{\partial x_i} + \overline{\rho\dot{\omega}_\varphi} \tag{2.21}$$

where $D\overline{p}/Dt = \partial\overline{p}/\partial t + \widetilde{u}_i\partial\overline{p}/\partial x_i$ represents the filtered material derivative of the pressure. For the *sgs* fluxes $J^{sgs}_{h,i}$ and $J^{sgs}_{\varphi,i}$, a gradient diffusion approximation (Schmidt and Schumann, 1989) analogous to the Smagorinsky model can be invoked, written in terms of a combined general scalar:

$$J^{sgs}_{\alpha,i} = \overline{\rho}(\widetilde{u_i\phi_\alpha} - \widetilde{u}_i\widetilde{\phi}_\alpha) = -\frac{\mu_{sgs}}{\sigma_{sgs}}\frac{\partial\widetilde{\phi}_\alpha}{\partial x_i} \tag{2.22}$$

Here, $\phi_\alpha = [\phi_1, ..., \phi_{N_s}]$ is the general scalar adopting n_φ or h_s as appropriate, where N_s is the number of scalars α (species plus enthalpy) required to describe the system. σ_{sgs} is the *sgs* Prandtl/Schmidt number, often referred to as the turbulent Schmidt number. By utilising this general scalar expression, both transport equations can be combined into the following filtered scalar transport equations:

$$\frac{\partial\overline{\rho}\widetilde{\phi}_\alpha}{\partial t} + \frac{\partial\overline{\rho}\widetilde{u}_i\widetilde{\phi}_\alpha}{\partial x_i} = \frac{\partial}{\partial x_i}\left[\left(\frac{\mu}{\sigma} + \frac{\mu_{sgs}}{\sigma_{sgs}}\right)\frac{\partial\widetilde{\phi}_\alpha}{\partial x_i}\right] + \overline{\rho\dot{\omega}_\alpha} \tag{2.23}$$

For the enthalpy, the unclosed scalar source term $\overline{\dot{\omega}}_\alpha$ includes potential heat sources and the material derivative of the pressure, whereas for all chemical species, it represents the unclosed chemical source terms according to:

$$\overline{\dot{\omega}}_\alpha = \begin{cases} \overline{\dot{\omega}}_h + D\overline{p}/Dt, & \text{for the enthalpy} \\ \overline{\dot{\omega}}_\varphi, & \text{for all chemical species} \end{cases} \tag{2.24}$$

The latter case introduces significant complexity to the simulation of turbulent reacting flows as a result of the strong interactions between turbulence and chemistry on the small-scales.

2.3 Combustion modelling

In order to address the afore-mentioned closure problem in the filtered species mass fraction transport equations, a sub-grid combustion model needs to be implemented. The combustion model underlying this work is based on a transported *pdf* approach solved by the Eulerian stochastic fields method. It has the advantage of a potentially burning regime independent description of turbulent flames, which becomes particularly useful in the context of gas turbine combustion. State of the art gas turbine combustors are designed to operate under lean, partially premixed conditions in order to effectively reduce pollutant emissions such as NO_x and CO. In the partially premixed burning regime, parts of the flow field are governed by premixed flame propagation and finite-rate effects, i.e. auto-ignition, extinction or ignition, while other parts will display mixing controlled reactions as encountered in diffusion (or non-premixed) flames. It has been shown in the past, see e.g. Jones and Navarro-Martinez (2007); Jones and Prasad (2010, 2011), that it is possible to capture these phenomena within a single LES framework using the present *pdf* method to account for turbulence-chemistry interaction. In a detailed study of an industrial gas turbine combustor, Bulat et al. (2013, 2014) employed this LES formulation and achieved good reproduction of the experimentally measured flow statistics. Local extinction of the flame was shown to be due to turbulence-chemistry effects rather than large-scale mixing and the combustor was found to have regions in the diffusion flame burning regime.

2.3.1 Sub-grid probability density function

Due to the difficulties encountered in evaluating the filtered values of the chemical source terms, the combined scalar transport equations (2.23) are not solved directly in the present work. Instead, the influence of *sgs* fluctuations on the species formation rates are accounted for following the approach of Gao and O'Brien (1993). A joint *sgs-pdf*, denoted $\widetilde{P}_{sgs}$, is therefore introduced representing the filtered product of the fine-grained *pdf* of each scalar - i.e. the specific mole numbers of the chemical species and the enthalpy:

$$\widetilde{P}_{sgs}(\underline{\psi};\mathbf{x},t) = \frac{1}{\overline{\rho}}\int_{\Omega} \rho G(\mathbf{x}-\mathbf{x}',\Delta(\mathbf{x}))\mathcal{F}(\underline{\psi};\mathbf{x}',t)\mathrm{d}\mathbf{x}' \tag{2.25}$$

Here, $\mathcal{F}$ denotes the joint *pdf*, which is simply the product of the fine-grained one-point probability density functions P_α of each scalar:

$$\mathcal{F}(\underline{\psi};\mathbf{x},t) = \prod_{\alpha=1}^{N_s} P_\alpha = \prod_{\alpha=1}^{N_s} \delta\left[\psi_\alpha - \phi_\alpha(\mathbf{x},t)\right] \tag{2.26}$$

where ψ_α is the sample, or composition, space for the scalar ϕ_α with $1 \leq \alpha \leq N_s$ and δ is the Dirac-function.

2.3.2 Transported *pdf* approach

An exact equation describing the evolution of $\widetilde{P}_{sgs}$ can be derived from the appropriate conservation equations using standard methods, e.g. Colucci et al. (1998); Gao and O'Brien (1993); Jaberi et al. (1999). Following the procedure of Brauner et al. (2016) the modelled sub-grid *pdf* evolution equation becomes:

$$\begin{aligned}
\overline{\rho}\frac{\partial \widetilde{P}_{sgs}(\underline{\psi})}{\partial t} + \overline{\rho}\widetilde{u}_i\frac{\partial \widetilde{P}_{sgs}(\underline{\psi})}{\partial x_i} + \sum_{\alpha=1}^{N_s}\sum_{\beta=1}^{N_s}\frac{\mu}{\sigma}\frac{\partial\widetilde{\phi}_\alpha}{\partial x_i}\frac{\partial\widetilde{\phi}_\beta}{\partial x_i}\frac{\partial^2 \widetilde{P}_{sgs}(\underline{\psi})}{\partial\psi_\alpha\partial\psi_\beta} = \\
\underbrace{-\sum_{\alpha=1}^{N_s}\frac{\partial}{\partial\psi_\alpha}\left[\overline{\rho}\dot{\omega}_\alpha(\underline{\psi})\widetilde{P}_{sgs}(\underline{\psi})\right]}_{\textbf{I: }\text{chemical reaction term (closed)}} \\
\underbrace{+\frac{\partial}{\partial x_i}\left[\left(\frac{\mu}{\sigma}+\frac{\mu_{sgs}}{\sigma_{sgs}}\right)\frac{\partial \widetilde{P}_{sgs}(\underline{\psi})}{\partial x_i}\right]}_{\textbf{II: }\textit{sgs-pdf}\text{ transport term (gradient closure)}} \\
\underbrace{-\frac{C_d}{2\tau_{sgs}}\sum_{\alpha=1}^{N_s}\frac{\partial}{\partial\psi_\alpha}\left[\overline{\rho}(\psi_\alpha-\widetilde{\phi}_\alpha(\mathbf{x},t))\widetilde{P}_{sgs}(\underline{\psi})\right]}_{\textbf{III: }\textit{sgs}\text{ micro-mixing term (LMSE closure)}}
\end{aligned} \tag{2.27}$$

where the scalar source term $\dot{\omega}_\alpha$ (I) now appears in closed form and thus does not require any further modelling - this being the main advantage of the *pdf* formulation. It includes either the reaction rate source for the chemical species, or the pressure derivatives and potential heat sources for the enthalpy, according to Eq. (2.24). The two additional unknown terms on the right-hand side of Eq. (2.27) represent *sgs*, or turbulent, transport of the *pdf* (II) and *sgs* micro-mixing due to the action of viscosity (III). These are approximated, respectively, by a gradient closure directly analogous to the Smagorinsky model and by the linear mean square estimation (LMSE) closure, Dopazo (1975, 1979); Dopazo and O'Brien (1974). The *sgs* micro-mixing time scale is given by $\tau_{sgs} = \overline{\rho}\Delta^2/\mu_{sgs}$, while the *sgs* Prandtl/Schmidt number σ_{sgs} and *sgs* micro-mixing constant C_d are assigned the values 0.7 and 2.0, respectively, see e.g. Branley and Jones (2001); Clayton and Jones (2008); Jones et al. (2012); Jones and Navarro-Martinez (2007); Mustata et al. (2006).

2.3.3 Eulerian stochastic fields method

It is not feasible to numerically solve the closed form of the *pdf* evolution equation (2.27) directly, due to the large number of independent variables, but also because $\widetilde{P}_{sgs}(\underline{\psi})$ is a generalised function, defined only in terms of its integral properties. As a consequence, a stochastic solution method is adopted instead, where $\widetilde{P}_{sgs}(\underline{\psi})$ is represented by an ensemble of stochastic fields for each scalar, here denoted $\xi_\alpha^n(\mathbf{x},t)$. The joint *sgs-pdf* equation (2.25) can then be rewritten as follows:

$$\widetilde{P}_{sgs}(\underline{\psi};\mathbf{x},t) = \frac{1}{N}\sum_{n=1}^{N}\frac{1}{\bar{\rho}}\int_\Omega \rho G(\mathbf{x}-\mathbf{x}',\Delta(\mathbf{x})) \times \prod_{\alpha=1}^{N_s}\delta\left[\psi_\alpha - \xi_\alpha^n(\mathbf{x},t)\right]\mathrm{d}\mathbf{x}' \tag{2.28}$$

where $1 \leqslant n \leqslant N$, with N being the number of fields, and $1 \leqslant \alpha \leqslant N_s$. A system of stochastic differential equations (*sdes*) equivalent to Eq. (2.27) can be derived using either an Itô or Stratonovich type formulation, see e.g. Gardiner (1985). The former is adopted in the present work following Valiño (1998) and Sabel'nikov and Soulard (2005):

$$\begin{aligned}\bar{\rho}\mathrm{d}\xi_\alpha^n + \bar{\rho}\widetilde{u}_i\frac{\partial \xi_\alpha^n}{\partial x_i}\mathrm{d}t = \overline{\rho}\dot{\omega}_\alpha^n(\underline{\xi}^n)\mathrm{d}t + \frac{\partial}{\partial x_i}\left[\left(\frac{\mu}{\sigma}+\frac{\mu_{sgs}}{\sigma_{sgs}}\right)\frac{\partial \xi_\alpha^n}{\partial x_i}\right]\mathrm{d}t \\ - \frac{C_d}{2\tau_{sgs}}\bar{\rho}\left(\xi_\alpha^n - \widetilde{\phi}_\alpha\right)\mathrm{d}t + \sqrt{2\bar{\rho}\frac{\mu_{sgs}}{\sigma_{sgs}}}\frac{\partial \xi_\alpha^n}{\partial x_i}\mathrm{d}W_i^n(t)\end{aligned} \tag{2.29}$$

The Wiener process $\mathrm{d}W_i^n(t)$, different for each field but independent of the spatial location $\mathbf{x}$, is approximated by time-step increments $\eta_i^n(\mathrm{d}t)^{1/2}$ containing the $\{-1,1\}$ dichotomic random vector η_i^n. The solutions of the stochastic fields equation (2.29) are continuous, differentiable and smooth on the scale of the filter width in space, and continuous but not differentiable in time. These solutions are not to be mistaken with any particular realisation of the real field, but rather form an equivalent stochastic system in the sense that all the one-point moments resulting from the *sdes* and from the solutions of Eq. (2.27) will be identical. Further details of the solution method and its implementation can be found e.g. in Jones and Prasad (2010). The filtered value of each scalar is finally obtained by averaging over the corresponding stochastic fields.

2.4 Chemistry modelling

The modelling of chemical reactions in combustion CFD is a highly complex topic. Its detailed description would clearly exceed the scope of this work - hence, only the most fundamental principles will be touched upon here. The interested reader is also referred to textbooks by Warnatz et al. (2001) and Turns (1996) for an in-depth explanation of the chemical processes underlying combustion.

2.4.1 Chemical reaction kinetics

In general, any combusting system can be globally defined by the following unique reaction equation:

$$\upsilon_F F + \upsilon_{Ox} Ox \rightarrow \upsilon_P P \tag{2.30}$$

where υ_F, υ_{Ox} and υ_P are, respectively, the coefficients corresponding to fuel (F), oxidiser (Ox) and products (P). While this equation holds true on a global scale, the actual combustion process is composed of a series of elementary reactions.

The unfiltered chemical source term $\dot{\omega}_\varphi$ included in Eq. (2.29) depends on all elementary reactions that species φ is involved in:

$$\dot{\omega}_\varphi = \sum_{r=1}^{N_r} (\nu''_{\varphi,r} - \nu'_{\varphi,r}) r_r \tag{2.31}$$

where $\nu'_{\varphi,r}$ and $\nu''_{\varphi,r}$ are the molar stoichiometric coefficients of species φ in reaction r for a total of N_r elementary reactions. The reaction rate r_r for the r-th elementary reaction can be written as:

$$r_r = k_r^f \prod_{\varphi=1}^{N_{sp}} \left[\rho n_\varphi\right]^{\nu'_{\varphi,r}} - k_r^b \prod_{\varphi=1}^{N_{sp}} \left[\rho n_\varphi\right]^{\nu''_{\varphi,r}} \tag{2.32}$$

The forward k_r^f and backward/reverse k_r^b rate coefficients of reaction r are usually modelled using the empirical Arrhenius law:

$$k_r = A_r T^{\beta_r} \exp\left(-\frac{E_{a,r}}{R^0 T}\right) \tag{2.33}$$

where A_r denotes the pre-exponential constant, β_r is the temperature exponent and $E_{a,r}$ is the activation energy, which can all be obtained from appropriate measurements. However, most detailed kinetic schemes involve a large number of reaction steps and species (e.g. more than 300 reactions and 50 species for methane-air combustion), which leads to very high computational requirements and thus renders them infeasible for LES computations of practical combustion systems. It is therefore often useful to employ more simplified, reduced reaction mechanisms. These can be derived from the complete detailed schemes and are essential in keeping computational costs at a reasonable level.

2.4.2 Reduced reaction mechanisms

In order to correctly reproduce finite-rate chemistry effects such as local flame extinction and re-ignition, an accurate description of the involved chemical reactions is required. For this purpose, two different reduced, yet comprehensive 15-step / 19 species mechanisms for methane oxidation are included in the present LES-*pdf* solver. These have each been derived from the full detailed GRI-Mech 3.0 mechanism[3] as reported in Sung et al. (2001) and Lu and Law (2008), respectively.

Table 2.1 summarises the 15-step augmented reduced mechanism (ARM) proposed by Sung et al. (2001). It uses quasi-steady-state (QSS) assumptions for minor intermediates and contains species such as hydroperoxyl (HO_2) and hydrogen peroxide (H_2O_2), that have been shown to substantially improve the predictive capability over extensive ranges of phenomena and parametric variations. For comparison, Table 2.2 summarises the reduced methane-air mechanism proposed by Lu and Law (2008). Here, the QSS species concentrations are solved analytically as opposed to the traditional algebraic iteration method used in ARM (Sung et al., 2001). A considerable decrease in the required computing time can thereby be achieved, while preventing any convergence issues that may arise in solving the concentrations of the QSS species. Nitric oxide (NO) chemistry is not included in this second mechanism but can optionally be added through an extended version with 17 steps and 21 species, Lu and Law (2008). Both applied mechanisms are expected to deliver similar results. However, due to its analytical solution strategy, the second mechanism of Lu and Law (2008) performed noticeably faster in the current work, with a reduction of computational time by more than half.

---

[3] http://combustion.berkeley.edu/gri-mech/version30/text30.html

Table 2.1: 15-step reduced chemical reaction mechanism for methane oxidation involving 19 species, Sung et al. (2001).

Reaction	Step
$CH_4 + H = CH_3 + H_2$	(R1)
$CH_3 + OH = CH_2O + H_2$	(R2)
$CH_2O = CO + H_2$	(R3)
$C_2H_6 = C_2H_4 + H_2$	(R4)
$C_2H_4 + OH = CH_3 + CO + H_2$	(R5)
$C_2H_2 + O_2 = 2CO + H_2$	(R6)
$CO + OH + H = CO_2 + H_2$	(R7)
$H + OH = H_2O$	(R8)
$2H_2 + O_2 = 2H + 2OH$	(R9)
$2H = H_2$	(R10)
$HO_2 + H = H_2 + O_2$	(R11)
$H_2O_2 + H = H_2 + HO_2$	(R12)
$O_2 + N_2 = 2NO$	(R13)
$HCN + H + O_2 = H_2 + CO + NO$	(R14)
$NH_3 + 3H + H_2O = 4H_2 + NO$	(R15)

Table 2.2: 15-step reduced chemical reaction mechanism for methane oxidation involving 19 species, Lu and Law (2008).

Reaction	Step
$2O = O_2$	(R1)
$H + O = OH$	(R2)
$O + CH_3 = H + CH_2O$	(R3)
$O + CO = CO_2$	(R4)
$H + O_2 = HO_2$	(R5)
$2H = H_2$	(R6)
$H + OH = H_2O$	(R7)
$H + CH_3 = CH_4$	(R8)
$H + CH_2CO = CH_3 + CO$	(R9)
$H_2 + CO = CH_2O$	(R10)
$2OH = H_2O_2$	(R11)
$OH + CH_3 = CH_3OH$	(R12)
$2CH_3 = C_2H_6$	(R13)
$C_2H_4 = H_2 + C_2H_2$	(R14)
$O + C_2H_2 = CH_2CO$	(R15)

2.5 Numerical aspects of BOFFIN

The developed computational method - named BOFFIN throughout this work - was extended from the in-house, incompressible[4] BOFFIN-LESi code, Jones et al. (2002), which has been applied to a wide range of reacting flow problems in the past, see e.g. Brauner (2017); Bulat (2012); Gallot-Lavallée (2018); Jurisch (2016); Noh (2016); Prasad (2011); Xia (2019). BOFFIN is a fully compressible, block-structured, boundary conforming coordinate LES solver comprising a second-order-accurate finite volume method (FVM). The code is fully parallelised by means of domain decomposition and message passing interface (MPI) routines and employs Cartesian velocity components with a co-located variable storage arrangement. It utilises an implicit pressure based formulation with a pressure correction method based on approximate factorisation (see Appendix A) and pressure smoothing, Rhie and Chow (1983).

The spatial and temporal discretisation schemes used in BOFFIN, details of which are given in Jones et al. (2012); Prasad (2011), are summarised in Table 2.3. In the momentum equations, an energy-conserving discretisation scheme is used for the convection terms, whereas all other spatial derivatives are discretised with a second-order central difference scheme (CDS). The stochastic fields equations are discretised using a total variation diminishing (TVD) scheme to avoid unphysical over- and undershoots, along with central differences and an approximately factored Euler-Maruyama (E-M) scheme, see e.g. Kloeden and Platen (1999). The advancement in time is performed with a weak first-order, time-centered Crank-Nicholson (C-N) scheme. A general review on numerical techniques and discretisation schemes for CFD can be found in, e.g. Ferziger and Peric (2012), Wesseling (2009) or Versteeg and Malalasekera (2007).

It should be noted that none of the code's default model parameters are adjusted for the simulations carried out in this work. Eight stochastic fields are used to describe the influence of the *sgs* contributions, as this number has proven to be a good compromise between computational accuracy and costs, see e.g. Jones and Navarro-Martinez (2007). For

Table 2.3: Discretisation schemes used in BOFFIN for the different terms in the momentum and stochastic fields equations.

	Convection	Diffusion	Stochastic	Temporal
Momentum	CDS	CDS	-	C-N
Stochastic fields	TVD	CDS	E-M	C-N

---

[4] see Section 3.2.1 for more details on the incompressible formulation

the boundaries, no-slip conditions are applied at all walls and approximate near wall models based on the semi-logarithm law of the wall, Hoffmann and Benocci (1995); Piomelli and Balaras (2002) are utilised to represent the region between the wall and the nearest wall adjacent grid point. The velocities and density of all incoming streams are fixed to prescribe the mass flow rates at each inflow. Treatment of the outflow boundaries is more complex and will be covered in the next chapter.

2.6 Characteristic boundary conditions

Numerical methods are known to be strongly dependent on the boundary conditions applied for limiting the size of a computational problem. One of the main difficulties encountered in the use of compressible CFD codes, specifically, is the undesired artificial reflection of numerically generated waves at the domain inlets and outlets. These can arise, for example, when fixing the pressure at a subsonic outflow to a constant value (or by extrapolating all quantities from interior points), which may lead to the reflection of pressure disturbances back into the domain. Moreover, acoustic impedances at the boundaries are often unknown *a priori*, making the modelling of physically reflected pressure waves challenging as well. Different approaches towards tackling the issue of acoustic wave reflection have been proposed in the past. A common technique for effective boundary treatment involves the application of so-called characteristic boundary conditions, which have also been chosen in the present work. A brief review of the main contributions towards these characteristic boundaries is provided below, followed by a description of the subsonic non-reflective outflow condition implemented in BOFFIN and the computation of two validation test cases.

One of the first non-reflective boundary conditions for numerical simulations was derived by Engquist and Majda (1977a,b). When applied to the linearised, two-dimensional (inviscid) Euler equations, their ‘second approximation’ can be expressed as:

$$\frac{\partial}{\partial t}\left(p' - \hat{\rho}\hat{c}u'_i\right) + C_1\rho' + C_2 u'_i + C_3 u'_j + C_4 p' + C_5 \frac{\partial u'_j}{\partial x_j} = 0 \tag{2.34}$$

where all quantities are decomposed into a steady-state solution $\hat{\cdot}$ and its respective perturbation $\cdot'$. The coefficients C_{1-5} involve $\hat{\rho}$, $\hat{u}_i$, $\hat{u}_j$ and $\hat{p}$ and their spatial derivatives and the speed of sound is defined as $c = \sqrt{\gamma RT}$ containing the isentropic expansion factor γ. Hedstrom (1979) subsequently developed a non-reflective boundary with non-linear formulation using characteristic wave relations based on Riemann invariants in one space dimension. For this purpose, the flow is essentially decomposed in terms of characteristic waves travelling in the direction normal to the boundary, resulting in the following expression:

$$\frac{\partial p}{\partial t} - \rho c \frac{\partial u}{\partial t} = 0 \tag{2.35}$$

By combining the previous two approaches and using $C_4 = \alpha_p$ and $C_{\neq 4} = 0$, Rudy and Strikwerda (1980, 1981) came up with a non-reflective pressure boundary condition for subsonic outflows:

$$\frac{\partial p}{\partial t} - \rho c \frac{\partial u}{\partial t} + \alpha_p \left(p - \hat{p}\right) = 0 \tag{2.36}$$

where the constant α_p denotes a pressure relaxation coefficient. Thompson (1987) presented a generalised, multi-dimensional formulation for characteristic boundary conditions based on the approach of Hedstrom (1979). In Poinsot and Lele (1992), this formulation was complemented by viscous terms to form the so-called Navier-Stokes characteristic boundary conditions (NSCBC). Yoo and Im (2007); Yoo et al. (2005) later suggested the addition of transverse terms to the NSCBC and introduced a set of non-reflective inflow conditions analogous to the outflow procedure described in Rudy and Strikwerda (1980). The NSCBC approach has since been further extended - e.g. by Lodato et al. (2008) to account for convection and pressure gradients in the boundary planes.

2.6.1 Subsonic non-reflective outflow

The non-reflective outflow condition used in the current work is directly adopted from the early approach of Rudy and Strikwerda (1980, 1981) and supplemented with the transverse term proposed by Yoo and Im (2007); Yoo et al. (2005), resulting in:

$$\left(\frac{\partial p}{\partial t} + \rho c \frac{\partial u_i}{\partial t}\right) + \eta_p \frac{c\left(1 - \mathcal{M}^2\right)}{L_x} \left(p - p_\infty\right) + \beta_t \mathbb{T} = 0 \tag{2.37}$$

where $\mathcal{M}$ is the average Mach number in the outlet plane, L_x is the characteristic size of the computational domain and p_∞ represents the target far-field pressure. The pressure relaxation factor η_p is a constant chosen to manipulate (i.e. minimise) the amplitudes of incoming waves. An optimal value for this factor of 0.28 was derived by Rudy and Strikwerda (1980), which is used throughout the present work. The transverse damping parameter β_t is set equal to $\mathcal{M}$, as suggested by Yoo and Im (2007), and combined with the transverse term $\mathbb{T}$ defined by:

$$\mathbb{T} = u_t \frac{\partial p}{\partial x_t} + \gamma p \frac{\partial u_t}{\partial x_t} - \rho c u_t \frac{\partial u_i}{\partial x_t}, \quad t = [j,k] \tag{2.38}$$

In the current formulation, all three velocity components plus the density are obtained on the boundary by using zero-th order extrapolation from interior points. The pressure is then calculated from the characteristic boundary condition given in Eq. 2.37. With the density and pressure known, the temperature can finally be calculated from the ideal gas law (Eq. 2.3). If needed, the implementation of a full NSCBC formulation into BOFFIN will be considered in future work.

Two non-reacting, inviscid test cases extensively used in the open literature, see e.g. Lodato et al. (2008); Poinsot and Lele (1992); Raynaud et al. (2015); Yoo and Im (2007), are computed in the following, to assess the effectiveness of the implemented non-reflective outflow boundary. A conventional reflective boundary condition with zero-th order extrapolation for all variables is also applied for comparison purposes.

2.6.2 Vortex convection problem

In the first test case, a vortex is superimposed onto a mean bulk flow of pure air and convected through the outflow boundary. The two-dimensional computational domain is a square of dimension L = 0.013 m with an inflow on the left-hand side, an outflow on the right-hand side and symmetry boundaries on the top and bottom sides. The initial axial and transverse velocities, u_i and u_j, are calculated from:

$$u_i = \frac{\partial \Psi}{\partial x_j}, \quad u_j = -\frac{\partial \Psi}{\partial x_i} \tag{2.39}$$

where the stream function Ψ contains the vortex strength and radius, which were set to C_v = 0.005 $\mathrm{m^2/s}$ and R_v = 0.001 m ($\approx$ 7.5% of L), respectively:

$$\Psi = C_v \exp\left(-\frac{r^2}{2R_v^2}\right) + U_\infty x_j \tag{2.40}$$

Here, $r = \sqrt{x_i^2 + x_j^2}$ is the radial distance from the vortex centre. U_∞ = 2 m/s represents the uniform bulk flow velocity prescribed at the inflow and in the initial field. At a reference far-field temperature of T_∞ = 300 K and pressure of p_∞ = 1 atm, this velocity corresponds to a Mach number of $Ma = u_i/c$ = 5.75 $\times$ 10^{-3} and a Reynolds number of about Re = 166. The initial pressure distribution is given by:

$$p = p_\infty \exp\left[-\frac{\gamma}{2}\left(\frac{C_v}{cR_v}\right)^2 \exp\left(-\frac{r^2}{R_v^2}\right)\right] \tag{2.41}$$

Assuming that the initial temperature field is uniform, the initial density distribution can be computed from the equation of state, $\rho(r) = p(r)/(RT_\infty)$. The resulting minimum and maximum velocities induced by the vortex are 5 m/s and -1 m/s in axial direction and 3 m/s and -3 m/s in transverse direction.

Figures 2.1, 2.2 and 2.3 display time series of different instantaneous flow quantities representing the vortex structure convected through both the conventional reflective and newly implemented, non-reflective outflow boundary. Iso-contours of the longitudinal velocity are shown in Fig. 2.1, complemented by the normalised pressure field, which is expressed with respect to the far-field reference pressure and the initial maximum pressure drop:

$$p^* = \frac{p(\mathbf{x},t) - p_\infty}{p_0 - p_\infty} \tag{2.42}$$

where p^* denotes the normalised pressure and $p_0 = p(\mathbf{0}, 0)$ is the initial minimum pressure located in the vortex centre. The reflective outflow applied in the reference case induces upstream wave propagation and strongly modifies the vortex structure once it reaches the boundary - as evidenced by the distorted pressure field and velocity iso-contours. By utilising the non-reflective outflow condition instead, the initial vortex structure remains reasonably well preserved and passes through the boundary without any significant distortions. Minor spurious effects visible near the outflow may be attributed to the applied central difference scheme combined with an insufficient mesh resolution. Overall, the numerical reflection of acoustic waves is considerably reduced compared to the reference case. The transverse velocity and vorticity fields including their respective iso-contours are shown in Figs. 2.2 and 2.3. The temporal evolution of both quantities further supports the above findings despite showing a small distortion of the concentric circles delineating vorticity at around t = 3.4 ms in the non-reflective case.

In order to enable a more quantitative analysis, the local pressure in the centrepoint of the outflow plane was recorded over time; see Fig. 2.4. The pressure profile is expected to maintain its shape while the vortex is passing through the boundary between approximately $t \approx$ 2-4 ms. This is clearly shown for the non-reflective case, albeit with a very minor increase of the pressure magnitude. Conversely, the reflective case exhibits an initial overshoot in the pressure signal and eventually becomes unstable. Pressure oscillations start to develop and the solution is unable to reach a steady-state. The relative minimum pressure within the entire domain is plotted in Fig. 2.5. It should initially be equal to p_0 - the initial minimum pressure in the vortex centre - before relaxing smoothly towards the far-field pressure value once the vortex has crossed the boundary. Indeed, this can be the seen for the non-reflective case, which also shows no evidence of any noticeable over- or undershoots in the signal. Finally,

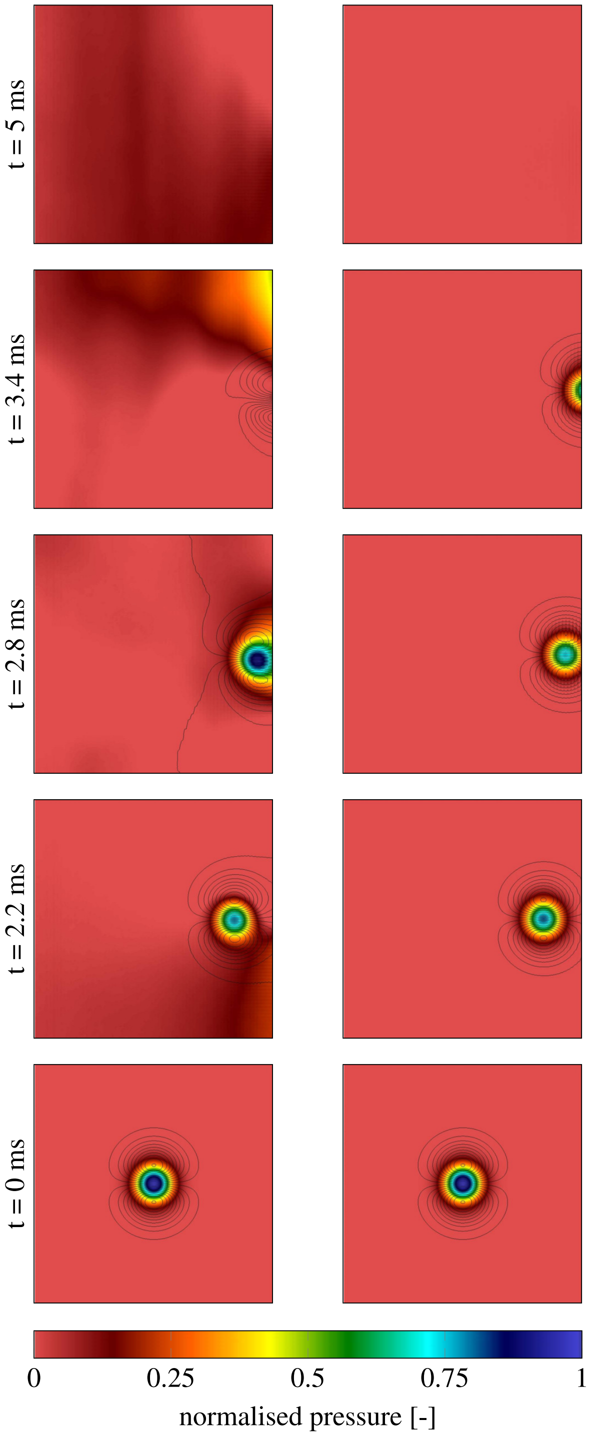

Figure 2.1: Evolution of the normalised pressure field and longitudinal velocity iso-contours at different instants of time using the reflective (left) and non-reflective (right) outflow condition on the right boundary.

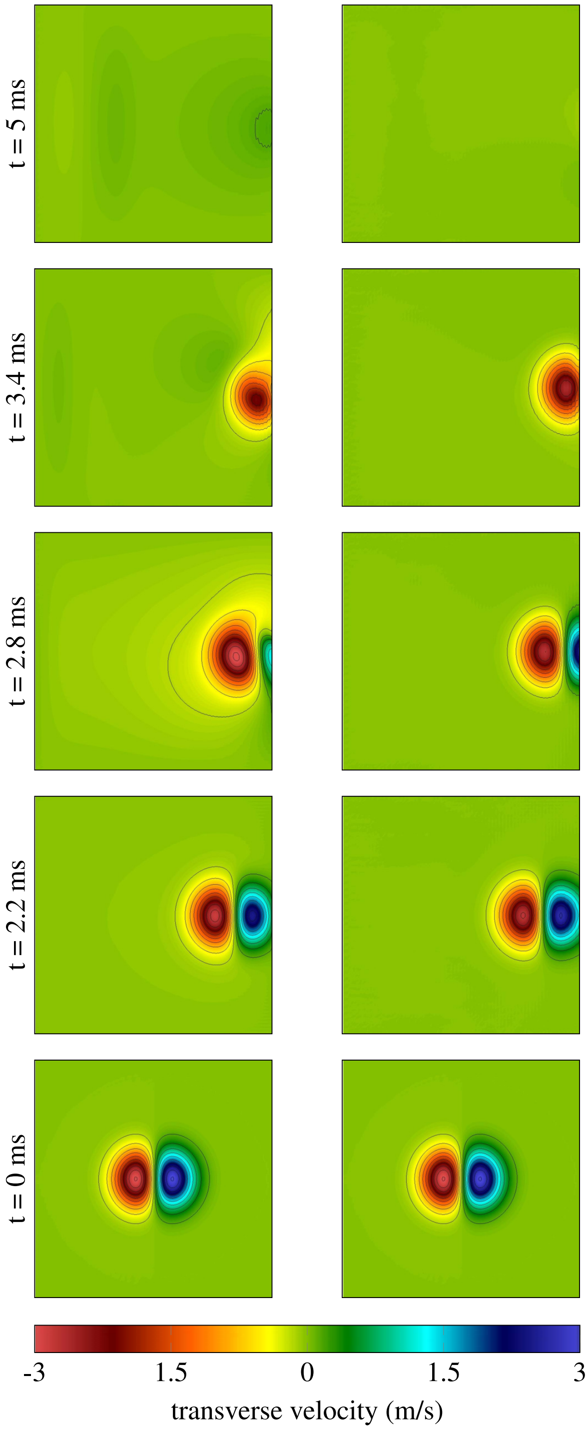

Figure 2.2: Evolution of the transverse velocity field and transverse velocity iso-contours at different instants of time using the reflective (left) and non-reflective (right) outflow condition on the right boundary.

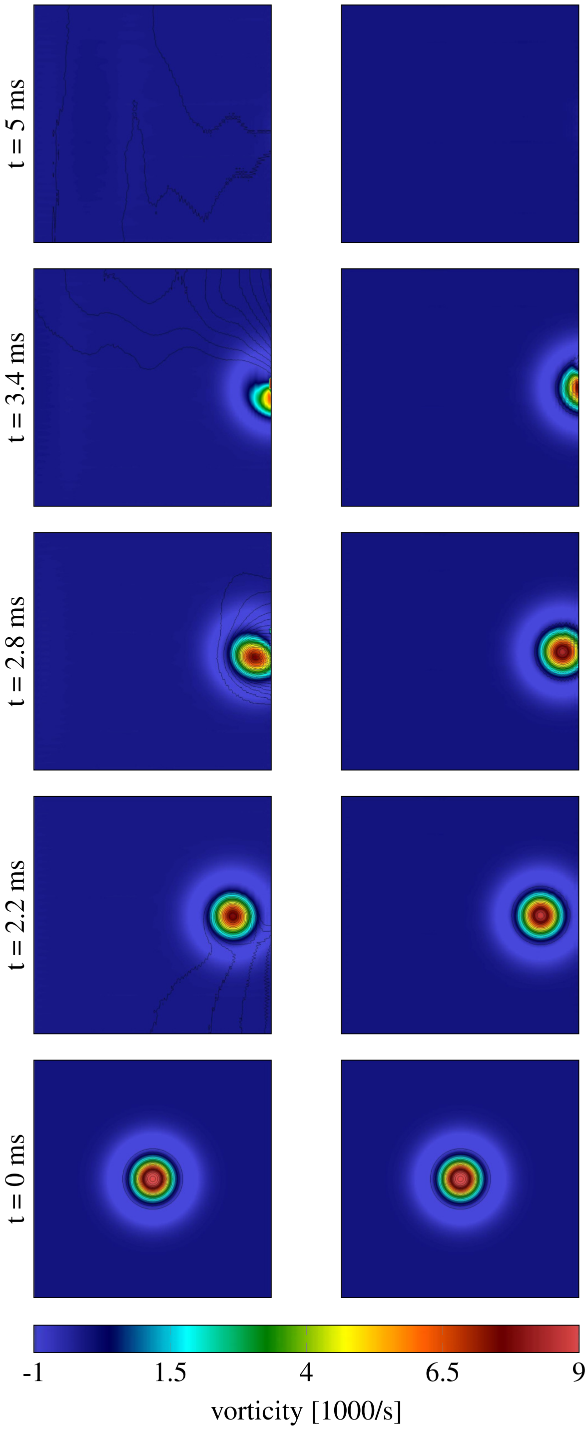

Figure 2.3: Evolution of the vorticity field and vorticity iso-contours at different instants of time using the reflective (left) and non-reflective (right) outflow condition on the right boundary.

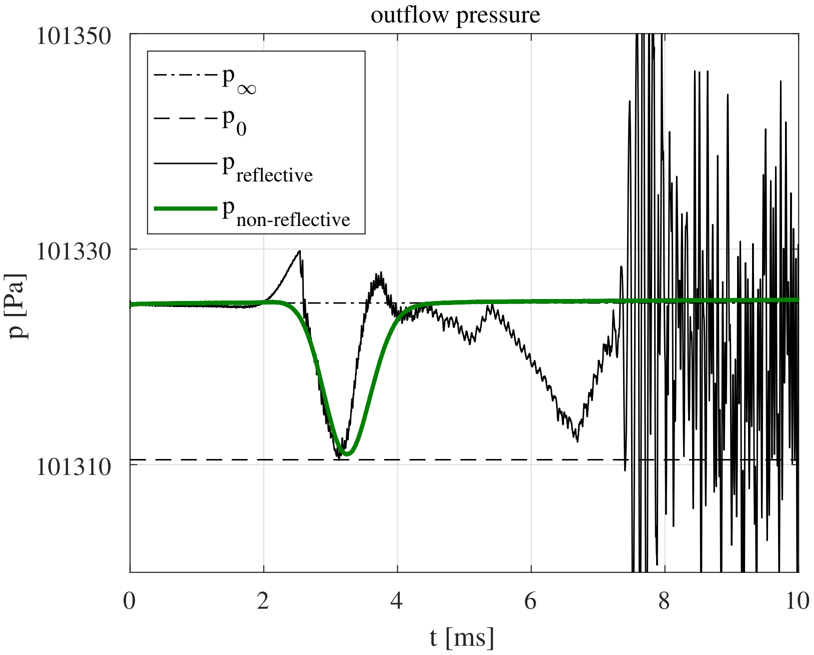

Figure 2.4: Time evolution of the pressure recorded in the centrepoint of the reflective and non-reflective outflow boundary plane.

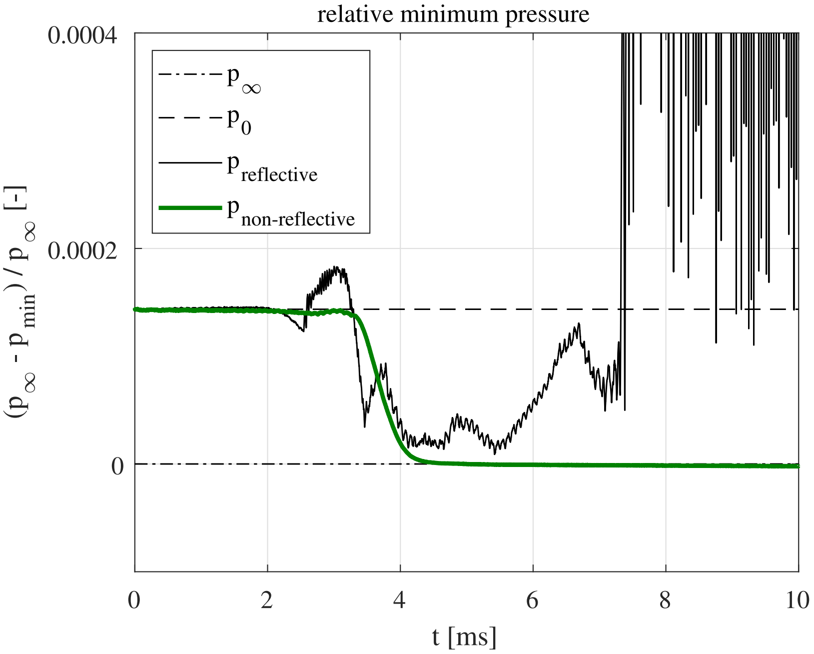

Figure 2.5: Time evolution of the relative minimum pressure within the entire computational domain using the reflective and non-reflective outflow condition.

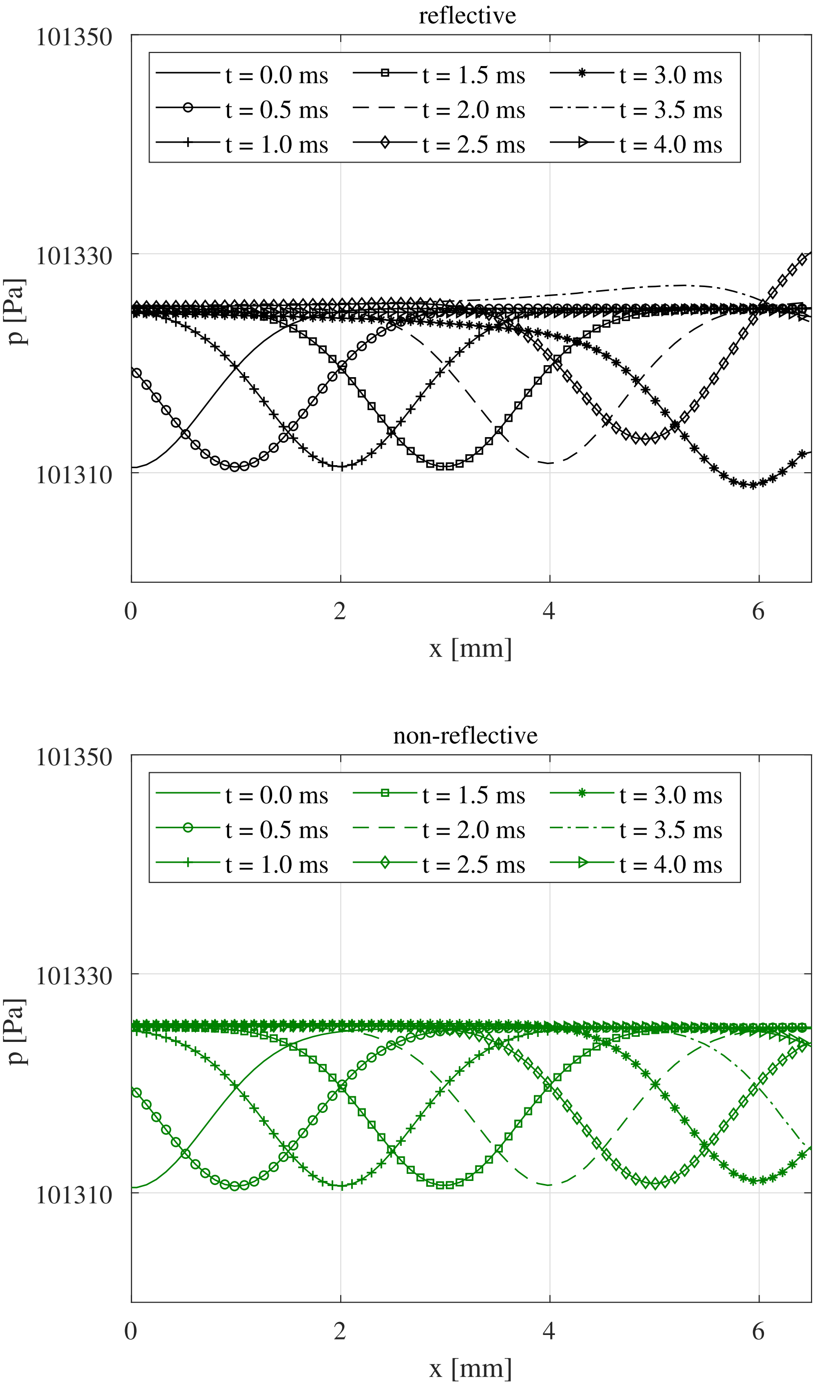

Figure 2.6: Pressure profiles extracted along the centreline at different instants of time using the reflective (top) and non-reflective (bottom) outflow boundary condition.

one-dimensional pressure profiles extracted along the centreline at different instants of time are given in Fig. 2.6 for the reflective and non-reflective case, respectively. The evolution of these profiles is consistent with the previous observations and shows how the reflective condition alters the shape of the initial pressure distribution.

2.6.3 Spherical wave propagation problem

The second test case consists of a three-dimensional, spherical acoustic wave that propagates inside of a cube with outflow conditions on all six faces and an edge length of $L = 0.013$ m. The pressure field is initialised as a spherical pressure pulse with $p_\infty = 1$ atm according to:

$$p = p_\infty \left[1 + \delta_a \exp\left(-\frac{r^2}{R_p^2} \right) \right] \tag{2.43}$$

where $r = \sqrt{x_i^2 + x_j^2 + x_k^2}$ is the distance from the cube's centrepoint, and where $\delta_a = 0.001$ and $R_p = 6.5 \times 10^{-4}$m (= 5% of L) represent, respectively, the amplitude and characteristic dimension of the pressure pulse. The flow field is initially at rest. Similar to the previous vortex problem, the initial density distribution can be computed from the equation of state by assuming the initial temperature field to be constant at $T_\infty = 300$ K.

Figure 2.7 qualitatively illustrates the temporal evolution of the spherical acoustic wave as it propagates outwards with the speed of sound. The wave's leading and trailing 'edges' are visualised via iso-surfaces of a single pressure value. Looking at the non-reflective case first, the wave front maintains its curvature while crossing the outflow boundary and induces virtually no reflection even when reaching the corners. A steady-state solution with uniform pressure distribution is attained at $t = 0.05$ ms once the wave has left the domain. In contrast, the reference case with reflective outflow conditions displays a vastly different behaviour. Upon approaching the domain boundaries, the acoustic wave is numerically displaced and appears to be partly 'sucked into' the outflow. Strong reflections and distortions are subsequently visible between $t = 0.0026$ and 0.03 ms. These reflections in turn cause spurious numerical artifacts, which persist even after the wave should have fully vacated the domain. Hence, the pressure field remains highly perturbed and the solution is unable to decay towards a steady-state with uniform pressure distribution and zero velocity.

One-dimensional profiles of the relative pressure are shown in Fig. 2.8 for the reflective and non-reflective case, respectively. These profiles extend from the centrepoint of the cubic domain to one of its boundaries and have been extracted at different time instants. The observed decrease in pressure magnitude over time is characteristic of expanding waves and therefore expected. However, in the reference case this trend is not continued once the

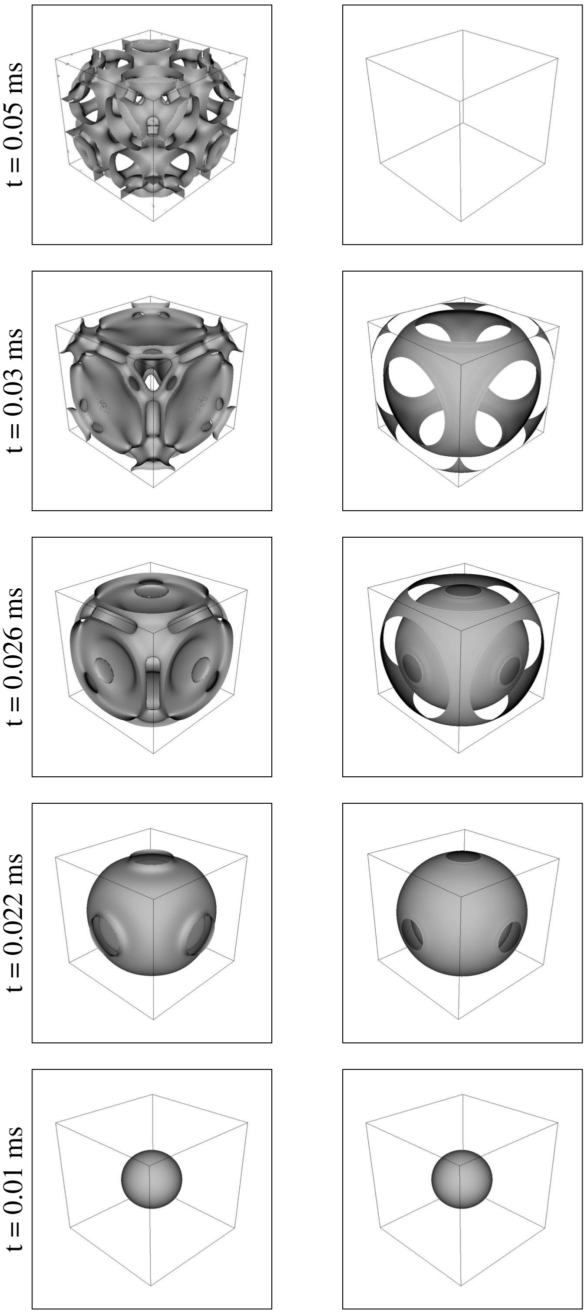

Figure 2.7: Evolution of the spherical pressure wave at different instants of time using a constant iso-surface of the pressure with, respectively, reflective (left) and non-reflective (right) outflow boundary conditions on all six faces of the cubic domain.

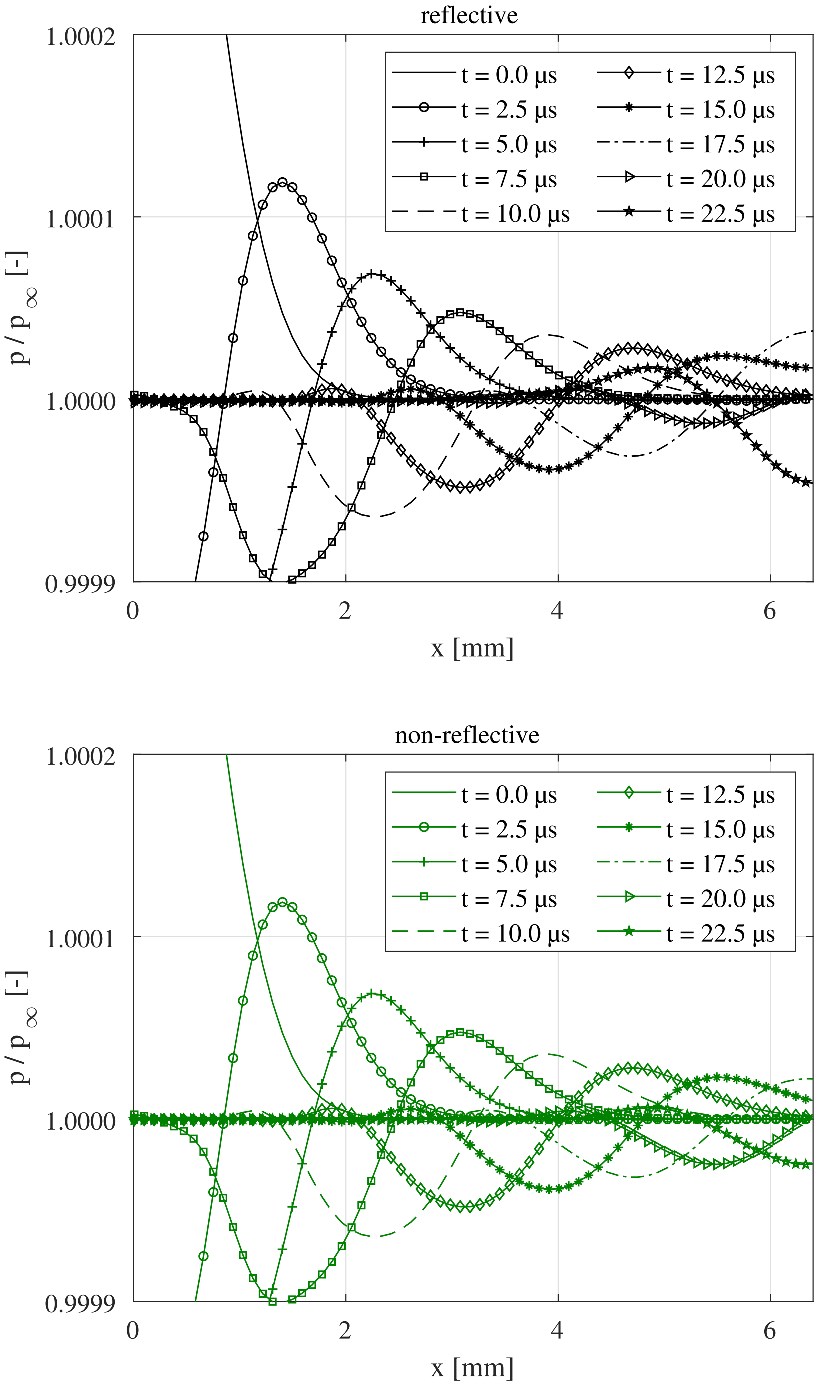

Figure 2.8: Relative pressure profile along the centreline at different instants of time using the reflective (top) and non-reflective (bottom) outflow boundary condition.

acoustic wave reaches the outflow condition. Instead, an unphysical increase of the pressure magnitude becomes evident, further underlining the importance of adequate boundary treatment when dealing with acoustic disturbances.

Chapter 3

Combustion model validation for partially premixed swirl flames

In this chapter, the potentially flame burning regime independent *pdf* approach / Eulerian stochastic fields method with reduced, yet comprehensive chemistry involving 15 steps and 19 species is applied to the PRECCINSTA model combustor including the treatment of wall heat transfer and resolution of the fuel-air mixing process. The specific objectives are to (*i*) evaluate the predictive capabilities of the transported *pdf* approach in the context of partially premixed combustion in a complex geometry and (*ii*) create a benchmark solution for the ensuing compressible simulation focusing on thermo-acoustic phenomena (Chapter 4) - acoustic effects are neglected by invoking an incompressible flow assumption. For this purpose, two different combustor operating conditions are simulated, one ‘stable’ and the other subject to experimentally observed flame oscillation, and the results are compared against available measurement data. This will allow for an assessment of the predicted flow field, flame topology, thermochemistry and species concentrations - i.e. CH_4, CO, carbon dioxide (CO_2) and hydroxide (OH) - as well as the influence of wall heat transfer.

The contents of this chapter have been published in Fredrich et al. (2019b).

3.1 Test case formulation

The lab-scale PRECCINSTA gas turbine model combustor, also known as Turbomeca burner, was first developed and studied as part of the EU (**E**uropean **U**nion) project ‘Prediction and Control of Combustion Instabilities in Industrial Gas Turbines’ (PRECCINSTA). The main objective of the project was to investigate the physics, prediction and control of combustor instabilities, Kelsall and Troger (2004).

3.1.1 Measurement campaign

Initially, the PRECCINSTA combustor was the subject of an experimental test campaign conducted by Meier et al. (2007) at the DLR (**D**eutsches Zentrum für **L**uft- und **R**aumfahrt; engl.: German Aerospace Center). It involved a lean, partially premixed, swirl-stabilised, methane-air flame at atmospheric conditions. Measurements were performed for three different operating conditions by varying the fuel mass flow rate to adjust the global equivalence ratio Φ_{global} of the mixture. An oscillating flame undergoing self-excited thermo-acoustic instabilities was observed at Φ_{global} = 0.7 - labelled oscillating flame case (1). Increasing the fuel mass flow rate to Φ_{global} = 0.83 resulted in a ‘stable’ flame case (2a) that did not exhibit any oscillations, whereas Φ_{global} = 0.75 produced a subtly pulsating, unstable flame case (2b); Table 3.1 summarises the different operating conditions investigated in the experimental campaign.

The combustor geometry is shown schematically in Fig. 3.1 and comprises four sections termed air plenum, injector unit, combustion chamber and exhaust pipe. Dry, pure air at atmospheric conditions is first fed into the air plenum through a large orifice. The ensuing injector unit was derived from a low-emission industrial design by Turbomeca. It consists of

Table 3.1: Summary of the three experimentally investigated combustor operating conditions, Meier et al. (2007).

Case	(1)	(2a)	(2b)
Flame behaviour	oscillating	‘stable’	unstable
Φ [-]	0.7	0.83	0.75
$\dot{m}_{air}$ [g/min]	734.2	734.2	734.2
$\dot{m}_{CH_4}$ [g/min]	30.0	35.9	32.3
P_{th} [kW]	25.1	30.0	27.0
$T_{ad(295K)}$ [K]	1834	2037	1915
Mixture fraction [-]	0.0391	0.0463	0.0418

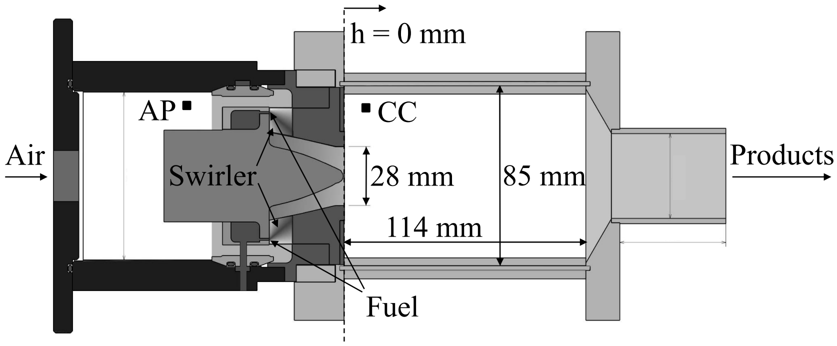

Figure 3.1: Schematic combustor geometry indicating the locations of the pressure probes AP (air plenum) and CC (combustion chamber). The burner nozzle exit / combustion chamber entry plane is defined as *h* = 0 mm.

a radial swirler followed by the burner nozzle with a conical central 'bluff body'. In between each of the 12 swirler vanes, fuel is injected into the air stream with high momentum to ensure good mixing. The combustion chamber is made of 1.5 mm thick quartz glass windows with a 85 x 85 mm cross section area and a total length of 114 mm. Its entry plane - aligned with tip of the burner nozzle cone - is defined as axial location *h* = 0 mm for all measurements. The burnt combustion products exit the combustion chamber through a converging duct and exhaust pipe into the atmosphere.

Comprehensive experimental data is available from laser Doppler velocimetry (LDV) measurements for cases (1) and (2b) as well as laser Raman scattering (Raman) for cases (1) and (2a). These were performed in one vertical plane along radial profiles with different axial locations. Additional planar laser-induced fluorescence (PLIF) and chemiluminescence of OH* (Hydroxyl Radical) were applied to visualise the flame structure in cases (1) and

Table 3.2: Systematic and statistical measurement uncertainties in the experiments, Meier et al. (2007).

Measured quantity	Systematic uncertainty	Statistical uncertainty
Axial location *h*	±0.5 mm	
Radial location *r*	±0.5 mm	
Velocity	<0.5%	±1.5-2%
Temperature	±3-4%	±2.5%
Mixture fraction	±3-4%	±1%
CH_4 mole fraction	+5-9%	±1-3%
CO_2 mole fraction	±3-5%	±7%
CO mole fraction	±5-10%	±20-50%

(2a). Relevant measurement uncertainties are presented in Table 3.2. These uncertainties are considered to be low, with the exception of the CO mole fraction, hence allowing a meaningful comparison of the quantitative results obtained from the LES and experiments.

3.1.2 Previous numerical works

Previous numerical works of the PRECCINSTA combustor include LES simulations of both the oscillating flame case (1), which are reviewed in Chapter 4, and the 'stable' flame case (2a). The latter provides a solid basis for the validation of LES combustion models and has been targeted for this specific purpose in a large number of works in the open literature: Ansari et al. (2015); Benard et al. (2019); Fiorina et al. (2010); Fredrich et al. (2019a,b); Galpin et al. (2008); Gövert et al. (2018); Guedot et al. (2015); Lecocq et al. (2011); Mercier et al. (2015); Moureau et al. (2011); Veynante and Moureau (2015); Volpiani et al. (2017); Wang et al. (2016). Comparisons between experiments and LES were first reported by Galpin et al. (2008) whose simulations predicted a higher burning rate - manifesting itself in a shortened flame length - and overestimated temperatures in the outer recirculation zone (ORZ). The latter was attributed to the assumption of adiabatic combustion chamber walls, which preclude the replication of any wall heat transfer occurring in the experiments. These findings were later reinforced in ensuing LES studies by other authors coming to similar conclusions. Simulations conducted by Gövert et al. (2018) achieved improved temperature and species mass fraction results by including non-adiabatic combustion chamber side walls and accounting for heat loss in the chemistry tabulation. Experimentally observed quenching of the flame in the outer shear layer (OSL) was not captured, however.

It should be mentioned that most of the above-cited numerical studies were performed using either simple chemistry involving very few species and reaction steps or tabulated chemistry based on fully premixed, laminar flame calculations. A more detailed skeletal reaction mechanism in combination with wall heat loss was applied in the work of Benard et al. (2019) resulting in good scalar predictions despite not accounting for the upstream premixing process between fuel and air. Franzelli et al. (2012) had previously underlined the importance of resolving the fuel injection, as opposed to prescribing a perfectly premixed mixture at the domain inlet. An overall better agreement between the simulated and measured statistical quantities, especially in terms of the mean and root mean square (RMS) values of the oscillating flame case, was obtained in their non-perfectly premixed simulations. More recently, Benard et al. (2019) and Fredrich et al. (2019b) achieved excellent agreement with experimental data including CO predictions. Their studies also showed that the application of non-adiabatic combustion chamber walls noticeably improves the near-wall scalar fields and can induce local extinction of the outer flame base in line with experimental observations.

3.2 Computational set-up

The incompressible flow assumptions invoked for the scope of this chapter are described below, followed by a detailed summary of the simulation parameters specific to the PRECCINSTA test case.

3.2.1 Incompressible flow assumptions

It should be noted that the term incompressible - in the current work - does not imply that the density remains constant throughout the flow field (the density does change as a function of temperature), but rather that it is independent of pressure variations, i.e. the flow cannot be compressed. For this to be the case, temporal changes in the thermodynamic pressure are assumed to be very small (i.e. constant), leading to $\partial p / \partial t \approx 0$. The enthalpy equation can furthermore be expressed in terms of the total enthalpy $h_t = h_s + \frac{1}{2} u_i^2$, so that the term $u_i \partial p / \partial x_i$ vanishes from the formulation. The dynamic part of the total enthalpy can then be neglected under the low-Mach number assumption, see e.g. Peters (2000), resulting in an expression analogous to that of Eq. (2.23), i.e.:

$$\frac{\partial \overline{\rho} \widetilde{\phi}_\alpha}{\partial t} + \frac{\partial \overline{\rho} \widetilde{u}_i \widetilde{\phi}_\alpha}{\partial x_i} = \frac{\partial}{\partial x_i} \left[\left(\frac{\mu}{\sigma} + \frac{\mu_{sgs}}{\sigma_{sgs}} \right) \frac{\partial \widetilde{\phi}_\alpha}{\partial x_i} \right] + \overline{\rho \dot{\omega}_\alpha} \tag{3.1}$$

where ϕ adopts the specific mole number of each species or the total enthalpy as appropriate. In this formulation, the scalar source term only includes the chemical source terms or the enthalpy source term without adding the time derivative of the pressure. The equation of state (cf. ideal gas law in Eq. 2.3):

$$\rho(T) = \frac{p_0}{RT} \tag{3.2}$$

is evaluated using a constant reference pressure p_0 equal to the combustor operating pressure, therefore causing the density to be a function of the local temperature only.

3.2.2 Simulation parameters

For the chemistry, the 15-step / 19 species CH_4 mechanism proposed by Sung et al. (2001) is used (see Section 2.4.2). In order to account for preheating of the mixture, as observed in the experiments of Meier et al. (2007), both air and methane are injected at a temperature of 320 K while the inflow pressure is equal to 1 bar. The inlet velocities have been adjusted accordingly to reflect the prescribed mass flow rates. The solution domain contains all of the main features of the geometry shown in Fig. 3.1, including the upstream air plenum and

Figure 3.2: Vertical cut through the generated mesh consisting of 2.7 million grid points distributed over 144 blocks and refined in the premixing as well as the flame region. The combustion chamber has a 85 x 85 mm^2 cross section area and a length of 114 mm.

short downstream duct. Figure 3.2 shows a vertical cut through the generated computational mesh consisting of 144 domains. It is refined in the mixing and reaction zones with cell edge lengths ranging from 0.1 to 1 mm in all three spatial directions, which are comparable to a Kolmogorov length scale of the order of 0.1 mm estimated in the experiments, Meier et al. (2007). Additionally, the mesh is refined towards the domain walls resulting in y^+ values between 20 and 30 in the swirler and nozzle regions, and below 10 in the combustion chamber with 5 to 10 grid points located within the wall boundary layer - where y^+ is the dimensionless wall distance. While such a mesh distribution is clearly not sufficient to resolve the detailed boundary layer turbulence structure accurately, it is likely to provide reasonably accurate time-averaged wall heat transfer rates, when used in conjunction with the approximate near wall treatment, Hoffmann and Benocci (1995); Piomelli and Balaras (2002).

Isothermal temperatures are fixed at the combustion chamber side walls (1400 K) and base plate wall (700 K) based on experimental measurements by Yin et al. (2017), whereas the central burner nozzle cone is assumed to be adiabatic. A separate simulation has shown that prescribing a wall temperature of 700 K to the tip of the central burner nozzle cone causes the flame to consistently lift off and fully detach from the nozzle. Consequently, the mean temperature profiles (shown later in Fig. 3.9) in this region are significantly lowered; well below the desired experimental values. Radiative heat transfer is included in the simulations through the radiation model described in Barlow et al. (2001) using the assumption of optically thin transfer between a given fluid element in the flame and the cold surroundings. The overall heat losses incurred by radiation and wall heat transfer respectively, amount to about 5% and less than 1% of the total integrated heat release rate. A more sophisticated approach to modelling heat transfer - that goes beyond the scope of this work - can be found in e.g. Kraus et al. (2018).

3.3 Results and discussion

Results of the oscillating flame case (1) with $\Phi_{global} = 0.7$ are presented and analysed first followed by the 'stable' flame reference case (2a). Both simulations were allowed to develop for 75 ms of physical time prior the collection of statistics. This corresponds to about 5 combustor flow-through times based on the bulk flow velocity through the radial swirler, burner nozzle and combustion chamber. Statistics were subsequently collected over a further 105 ms of physical time or 7 combustor flow-through times. The total computational cost for each case amounts to about 200,000 CPUh (**C**entral **P**rocessor **U**nit **h**ours) on the ARCHER UK National Supercomputing Service.

3.3.1 Flow field and flame topology

In order to visualise both the fuel injection and mixing process within the swirler as well as the flame structure and its location in the combustion chamber, iso-surfaces of the instantaneous CH_4 mass fraction and heat release rate are shown in Fig. 3.3. An inhomogeneous mixture fraction distribution along the flame surface - indicating local stratification of the flame - in conjunction with strong swirling of the flow can be observed. Figure 3.4 further displays instantaneous and mean LES snapshots of the axial velocity, temperature and mixture fraction illustrating the highly turbulent flow and flame behaviour. Distinct variations in the mixture fraction distribution may be interpreted as a potential indicator for the partially premixed nature of the combustor (discussed further in Section 3.3.4).

Radial profiles of the mean velocity at different downstream locations in the mid-plane are given in Fig. 3.5 allowing for a quantitative comparison between experiment and simulation. When characterising the flow field, three distinctive flow regions can be identified. An inner recirculation zone (IRZ), created by the swirling flow to stabilise the flame, is easily detected due to the negative velocities around the combustor centreline. The conically shaped, swirling jet of unburnt gases is characterised by high axial velocities peaking at 40 m/s and high radial velocity magnitudes reaching approximately 20 m/s. Lower velocities towards the combustion chamber walls indicate the transition into an ORZ, which is located outside of

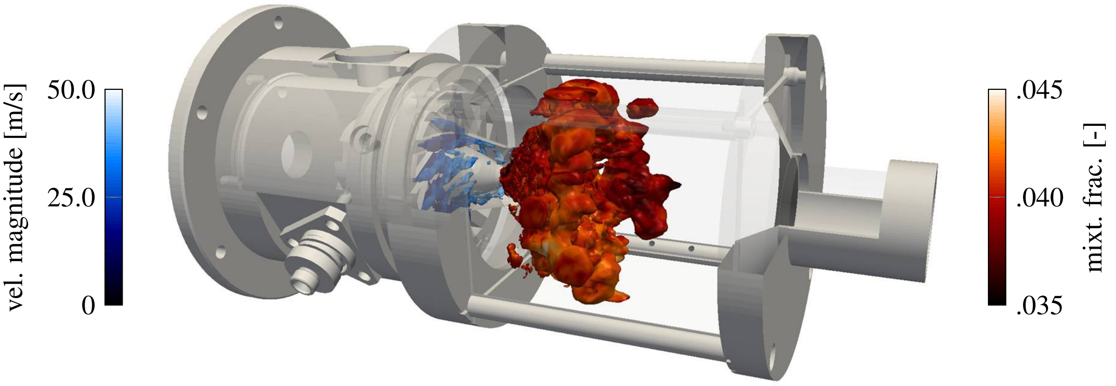

Figure 3.3: Iso-surfaces of the instantaneous CH_4 mass fraction (left) and heat release rate (right) coloured by, respectively, the velocity magnitude and mixture fraction - $\Phi_{global} = 0.7$.

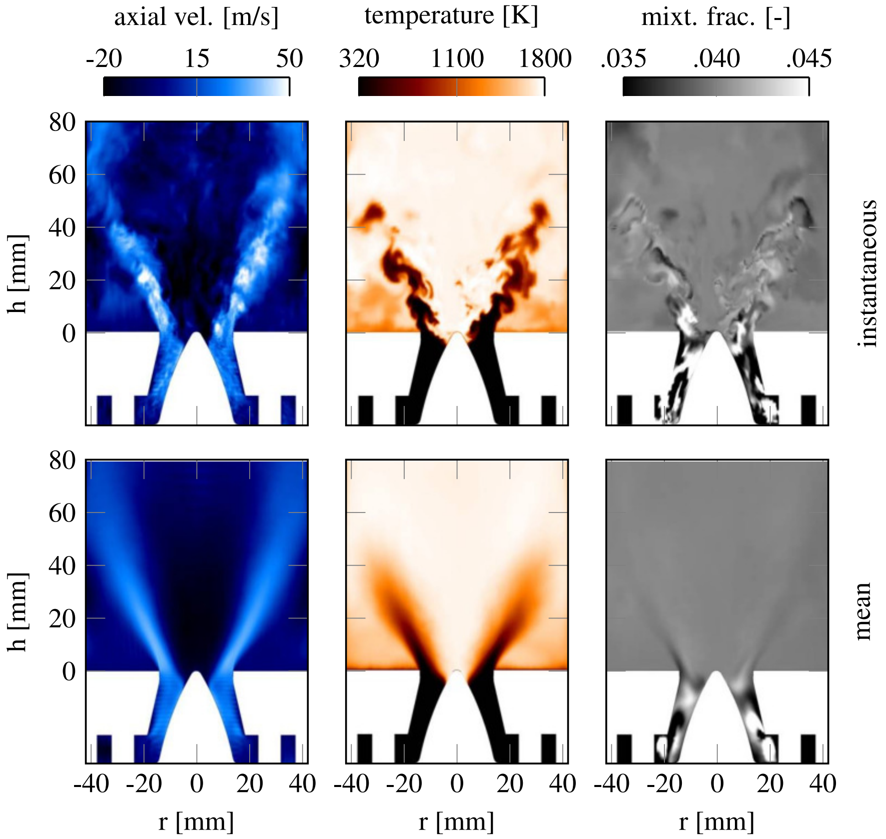

Figure 3.4: LES snapshots of the instantaneous (top) and mean (bottom) axial velocity, temperature and mixture fraction - $\Phi_{global} = 0.7$.

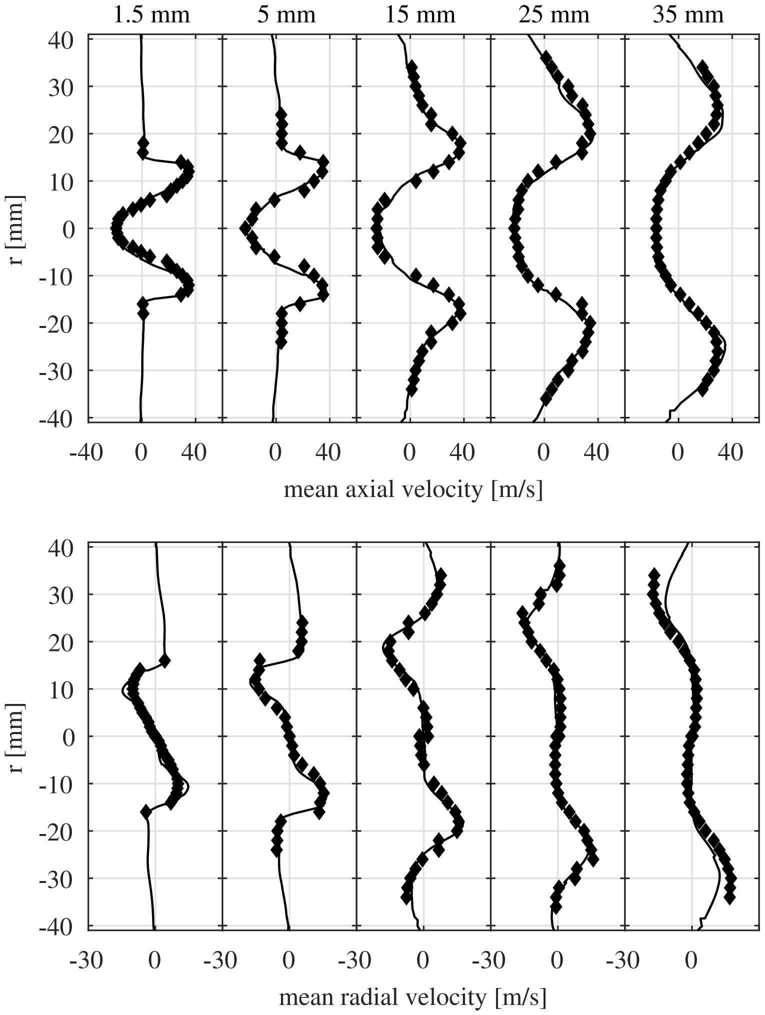

Figure 3.5: Radial profiles of the mean axial (top) and radial (bottom) velocity from the experiment (♦) and LES (—) - $\Phi_{global} = 0.7$.

the experimentally measured region. With increasing downstream position, the high velocity jet widens and shifts towards the combustion chamber walls reducing the size of the ORZ while widening the IRZ. All of the above-mentioned flow characteristics are captured in the simulation and the quantitative velocity results match experimental data with very high accuracy.

3.3.2 Thermochemical properties

The simulated thermochemistry results can be analysed in terms of the instantaneous relation between temperature and mixture fraction as depicted in Fig. 3.6. Looking at the evolution of the temperature-mixture fraction distribution with downstream position, a shortened flame length can be determined corresponding to an overestimated burning rate. Compared to the experiment, the simulated temperatures approach the adiabatic flame temperature at a slightly quicker rate. Hence, at h = 15 mm for example, the simulated minimum temperatures are marginally higher compared to the experimental ones. This trend continues at h = 30 mm where all of the LES points have moved into either the reaction zone with intermediate temperatures or the fully burnt region, whereas the measurements still show a number of points remaining within the fresh gas region below $\sim$400 K. Finally, at h = 80 mm, both experimental and LES points are scattered exclusively around the adiabatic flame temperature indicating a fully burnt mixture.

In terms of the mixture fraction distributions, experimental extreme values of about 0.015 and 0.08 are observed. The simulation does not reproduce such a wide range of mixture fraction values but instead predicts a somewhat higher degree of premixing. Increased premixing tends to affect the burning rate, and may therefore be identified as a potential reason for the shortened flame length, Galpin et al. (2008). The expanded experimental mixture fraction distribution is likely to be caused by the occurrence of thermo-acoustic instabilities periodically varying the amount of fuel in the mixture, as established experimentally by Meier et al. (2007) and numerically by Franzelli et al. (2012). Different impedances of the fuel and air supply lines are almost certainly responsible for the equivalence ratio variations (discussed later on in Chapter 4). Note that the incompressible flow assumptions applied here will impede the propagation of acoustic waves, thus prohibiting the reproduction of thermo-acoustic instabilities. Nonetheless, the overall computed, instantaneous temperature-mixture fraction correlation matches the experimental results including a reasonably estimated mixture fraction distribution.

A more detailed analysis of the thermochemistry at the first downstream location (h = 6 mm) close to the combustion chamber entry plane is carried out based on Fig. 3.7. The lower temperature limit suggests that the assumed inlet temperature of 320 K recreates experimental

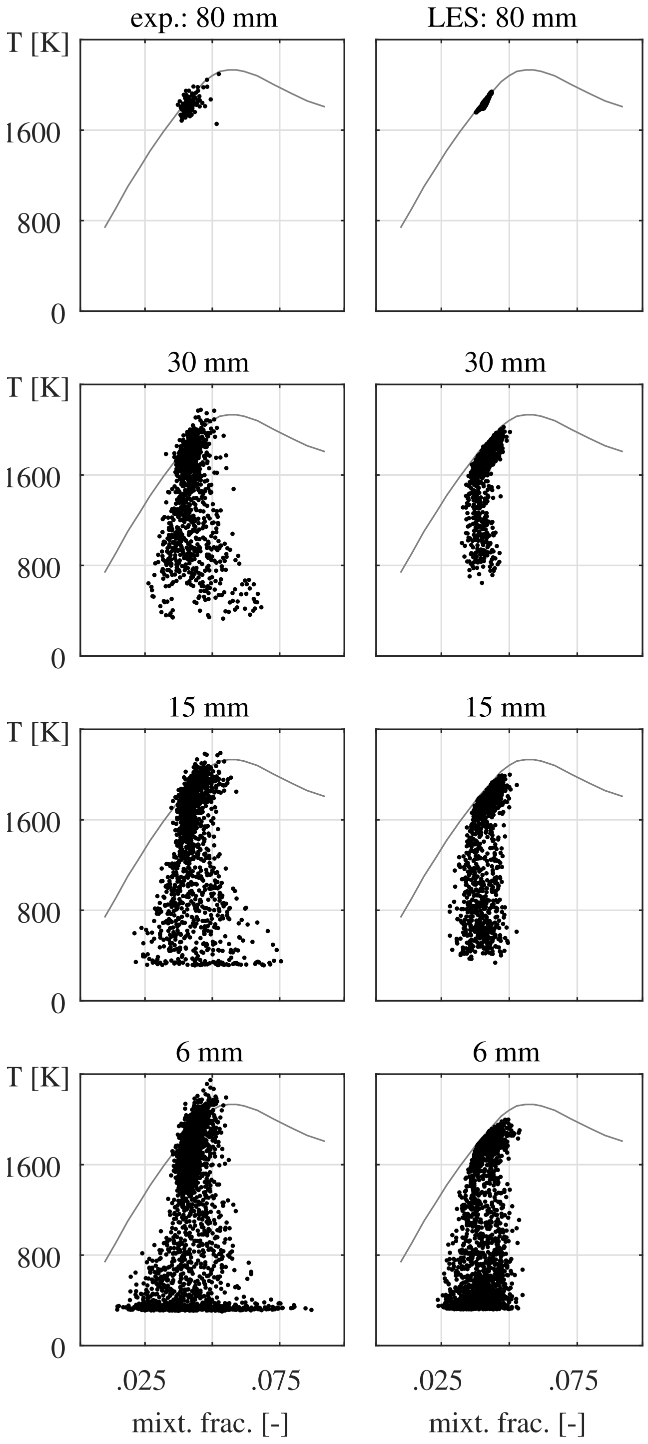

Figure 3.6: Experimental (left) and LES (right) scatter plots of the instantaneous temperature versus mixture fraction - $\Phi_{global} = 0.7$. The solid line represents the adiabatic flame temperature.

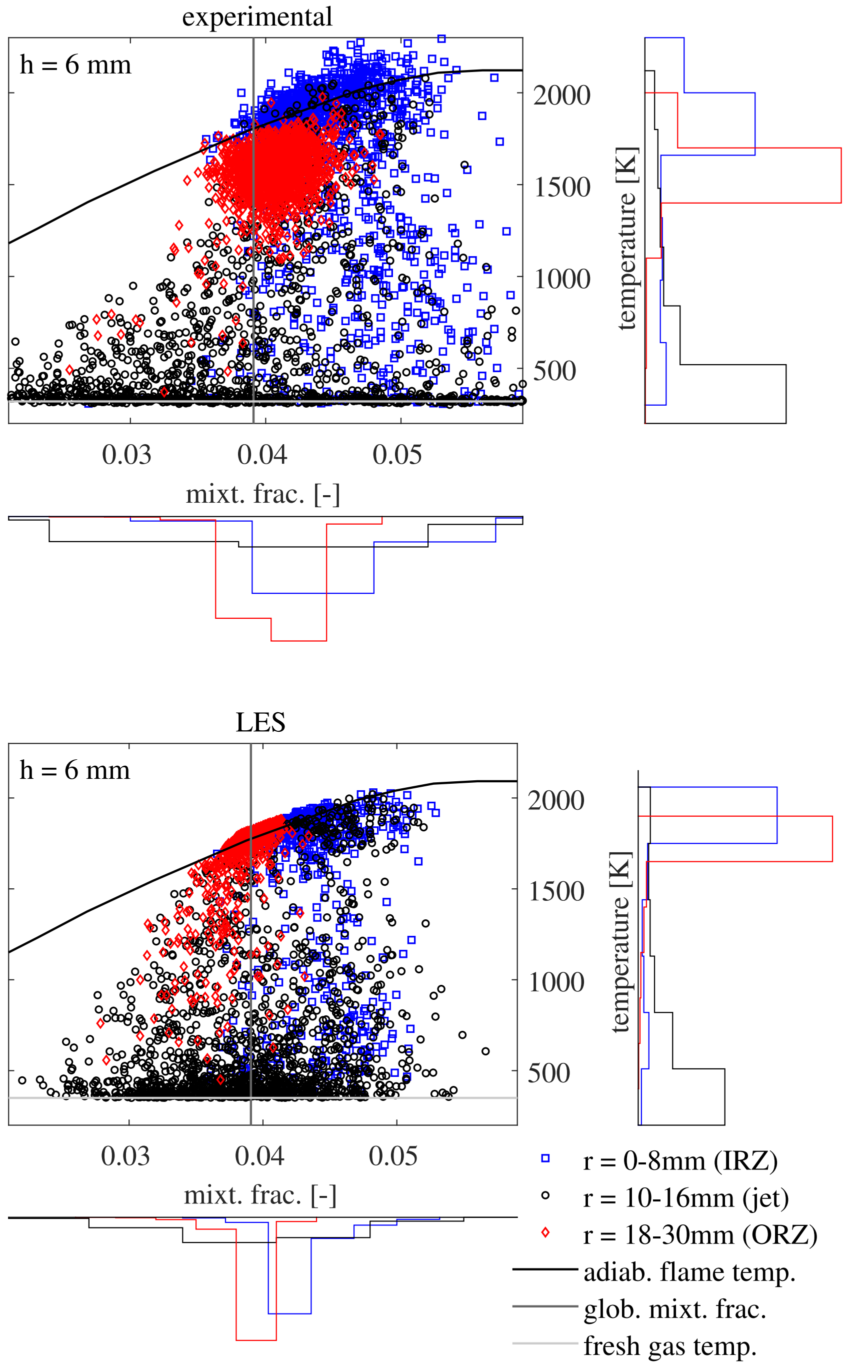

Figure 3.7: Instantaneous temperature-mixture fraction correlation from the experiment (top) and LES (bottom) at the first downstream location (h = 6 mm) including marginal histograms - $\Phi_{global} = 0.7$. The solid lines represent the global mixture fraction and fresh gas temperature at 0.0391 and 320 K, respectively.

preheating of the mixture. Also displayed in Fig. 3.7 are the marginal histograms of the temperature and mixture fraction at three different radial regions representing the IRZ, jet and ORZ. These are scaled differently (they both integrate to unity) so that only qualitative comparisons are possible. The locations of the temperature and mixture fraction maxima are in reasonable agreement for all three regions while the experimental point distributions are, as expected slightly more spread out. The measured and simulated histograms are in reasonably good qualitative agreement although the simulated temperature histogram shows somewhat higher values than those measured. Burnt gases in the IRZ and ORZ are well captured by the LES as evidenced by the high temperatures and narrow range of mixture fraction values in these regions. Significantly higher levels of unmixedness are found in the jet of mostly fresh reactants with low temperatures (r $\approx$ 10 - 16 mm) in both the experiment and simulation.

3.3.3 Wall heat transfer and species concentrations

Images of the OH intensity are displayed in Fig. 3.8 in a strictly qualitative comparison between experiments and simulation (for case Φ_{global} = 0.83; representing a ‘stable’ flame further discussed in Section 3.3.4). Generally, the LES reproduces the flame structure despite not being able to capture the smallest features visible in the OH PLIF measurements. Wrinkling of the flame front appears to increase with downstream position where most of the smaller structures are found. The inclusion of non-adiabatic walls improves the mean flame shape and general OH concentration especially in the ORZ. Moreover, a reduction in the maximum values of OH becomes evident compared to the adiabatic simulation. Similar to the experimental images, flame quenching is observed in the outer shear layer of the incoming jet leading to lift-off of the external flame front, Benard et al. (2019). This effect was not reported in the work of Gövert et al. (2018) presumably because only heat loss to the combustion chamber side walls (quartz glass) was taken into account; base plate wall heat transfer was neglected. Thus, despite only inducing very little total heat loss (lower than 1% compared to the integrated heat release rate), wall heat transfer impacts the simulation by introducing flame lift-off and increasing the length, width and outer spreading angle of the flame. The differences that occur between the mean inner and outer flame fronts in the adiabatic simulation are almost certainly due to the variation in equivalence ratio between these two regions - see Fig. 3.4.

Figure 3.9 presents radial profiles of the temperature with and without wall heat transfer treatment. The general mean temperature trends including the location of the temperature dip representing unburnt gases are well reproduced by the LES. High temperatures near the centreline characterise the IRZ where burnt gases are transported back to the flame front with

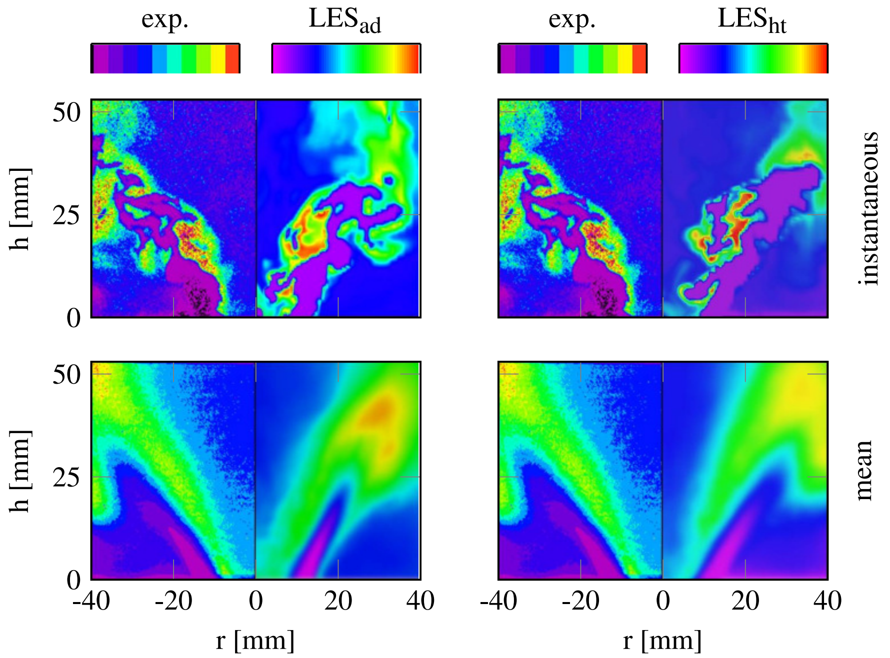

Figure 3.8: Qualitative comparison of measured OH PLIF intensities with those of LES with fully adiabatic walls (left) and with wall heat transfer (right) - Φ_{global} = 0.83. The top figures represent a snapshot of the results whilst the lower show mean values. The colour scales of the measurements and simulations are very closely similar.

the purpose of stabilising the flame. Complementing the temperature results, radial profiles of the CO_2 and CH_4 mass fractions with wall heat transfer are shown in Figs. 3.10 and 3.11. Deviations between the measured and simulated temperature, CO_2 and CH_4 mass fraction profiles are observed as a result of the under-predicted flame length first determined from Fig. 3.6. Hence, an earlier consumption of methane occurs leading to a local overestimation of CO_2. This discrepancy is mainly visible at the first three downstream locations and inside of the inner shear layer with errors of up to 15%. In accordance with the measurements, at h = 80 mm, the LES temperatures reach a homogeneous ‘equilibrium’ state around the adiabatic flame temperature of just over 1800 K and the methane is fully consumed.

From the RMS profiles depicted in Figs. 3.9, 3.10 and 3.11 it becomes clear that the temperature, CO_2 and CH_4 mass fraction fluctuations are not sufficiently captured towards the combustor centreline. In this region, a maximum temperature discrepancy of about 450 K can be observed at h = 10 mm. Again, the method’s current inability to reproduce an oscillating flame undergoing self-excited thermo-acoustic instabilities serves as a potential explanation for the underestimation. In a previous LES of the PRECCINSTA test case, Franzelli et al. (2012) have shown an improvement of RMS temperature results close to the

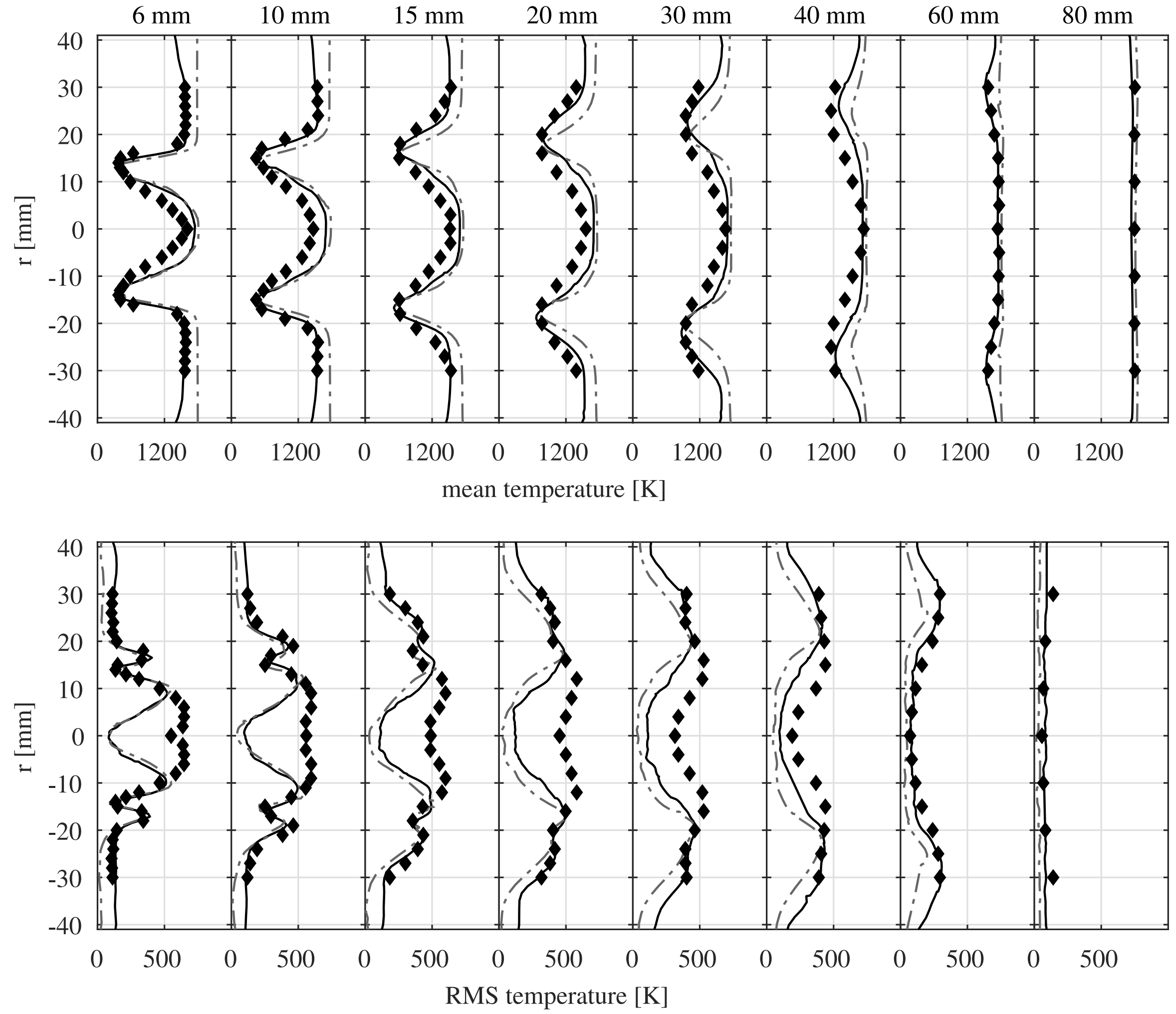

Figure 3.9: Radial profiles of the mean (top) and RMS (bottom) temperature from the experiment (♦), an LES with fully adiabatic walls (-·-) and the LES accounting for wall heat transfer (—) - $\Phi_{global} = 0.7$.

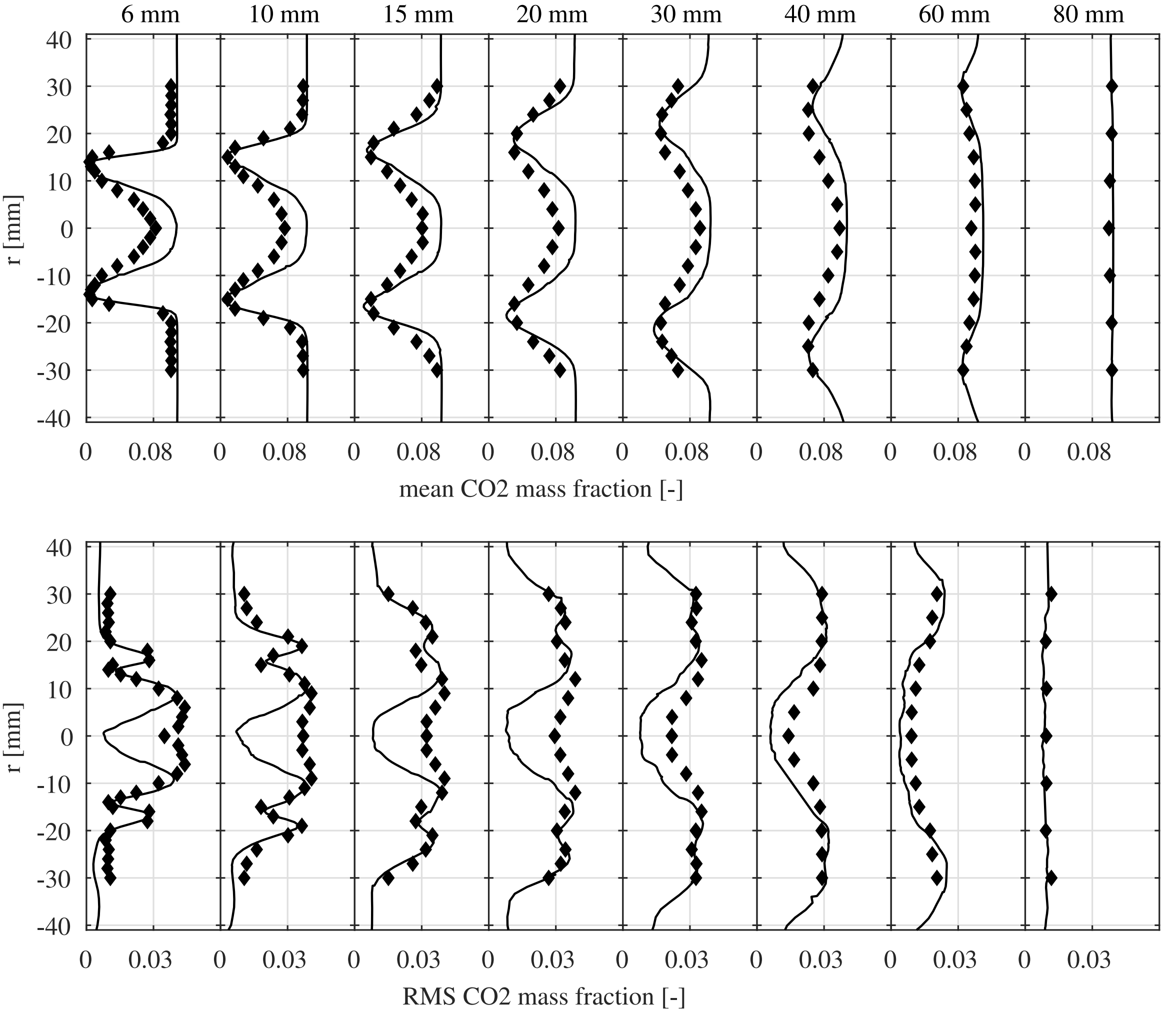

Figure 3.10: Radial profiles of the mean (top) and RMS (bottom) CO_2 mass fraction from the experiment (♦) and LES (—) - $\Phi_{global} = 0.7$.

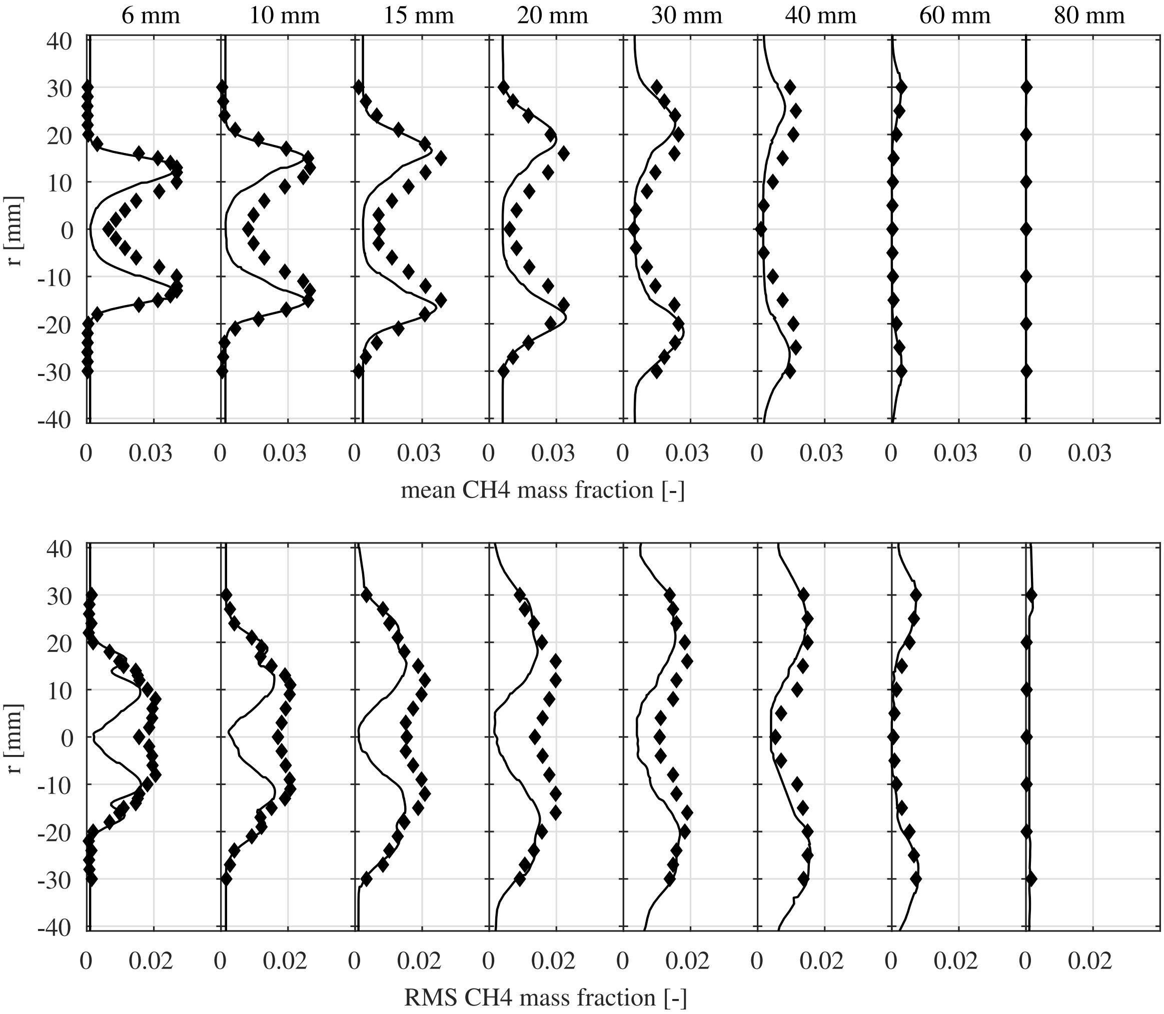

Figure 3.11: Radial profiles of the mean (top) and RMS (bottom) CH_4 mass fraction from the experiment (♦) and LES (—) - $\Phi_{global} = 0.7$.

centreline by resolving flame oscillation using a fully compressible flow solver. Despite this shortcoming, RMS temperature profiles away from the centreline are accurately predicted.

Finally, by examining the mean and RMS temperature results of the adiabatic and non-adiabatic LES cases with experimental data in Fig. 3.9, unaccounted heat loss can be identified as the source of local temperature overestimation adjacent to the combustion chamber walls in the fully adiabatic LES. Furthermore, and in accordance with observations made in the above comparison of OH images (Fig. 3.8), wall heat transfer noticeably improves the flame length, width and outer spreading angle in the non-adiabatic case. Overall, both the mean and RMS temperatures are in better agreement with measurements when wall heat transfer is included in the simulation.

3.3.4 'Stable' flame reference case

An additional 'stable' flame corresponding to the experimental combustor operating condition (2a) with an equivalence ratio of Φ_{global} = 0.83 was simulated to eliminate the influence of thermo-acoustic instabilities on the time-averaged results. Heat transfer at the combustion chamber walls was included based on the findings of the previous Section 3.3.3. The flame index FI proposed by Yamashita et al. (1996) and defined as the scaled product of the methane and oxygen (O_2) mass fraction gradients:

$$FI = 0.5 \cdot \left(\frac{\nabla \widetilde{Y}_{CH_4} \cdot \nabla \widetilde{Y}_{O_2}}{|\nabla \widetilde{Y}_{CH_4} \cdot \nabla \widetilde{Y}_{O_2}|} + 1 \right) \tag{3.3}$$

is displayed on the left-hand side of Fig. 3.12. It has been computed with a threshold on the minimum heat release rate to isolate the reacting layer, such that values below 0.5 represent a flame front burning in the diffusion regime as opposed to values above 0.5 indicating a premixed regime. The 'stable' case is clearly dominated by premixed flame propagation showing that the wide distribution of local mixture fraction values does not directly correlate to large regions of non-premixed combustion. However, small regions influenced by diffusion conditions do exist confirming that the premixing is indeed not globally perfect. These diffusion regions can be found behind the premixed flame front in areas of locally high OH concentrations around the inner shear layer and at the maximum extension of the flame (refer to the instantaneous images in Fig. 3.8). Note that the oscillating flame case is expected to have a lower overall degree of premixing due to the occurrence of thermo-acoustic instabilities, Franzelli et al. (2012); Meier et al. (2007). The simulated and experimental mean flame topology are visualised on the right-hand side of Fig. 3.12 illustrating the flame's characteristic V-shape. Here, the flame length, spreading angle and

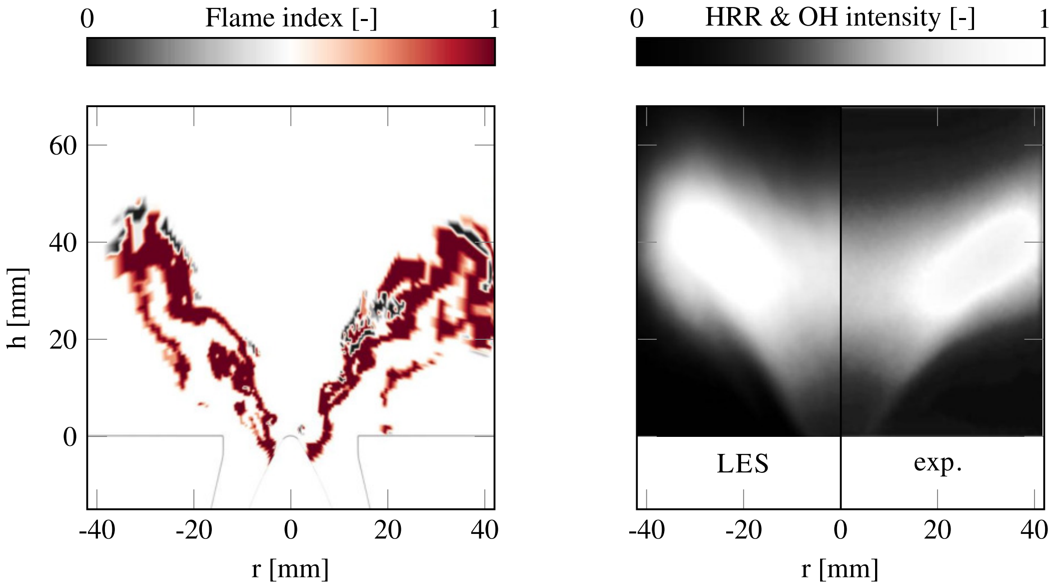

Figure 3.12: Instantaneous snapshot of the simulated flame index (left) and line-of-sight integration of the LES mean heat release rate (HRR) compared to an experimental mean OH* chemiluminescence image (right) - $\Phi_{global} = 0.83$. The experimental image (Meier et al., 2007) was converted into greyscale.

region of high intensities are well reproduced by the LES leading to a qualitatively very similar looking flame topology.

Figures 3.13, 3.14 and 3.15 show radial profiles of the temperature and the CO_2 and CH_4 mass fractions, exhibiting a remarkable agreement with the measurements. A minor over-prediction of RMS CO_2 values in between the two double peaks at the first downstream location (h = 6 mm) indicate a slightly less stable flame base in the simulation. The mean CH_4 mass fraction profiles further reveal a marginally shorter and more narrow jet of fresh reactants penetrating into the combustion chamber. Due to the increased global equivalence ratio, maximum values for the temperature and CO_2 mass fraction of about 2000 K and 0.125 are, accordingly higher compared to 1850 K and 0.105 in the oscillating flame case.

The LES and experimental RMS scalar values around the combustor centreline ($r <$ 8 mm) and close to the combustion chamber entry plane (h = 6 mm and 15 mm) are both significantly lower in relation to the oscillating flame case (Figs. 3.9, 3.10 and 3.11). These results imply that the large deviations observed in the oscillating case may indeed be linked to the combustor's thermo-acoustic behaviour. Stopper et al. (2013) reported a similar effect in their experimental study of an industrial combustor comparing a ‘quiet’ to an oscillating flame case. They argued that elevated RMS fluctuations in the oscillating case were caused

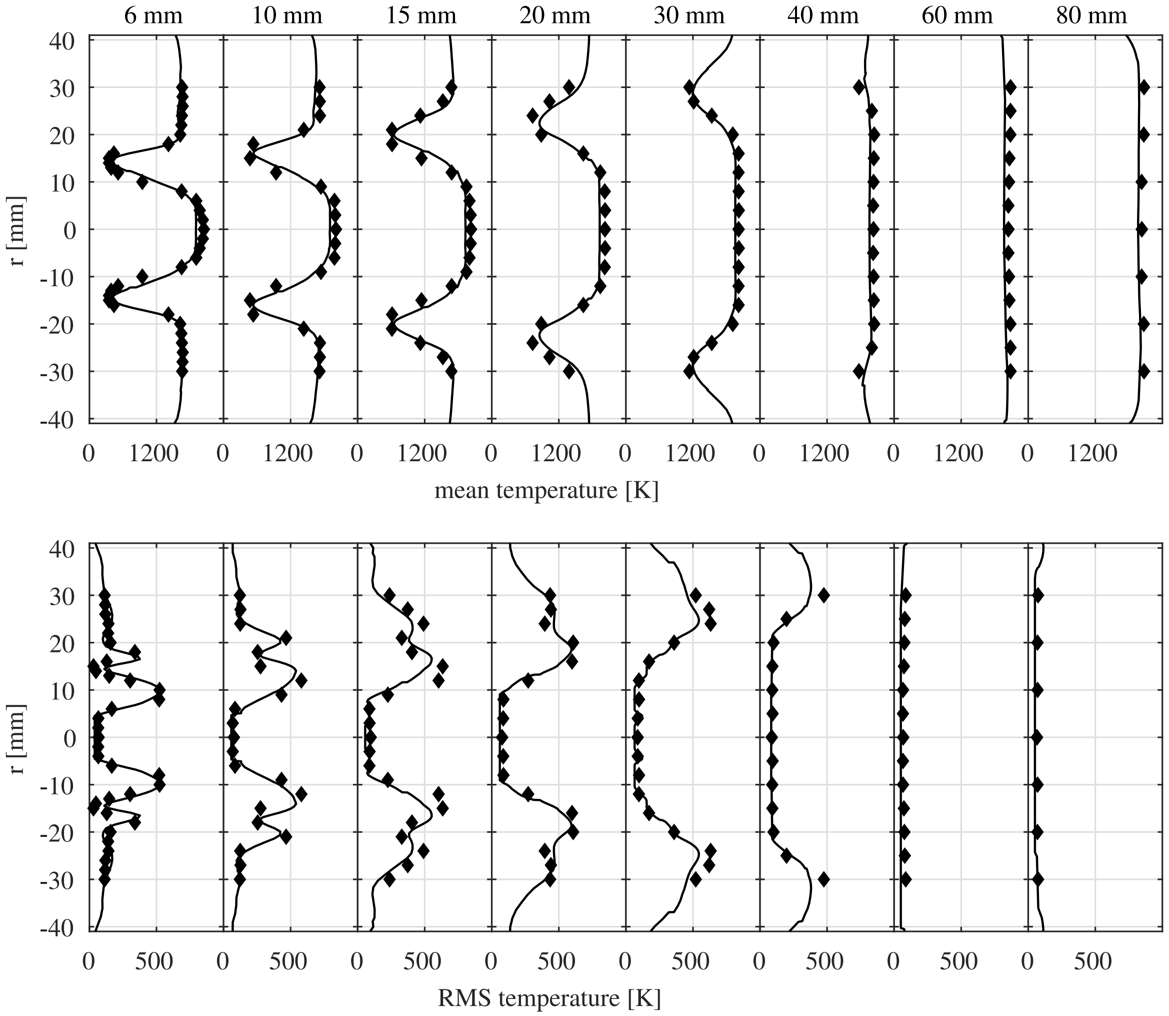

Figure 3.13: Radial profiles of the mean (top) and RMS (bottom) temperature from the experiment (♦) and LES (—) - Φ_{global} = 0.83.

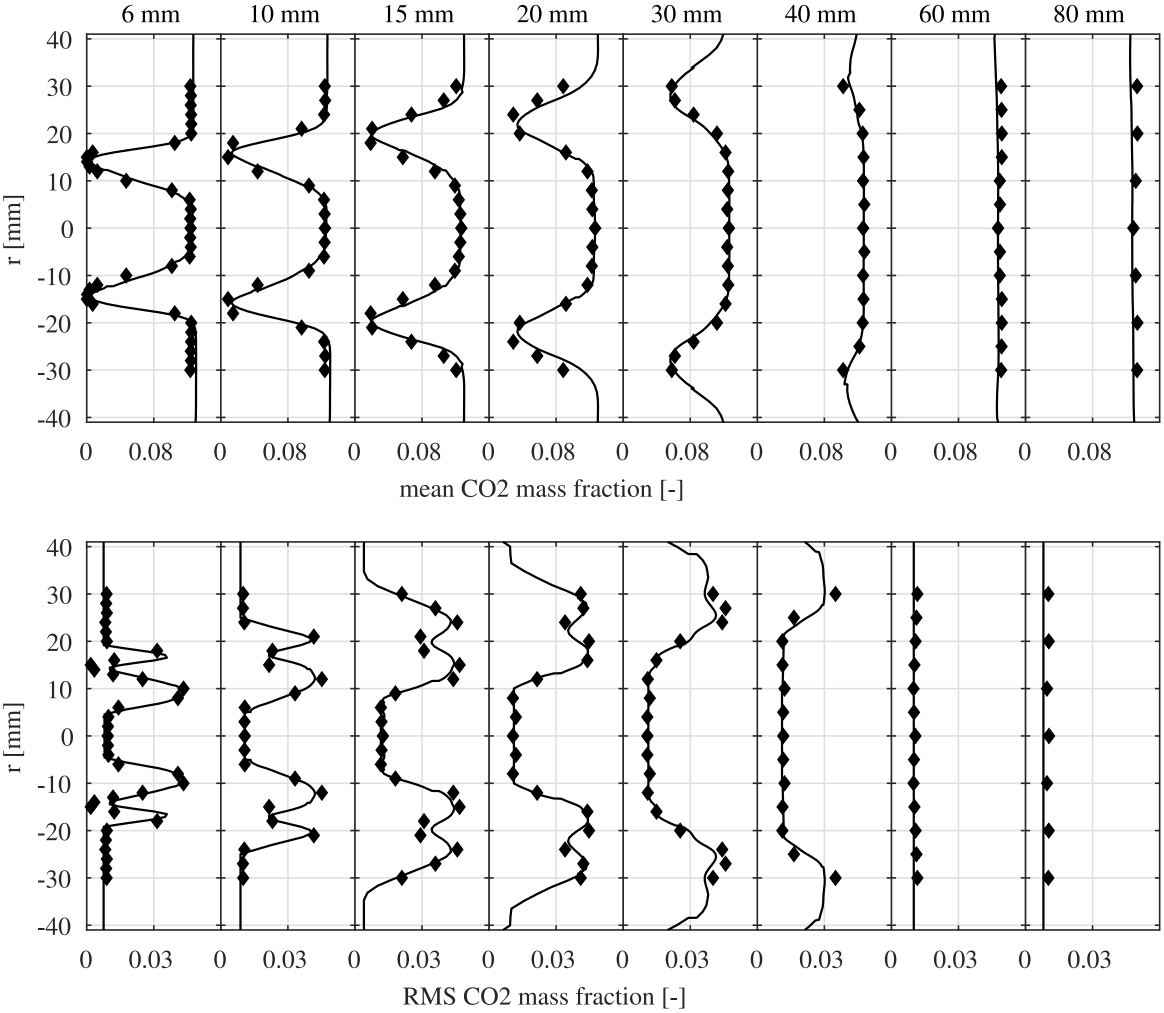

Figure 3.14: Radial profiles of the mean (top) and RMS (bottom) CO_2 mass fraction from the experiment (♦) and LES (—) - $\Phi_{global} = 0.83$.

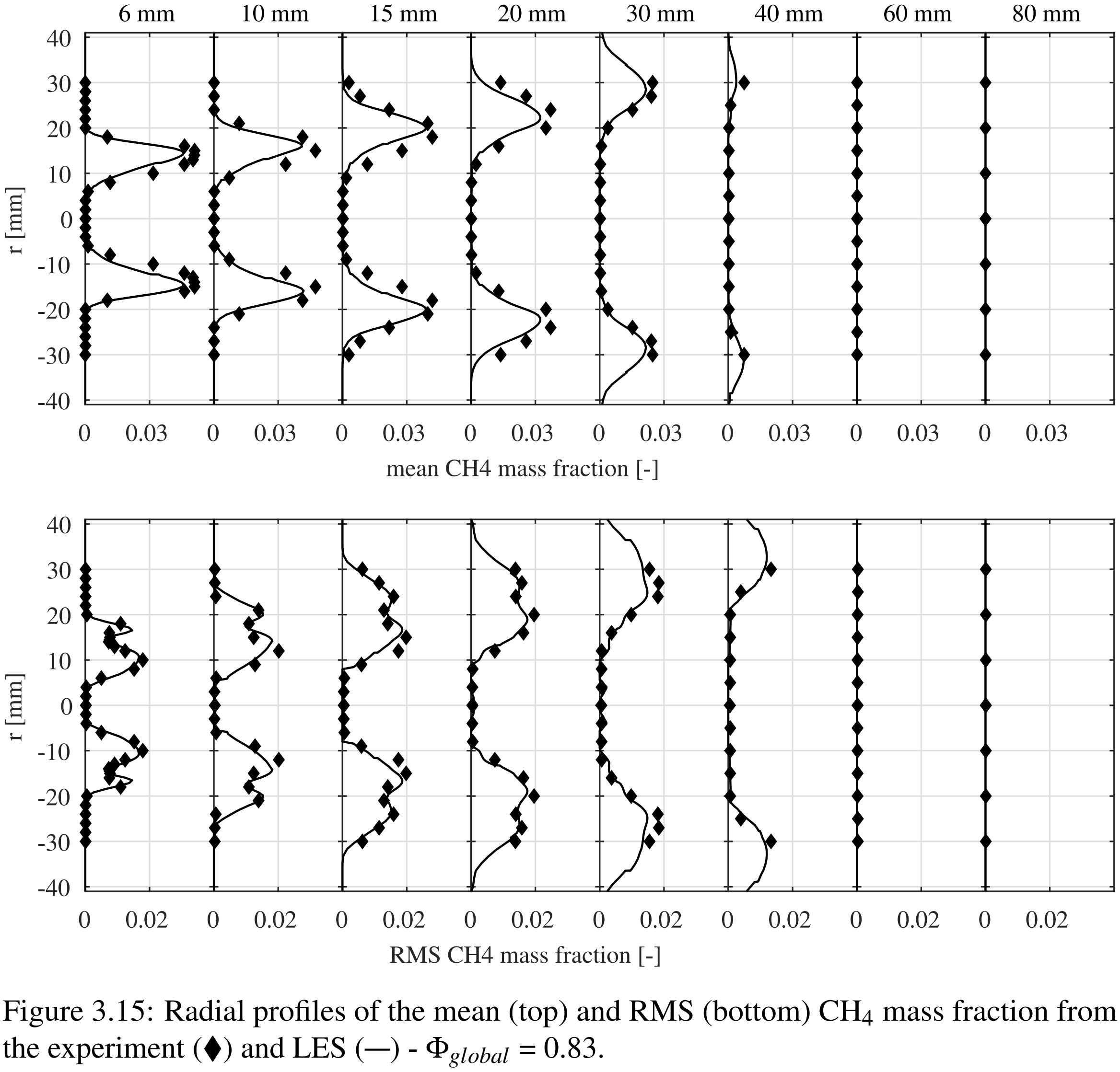

Figure 3.15: Radial profiles of the mean (top) and RMS (bottom) CH_4 mass fraction from the experiment (♦) and LES (—) - $\Phi_{global} = 0.83$.

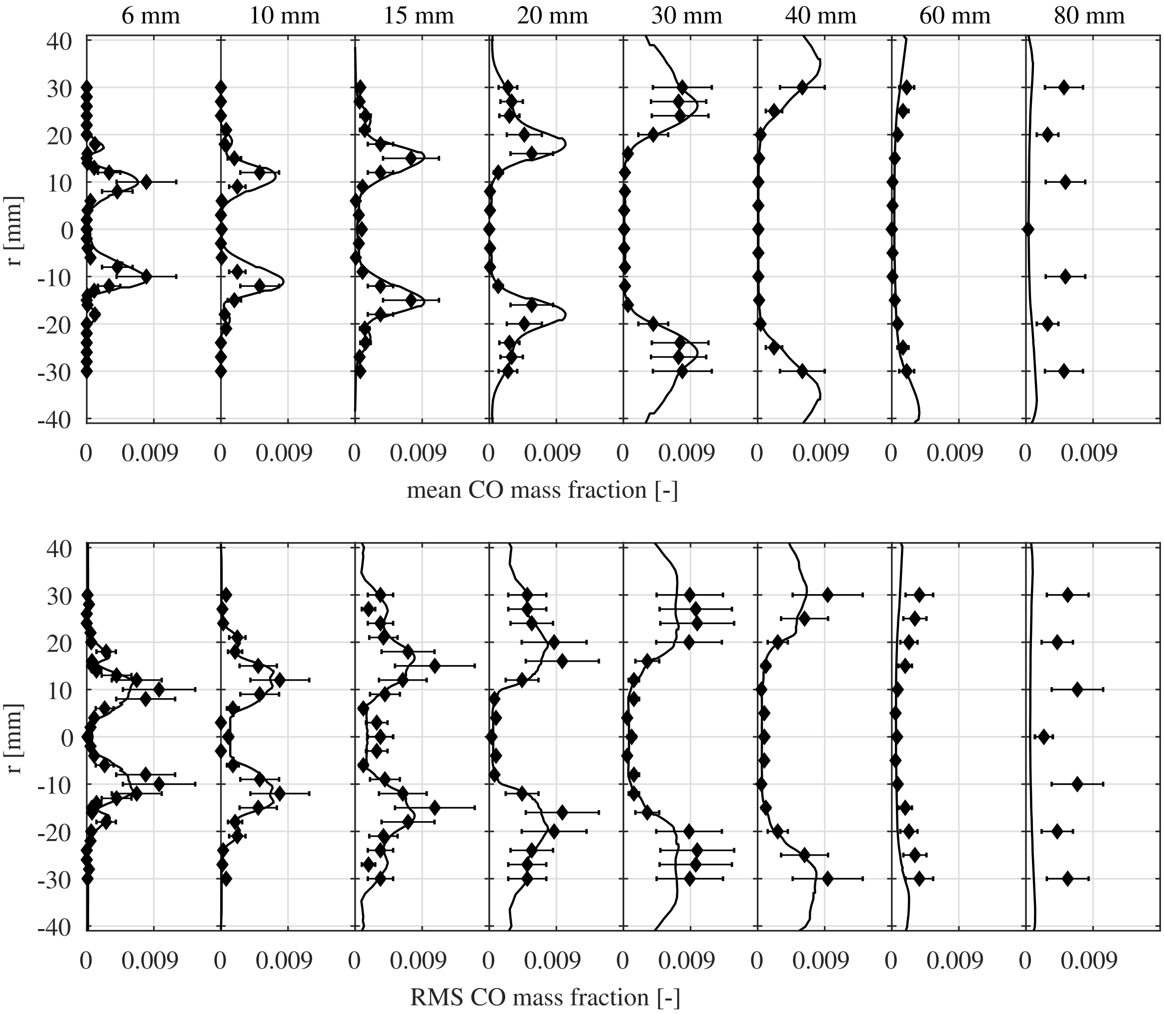

Figure 3.16: Radial profiles of the mean (top) and RMS (bottom) CO mass fraction from the experiment (♦) and LES (—) - Φ_{global} = 0.83. Error bars are taken from the experimental data based on Table 3.2.

by phase-dependent temperature variations induced by thermo-acoustic instabilities. This will also be shown later in Chapters 4 and 5 of the present work.

Lastly, the computed mass fraction profiles of CO are displayed in Fig. 3.16. In general, the mean and RMS profiles are in alignment with experimental data; outside of the final downstream position at h = 80 mm where the measured CO concentration seems very high. The mean profiles indicate maximum simulated values of up to 0.1, which are slightly above the maximum experimental values of about 0.08. The computed RMS maxima are consistently underestimated at all downstream locations, however, profiles outside of the peak region are well captured. Overall, good agreement is achieved , particularly considering the large uncertainties in the CO measurements - up to 50% - reported in Meier et al. (2007).

3.4 Concluding remarks

The PRECCINSTA gas turbine model combustor was successfully simulated using LES in conjunction with a transported *pdf* approach accounting for turbulence-chemistry interaction. Simulations were carried out for two different combustor operating conditions representing an oscillating and a ‘stable’ flame. The flow field was shown to be in excellent agreement with experimental data supporting the applicability of the solver with a dynamic sub-grid turbulence model to highly swirling flows. The mean temperature, CO_2 and CH_4 mass fraction profiles as well as the instantaneous thermochemical properties of the oscillating flame case were generally well reproduced. The inclusion of wall heat transfer was found to provide improved temperature and OH mass fraction results, particularly in the near-wall regions. A slightly under-predicted flame spreading angle and length - corresponding to faster combustion - were identified compared to the measurements. This was attributed to a somewhat overestimated degree of premixing potentially causing an increase in the burning rate. The disagreement in premixing degree and the failure to accurately capture the RMS scalar fluctuations towards the combustor centreline are most likely due to the flow solver’s incompressible formulation, which deliberately excluded any development of the experimentally observed flame oscillation caused by thermo-acoustic instabilities. Finally, comparisons between the LES and experiments were presented for the ‘stable’ flame case revealing very good agreement in terms of the overall flame shape and species concentrations including CO. Hence, the predictive capabilities of the employed *pdf* approach have been demonstrated in the context of partially premixed combustion.

Chapter 4

Combustion instabilities in the PRECCINSTA model combustor

In an attempt to reproduce the flame oscillation experimentally observed in the PRECCINSTA combustor, the fully compressible formulation of BOFFIN will now be applied. The simulation parameters described in the previous chapter (cf. Section 3.2.2) are preserved, except for the addition of a non-reflective outflow boundary condition with a target pressure of 1 bar to minimise acoustic wave reflection. No artificial forcing of the inlet velocities is imposed to ensure that any potential oscillatory behaviour observed in the simulation is fully self-excited. The specific objective of the work presented in this chapter is to capture and study the combined effects of self-excited thermo-acoustic and hydrodynamic instabilities. Despite considerable (mostly experimental) research efforts in the past, these effects are still not very well understood and typically examined separately, with the purpose of isolating the various feedback mechanisms at play. Relevant literature on the unstable PRECCINSTA test case is reviewed first, before presenting the results of the current study, which are organised into three parts concerning the discussion of thermo-acoustic instabilities (Section 4.2), hydrodynamic instabilities (Section 4.3) and the combined oscillation cycle (Section 4.4).

The contents of this chapter have been submitted for publication in Fredrich et al. (2020a,b).

4.1 Previous works

A significant number of experimental studies at various operating conditions have been carried out attempting to identify the underlying mechanisms involved in the observed flame oscillation. Among the different phenomena studied in these works are the role of mass flow rate and equivalence ratio oscillations, Meier et al. (2007); Stöhr et al. (2017), the dynamics of coherent vortex structures, i.e. the PVC, Boxx et al. (2012); Caux-Brisebois et al. (2014); Steinberg et al. (2013); Zhang et al. (2019) and symmetric vortex shedding, Steinberg et al. (2013), as well as the transition between bi-stable flame shapes, An et al. (2016); An and Steinberg (2019); Oberleithner et al. (2015); Stöhr et al. (2018); Yin et al. (2017).

4.1.1 Experimental findings

Meier et al. (2007) initially identified a fluctuating equivalence ratio of the local mixture convected into the combustion zone as the main driver of the observed thermo-acoustic feedback loop. The fluctuation was thought to be caused by different acoustic impedances of the fuel and air supply lines and subject to a convective time delay from the point of fuel injection. These findings were later verified by Stöhr et al. (2017) who further examined the interaction between velocity and equivalence ratio fluctuations based on a partially premixed as well as an additional perfectly premixed configuration. The emergence of a hydrodynamic instability in the PRECCINSTA test case was first reported by Boxx et al. (2012). Their investigation identified a helical PVC in the flow region around the inner shear layer (ISL) and the annular jet of reactants, which was found to precess the central burner axis with a frequency twice as large as that of the thermo-acoustic mode. In a parametric study of different perfectly premixed operating conditions, Steinberg et al. (2013) observed the periodic shedding of symmetric vortices at the thermo-acoustic frequency, which was replaced by a PVC with a higher frequency when decreasing Φ_{global} and increasing P_{th}.

A number of studies subsequently focused on the perfectly premixed combustor configuration looking into the interaction between the PVC and the flame dynamics. Caux-Brisebois et al. (2014) described qualitatively the mechanism of PVC deformation due to the propagation of swirl number waves with a characteristic phase lag. The resulting modulation of the flame ‘surface area’ was shown to be responsible for generating unsteady heat release. Oberleithner et al. (2015), An et al. (2016) and An and Steinberg (2019) investigated the role of the PVC in the transition from attached **V**-shape to lifted **M**-shape flames. They found the lift-off mechanism may be triggered by a stochastic local extinction event near the flame base altering the density gradient in the region. This promoted the formation of a PVC, which in turn increased the strain-rate at the flame base and eventually led to total flame detachment.

An and Steinberg (2019) also argued that future numerical simulations hence need to be able to reproduce flame extinction due to turbulent straining and hydrodynamic instability, in order to accurately predict the stabilisation process of swirl flame configurations. The influence of bi-stable flame shape transitions on the surface wall temperature at the combustor base plate and burner nozzle cone was further quantified by Yin et al. (2017). Stöhr et al. (2018) recently derived a detailed description of the governing mechanisms in a **V**- to **M**-shape flame transition and vice versa. Finally, Zhang et al. (2019) studied the coupling of PVC, IRZ and heat release at a partially premixed operating condition with elevated pressure and underlined how rapid mixing induced by a high frequency PVC can have a significant impact on the overall combustion dynamics.

4.1.2 Numerical findings

The majority of previous numerical studies have chosen the PRECCINSTA test case to validate specific LES combustion models (cf. Section 3.1.2) based on its reference operating condition, case (2a) with Φ_{global} = 0.83 and P_{th} = 30 kW, featuring a 'stable' flame, Meier et al. (2007). Only very few works in the published literature have attempted to investigate the experimentally observed oscillating flame behaviour and its underlying physical mechanisms, i.e. thermo-acoustic and hydrodynamic instabilities. Roux et al. (2005) computed both a non-reacting flow and a reacting flow involving a subtly pulsating flame, case (2b) at Φ_{global} = 0.75 and P_{th} = 27 kW, utilising a compressible LES method in combination with acoustic analysis. Comparisons with experimental data revealed good agreement for the predicted acoustic and hydrodynamic mode in the cold flow as well as for the thermo-acoustic mode obtained with combustion. A helical PVC was observed in the non-reacting case, however, its presence was reportedly damped under reacting conditions. Their study also underlined the importance of well-defined boundary conditions and resolving the upstream radial swirler instead of a solution domain inlet coincident with the combustion chamber inlet plane.

The oscillating flame case (1) measured by Meier et al. (2007) and considered in the current work, was first simulated by Franzelli et al. (2012). Their compressible LES successfully reproduced self-excited oscillations at a frequency of 390 Hz - about 100 Hz above the experimentally measured value. The overestimation was argued to be the result of an inaccurately modelled acoustic impedance at the fuel injection inlets. It was furthermore concluded that resolving the fuel-air mixing, as opposed to prescribing a fully premixed mixture at the domain inlet, is crucial for the prediction of thermo-acoustic coupling in this test case. Lourier et al. (2017) later performed a scale-adaptive simulation (SAS) of the oscillating flame case as well as additional experimental measurements with adjusted acoustic boundary conditions. For this purpose, a choked orifice plate 15 cm upstream of the air plenum was located inside the inflow nozzle creating a well-defined acoustic inlet boundary. This however, led to a marginal decrease of the predominant thermo-acoustic frequency by about 15 Hz. Moreover, rigid metal walls were securely mounted in between the combustion chamber corner posts to mitigate the effects of acoustic damping, which was evident in the initial measurement campaign by Meier et al. (2007) due to the use of loosely-mounted quartz glass windows. Power spectral density (PSD) analysis of the air plenum and combustion chamber pressure signals accordingly provided an increase in the oscillation amplitude of around 10 dB with the adjusted set-up. The employed SAS model switched between an LES and an unsteady Reynolds-averaged Navier-Stokes (URANS) solution depending on the local grid resolution and, based on the findings of Franzelli et al. (2012), both the fuel supply plenum and channels were included in the simulation. Good overall agreement was obtained for the thermo-acoustic frequency and its amplitude, showing only a relatively small over-prediction of about 15-25 Hz and 5 dB, respectively.

4.2 Thermo-acoustic instabilities

Results from the current LES of the PRECCINSTA combustor's thermo-acoustic behaviour are presented below. The predicted limit-cycle oscillation is described followed by a detailed description of its underlying driving mechanisms. In addition, time- and phase-averaged velocity, temperature and species mass fraction profiles are analysed and compared with the available experimental data. In order to initialise the flame, a cold flow solution was developed first. The fuel was then injected and ignited along the isothermal combustion chamber walls, i.e. by auto-ignition. The amplitude of the subsequent unsteady heat release and pressure oscillation grew continuously until a limit-cycle was reached after about 100 ms of physical time.

4.2.1 Limit-cycle oscillation

Figure 4.1 presents the fluctuation signals of the spatially integrated - or global - heat release rate (HRR) and the local pressure recorded at probes AP and CC (cf. Figure 3.1). The HRR and pressure inside the combustion chamber both visibly oscillate in phase indicating a positive feedback loop, therefore globally satisfying the Rayleigh (1877) criterion defined as:

$$\int_{\Omega}\int_{t_p} p'\dot{q}'d\Omega dt > 0 \tag{4.1}$$

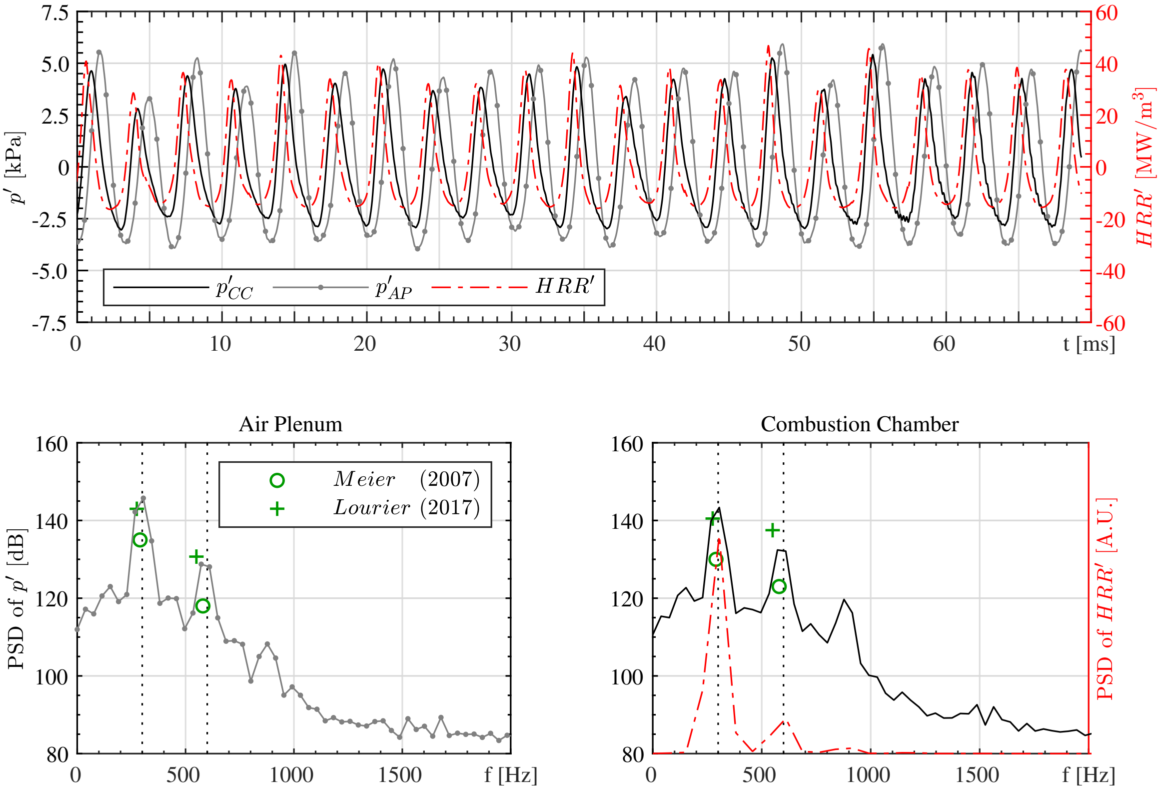

Figure 4.1: Top: Time signals of the global heat release rate and local pressure fluctuations recorded at AP and CC. Bottom: Their respective power spectral densities - where f denotes the frequency. PSD peaks from the experimental pressure signals are plotted for measurements with vibrating quartz windows Meier et al. (2007) and rigid metal walls Lourier et al. (2017).

where p' and $\dot{q}'$ are the local pressure and HRR and t_p is the oscillation period. Constant mean amplitudes further reveal a state of zero growth rate - typical of a limit-cycle oscillation. The existing modes are retrieved via PSD analysis showing two pronounced peaks in the air plenum and combustion chamber pressures, as well as in the global HRR. These peaks represent the dominant thermo-acoustic mode at 300 Hz and its first harmonic at 600 Hz, closely matching the experimentally measured counterparts of approximately 290 Hz and 580 Hz, Meier et al. (2007). The minor discrepancy of about 10 Hz may be related to a combination of small mismatches in the simulated test rig geometry (i.e. shorter inflow or exhaust pipe lengths), and the operating conditions, e.g. slightly higher air inflow temperatures increasing the local sound speed. Correct trends are also evident for the computed power densities. However, the peak amplitudes of 145 dB (290 Hz) and 128 dB (580 Hz) in the air plenum as well as 143 dB (290 Hz) and 133 dB (580 Hz) in the combustion chamber are each overestimated by about 10-13 dB when compared to the initial experiments by Meier et al. (2007). A similar observation was reported in a recent simulation by Lourier et al. (2017) who associated the over-prediction with acoustic damping incurred at the loosely-fitted quartz glass windows used in the experiments. Additional measurements performed with tightly-fitted rigid metal walls subsequently showed an increase of the peak pressure amplitudes by more than 10 dB, Lourier et al. (2017). This significant increase ultimately yields excellent agreement for the two dominant modes predicted in the current work, which are respectively within 2 dB and 5 dB of these additional measurements.

Overall, the LES method is shown to be capable of accurately reproducing the combustor's self-excited dynamic behaviour. A predominant limit-cycle oscillation is successfully captured at the correct frequency and amplitude despite the fuel plenum and supply lines not being included in the solution domain. These results further underline the importance of utilising appropriate boundary conditions in test cases involving thermo-acoustic phenomena. Care must be taken specifically, when dealing with potential damping effects arising from vibrating structural parts or perforated cooling liners often installed in industrial applications.

4.2.2 Governing feedback loop

One full period of the global HRR, pressure and mass flow rate oscillations is presented in Figure 4.2, including the introduction of eight, equally spaced phase angles ($Ph_{1\text{-}8}$) used for phase-averaged and -resolved analyses throughout the rest of this work. The observed initial steep rise in heat release is expected to produce a pressure disturbance at the flame front that propagates up- and downstream within the domain. The local pressure, recorded by probes located in the combustion chamber and air plenum, increases accordingly with a specific time delay governed by the propagation speed of the acoustic wave. This time delay introduces a

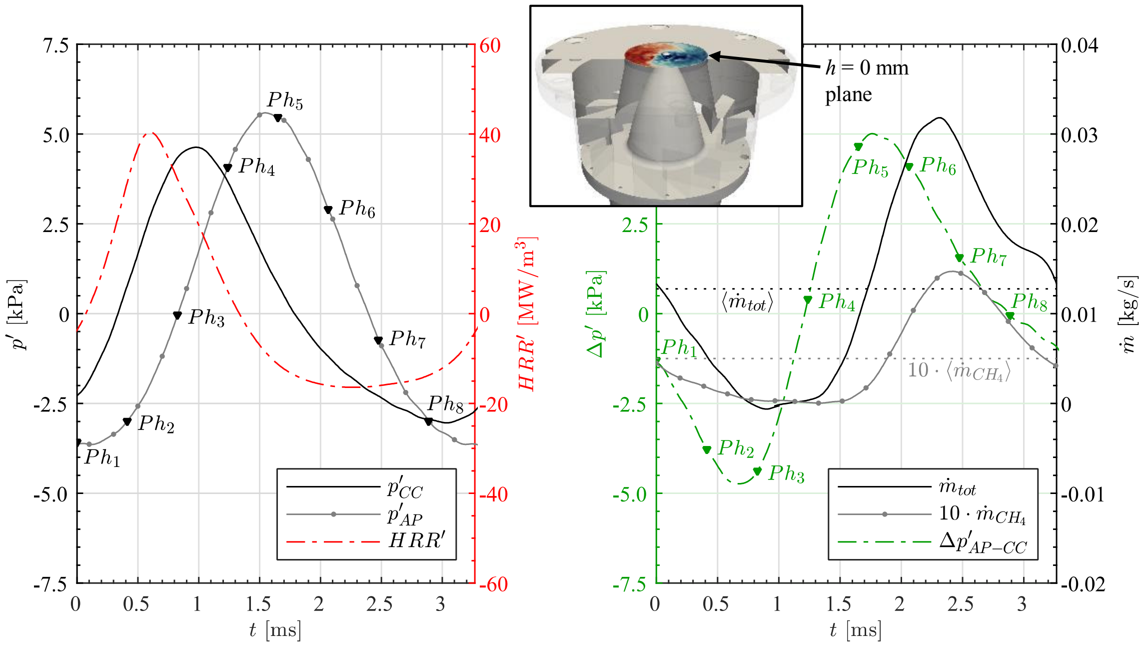

Figure 4.2: Left: Temporal evolution of the global heat release rate and local pressure fluctuations at AP and CC for a full period of the oscillation cycle. Eight different phase angles are introduced: $Ph_1 = 0°$, $Ph_2 = 45°$, $Ph_3 = 90°$, $Ph_4 = 135°$, $Ph_5 = 180°$, $Ph_6 = 225°$, $Ph_7 = 270°$, $Ph_8 = 315°$. Right: Pressure drop between AP and CC as well as the resulting fluctuations of $\dot{m}_{CH_4}$ (scaled by a factor of 10) and $\dot{m}_{tot}$ in the burner nozzle exit plane ($h =$ 0 mm). The respective time-averages are denoted as $\langle \cdot \rangle$.

phase shift between both signals with a maximum phase difference of about 80°, similar to experimental findings reported in Meier et al. (2007). The resulting pressure drop between the combustion chamber and air plenum fluctuates periodically inducing total mixture and CH_4 mass flow rate oscillations, $\dot{m}_{tot}$ and $\dot{m}_{CH_4}$, inside the swirler and burner nozzle. These oscillations - evaluated in the burner nozzle exit plane (h = 0 mm) - lead to a fluctuating supply of unburnt reactants into the main flame zone, which in turn induces the unsteady heat release response. A minor phase lag between the two mass flow rates becomes evident and represents the temporal variation of the local mixture equivalence ratio. This phase lag is caused by an additional mechanism involving fuel accumulation inside the swirler unit combined with a convective time delay further discussed below.

The spatial and temporal evolution of the flow oscillation is shown in Figure 4.3 for a full period of the thermo-acoustic cycle. Starting from Ph_1, an increased mass flow rate of fresh reactants with elevated local equivalence ratio enters the combustion chamber - as characterised by the high velocity magnitudes and fuel concentration in this region. Large quantities of premixed fuel and oxidiser are thereby transported into the main flame zone enhancing combustion. The global HRR reaches its maximum value around Ph_2, successively elevating the pressure inside the combustion chamber. Consequently, the pressure drop between the combustion chamber and air plenum becomes negative, decreasing the mass flow and hence supply of fresh reactants into the combustion zone. At Ph_3, the bulk flow inside the swirler unit becomes almost stagnant, whereas the fuel injection rate remains essentially constant. This is a result of the high acoustic impedance of the fuel jets, making them only weakly susceptible to incident pressure disturbances. A significant amount of fuel accumulates within the swirler unit during $Ph_{4\text{-}5}$, raising the equivalence ratio of the local mixture. Scattered occurrences of flame flashback can be observed as the IRZ moves further upstream, extending the reverse flow far into the burner nozzle (also visible in Figure 4.10). Based on the lack of fresh reactants located within the combustion zone, the heat release rapidly decreases followed by a reduction of the local pressure. The pressure drop between the combustion chamber and air plenum is subsequently reversed and becomes positive. From Ph_6, the mass flow rate within the swirler begins to increase again as the global HRR in the combustion chamber approaches a minimum. The accumulated high-equivalence-ratio mixture exits the burner nozzle with high momentum around Ph_7. Additionally, the flame base begins to lift-off from the burner nozzle cone and outer rim while the flame front is convected downstream. Similar lift-off events have previously been reported in the literature, e.g. Prasad et al. (2014) who investigated the propagation of lifted flames after a controlled mass flow pulse of fuel. The feedback loop is finally closed at Ph_8 as the heat release begins to increase again.

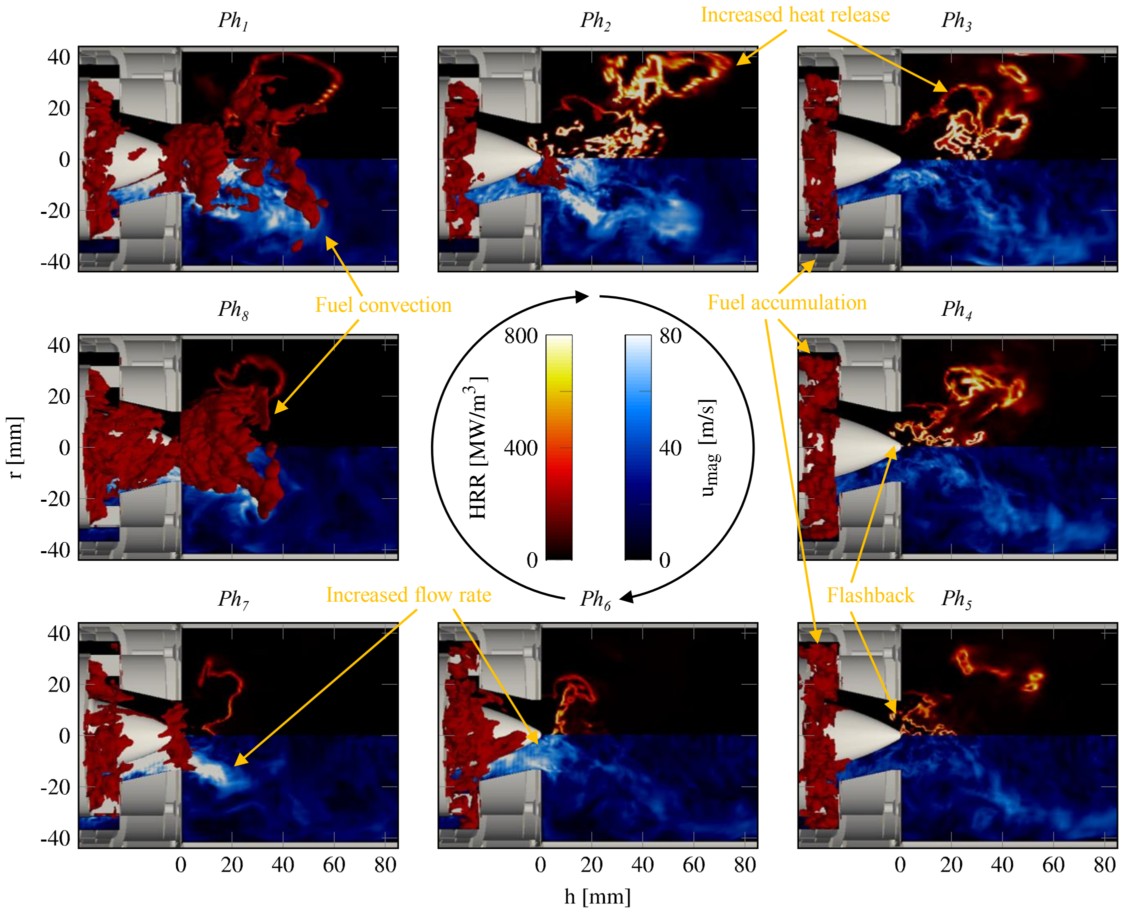

Figure 4.3: Periodic evolution of the local heat release rate, velocity magnitude and reactant mixture composition. Red iso-surfaces of a constant CH_4 mass fraction equal to 0.035 delineate the instantaneous fuel distribution.

In summary, a superposition of mass flow rate and reactant mixture composition (i.e. local equivalence ratio) oscillations, can be identified as a key driving mechanism underlying the governing feedback loop. These oscillations are sustained by a periodically varying pressure drop between the combustion chamber and air plenum due to acoustic wave propagation. A similar oscillation behaviour, involving violent, periodic flame lift-off and flashback in accordance with the current LES, was recently reported by Temme et al. (2014). Their experimental study of a swirl-stabilised, liquid fuel gas turbine combustor featured strong self-excited combustion instabilities driven by a comparable equivalence ratio oscillation mechanism. While the potential impact of hydrodynamic phenomena was not explicitly investigated, results did underline the importance of flame lift-off in these types of instabilities.

4.2.3 Phase-averaged statistics

Time- and phase-averaged radial profiles of the velocity, temperature and species mass fractions are shown in figures 4.4, 4.5 and 4.6, respectively, for five different downstream locations. These statistics have been collected for a duration of 130 ms of physical time - equivalent to about 40 oscillation cycles - and are compared with measurement data from the first experiments by Meier et al. (2007). As mentioned previously, these experiments were influenced by acoustic damping effects in the combustion chamber, which are neglected in the current simulation. The computed flame oscillation is therefore expected to be amplified as a result of the increased limit-cycle amplitude. Unfortunately, similar detailed measurement data from the latter campaign of Lourier et al. (2017) is not available since the utilised rigid metal walls provided no optical access for laser-based measurements. Nevertheless, both the axial and radial velocity profiles shown in Figure 4.4 are in good agreement with the measurements and accurately reproduce the flow's oscillating behaviour. This includes reproducing the varying location and strength of the IRZ, ORZ and incoming annular jet of fresh reactants, represented by two pronounced velocity maxima. Globally, these maxima display a minor inwards shift with downstream position, which, in combination with underestimated peak values in the radial velocity, indicate a smaller spreading angle. The jet's expansion into the combustion chamber is furthermore slightly over- and under-predicted between $Ph_{8\text{-}2}$ and $Ph_{4\text{-}6}$, respectively, exemplifying the amplified oscillation amplitude.

Figure 4.5 illustrates the corresponding flame oscillation, which is characterised by an alternating down- ($Ph_{8\text{-}2}$) and upstream ($Ph_{4\text{-}6}$) movement of the flame front. The overall flame position and shape are qualitatively captured, while the temperature distribution in the ORZ is reproduced, suggesting the applied wall heat transfer treatment is realistic. Within the IRZ, the flame lift-off height is almost universally over-predicted, implying a longer duration of flame detachment, Hermeth et al. (2014) from the burner nozzle cone compared

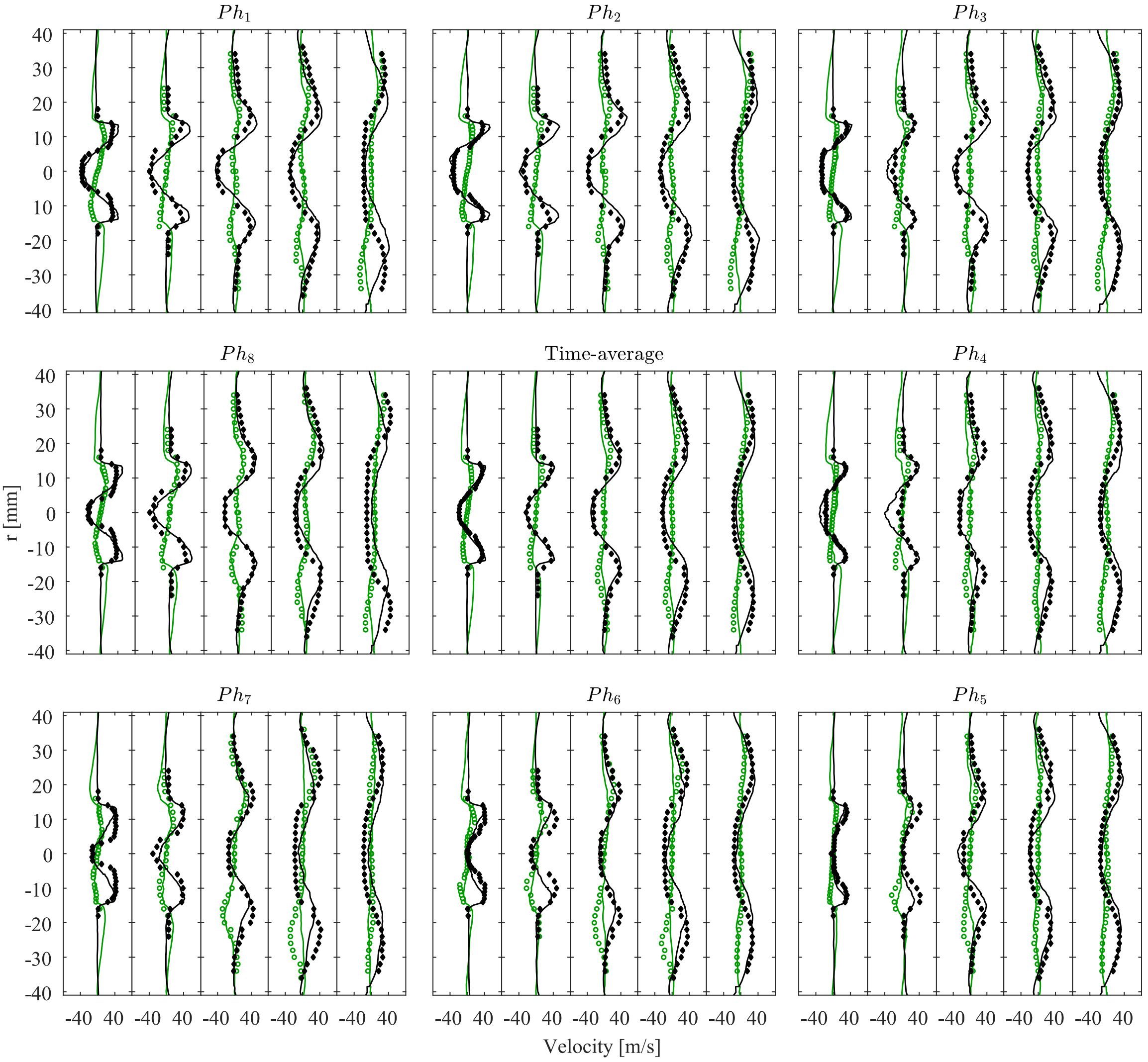

Figure 4.4: Phase-averaged radial profiles of the axial (black) and radial (green) velocity at downstream positions *h* = 1.5, 5, 15, 25, 35 mm - lines: simulation; symbols: experiment. The corresponding time-averaged results are shown in the centre.

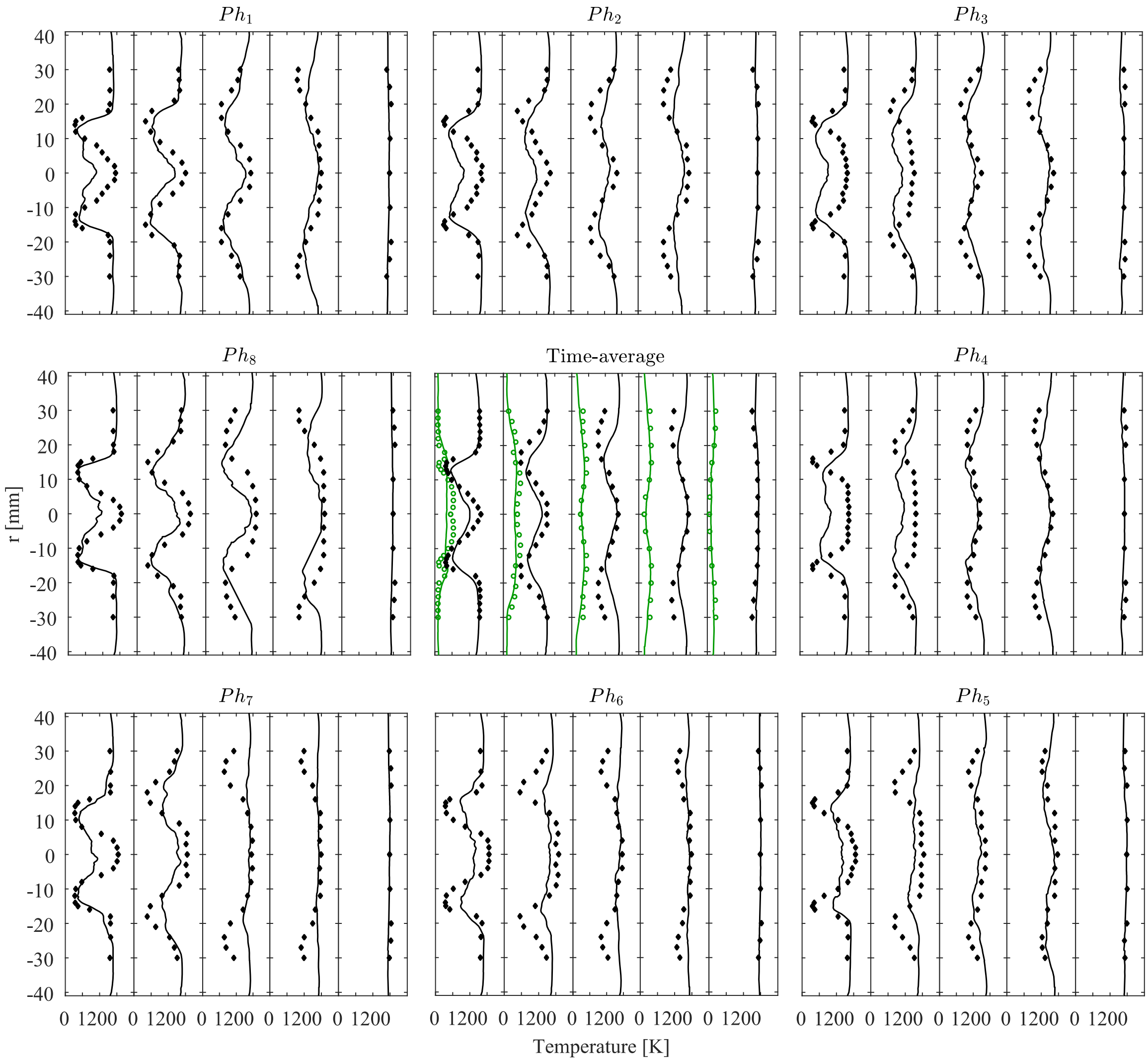

Figure 4.5: Phase-averaged radial profiles of the mean (black) and RMS (green) temperature at downstream positions h = 6, 15, 25, 35, 60 mm - lines: simulation; symbols: experiment. The corresponding time-averaged results are shown in the centre.

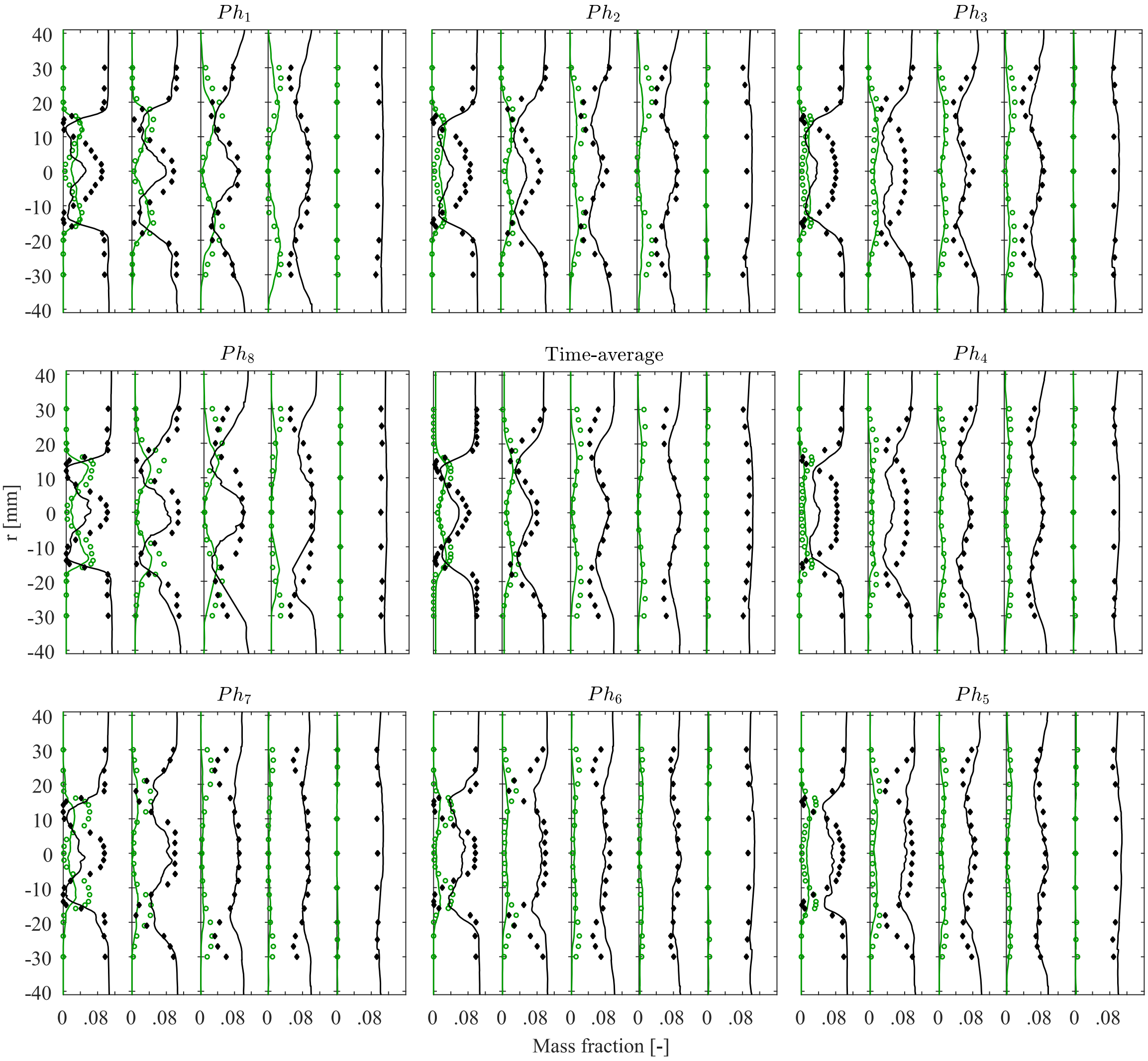

Figure 4.6: Phase-averaged radial profiles of the CO_2 (black) and CH_4 (green) mass fraction at downstream positions h = 6, 15, 25, 35, 60 mm - lines: simulation; symbols: experiment. The corresponding time-averaged results are shown in the centre.

to the measurements. In accordance with the obtained velocity field, an underestimation of the flame's global spreading angle can be determined from the time-averaged temperature profiles in the centre of Figure 4.5. Moreover, global temperature fluctuations of up to 500 K - indicated by the RMS profiles - are expectedly high in both the simulation and experiments due to the oscillating nature of the flame. However, while the computed results show an almost constant level of fluctuation inside of the ISL ($|r| \leqslant 16$ mm), experimental data reveals an additional dip of RMS values in between the inner and outer shear layer ($10 \leqslant |r| \leqslant 16$ mm) not captured by the LES. The simulated radial location of the inner and outer flame front is therefore presumably less steady over the thermo-acoustic cycle. This conclusion is further supported by radial fluctuations of the ISL and OSL that are displayed in Figure 4.4 and accompanied by a widening and narrowing of the IRZ. A distinct oscillation of the flame angle with respect to the axial direction - also known as flame flapping - can be inferred, which is likely to contribute to the under-predicted global spreading angle observed in the annular jet and flame. The increased flapping motion is potentially induced by swirl number fluctuations, Candel et al. (2014); Palies et al. (2010) associated with stronger acoustic perturbations. These may again be attributed to a higher amplitude limit-cycle oscillation in the simulations. A more detailed description of the resulting flame angle oscillation is provided in Section 4.3.1 below.

Finally, radial profiles of the CO_2 and CH_4 mass fraction are shown in Figure 4.6 to complement the velocity and temperature results. Although the overall trends between the different scalars are consistent, the deviations from the measurements are of larger magnitude compared to those of the velocity profiles. This is probably related to the large gradients, for example in temperature, that occur across a thin flame front. Minor spatial differences in flame location - manifested by small velocity deviations - will naturally result in more pronounced deviations in the composition and temperature profiles.

4.3 Hydrodynamic instabilities

In the following subsections, the flow is further examined for hydrodynamic instabilities resulting from flame angle oscillation or flame-vortex interaction. The formation of large-scale vortical structures and their potential impact on the local heat release and mixing of fuel and oxidiser are also described.

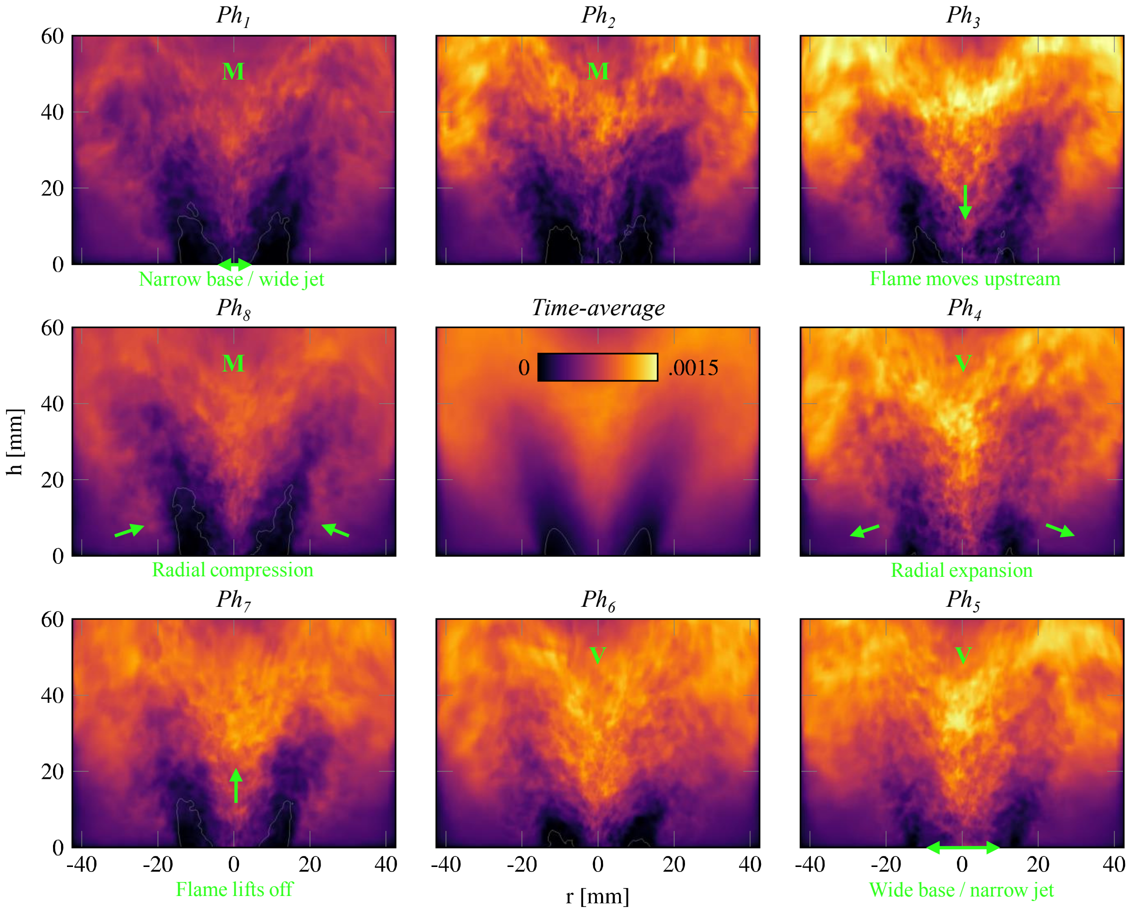

Figure 4.7: Phase-averaged snapshots of the OH concentration with arrows qualitatively indicating the periodic evolution of the flame motion, spreading angle and overall topology (i.e. **V**-shape or **M**-shape). White iso-contours of a constant CH_4 mass fraction equal to 0.025 indicate the extension of the incoming annular jet.

4.3.1 Flame angle oscillation

Phase-averaged snapshots of the OH concentration are displayed in Figure 4.7. The flame visibly lifts off from the burner nozzle cone between $Ph_{7\text{-}8}$ and reattaches about half of a period later at $Ph_{3\text{-}4}$. Within each cycle, the overall flame topology transitions from an attached **V**-shape ($Ph_{4\text{-}6}$) to a lifted **M**-shape ($Ph_{8\text{-}2}$) and vice versa. This flame shape transition can be compared to the one observed experimentally by Oberleithner et al. (2015) and Stöhr et al. (2018) for a slightly different operating condition with reduced thermal power (P_{th} = 20 kW). In these experimental studies however, the transition was not periodic and instead involved a bi-stable flame undergoing bifurcation with significantly longer time scales (about once per second). A radial compression and expansion of the flame spreading angle can furthermore be identified and comes with a widening and narrowing of the flame base (and annular jet, cf. Figure 4.4), which was also reported in recent experiments by Stöhr et al. (2017). The maximum and minimum flame angle are observed around Ph_1 and Ph_5, respectively.

The obtained flame angle oscillation is caused by an unsteady interaction between the swirler unit and incident acoustic perturbations, which originate from the fluctuating pressure drop between the air plenum and combustion chamber. Under low-Mach number flow conditions, pressure waves that impinge on a swirler unit are subject to a mode conversion process giving rise to both axial and azimuthal velocity perturbations, Palies et al. (2011a). The former are propagated downstream (at the sound speed) in the form of axial acoustic waves. They may induce a shedding of toroidal vortices from the burner nozzle rim (cf. Section 4.3.2), which in turn can roll up the flame front. The latter are caused by acoustic vorticity waves generated at the trailing edge of the swirler blades, Cumpsty and Marble (1977); Komarek and Polifke (2010); Sajben and Said (2001); Wang and Yang (2005) and have an amplitude of the same order of magnitude as the incident acoustic disturbance, Palies et al. (2011a). These acoustic vorticity waves are believed to be convected downstream by the bulk flow - hence introducing a phase shift - and effectively perturb the swirl number, which controls the motion and strength of the IRZ, Palies et al. (2010, 2011b). The resulting angular oscillation of the flame root may then lead to fluctuations of the turbulent burning velocity, thereby promoting an unsteady heat release response, Palies et al. (2017). Note that the exact mechanisms underlying the mode conversion process are still not very well understood and remain a major focus of ongoing research efforts.

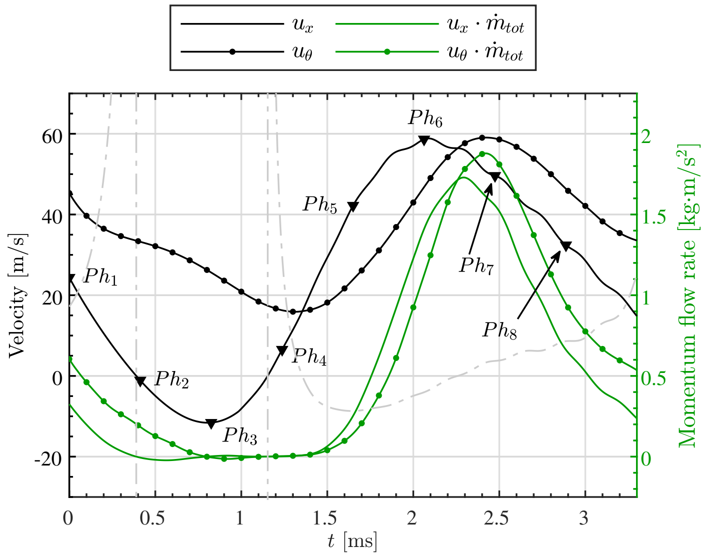

Figure 4.8: Temporal evolution of the axial and azimuthal components of the velocity (u_x, u_θ) and momentum flow rate, spatially integrated over the burner nozzle exit plane (h = 0 mm) for a full period of the oscillation cycle. A dash-dotted line indicates the ratio of azimuthal to axial momentum flow rate (scaled by a factor of 2).

The swirl number S, Beér and Chigier (1983) essentially compares the axial flux of azimuthal momentum with the axial flux of axial momentum:

$$S = \frac{\int_0^{R_n} u_x u_\theta r^2 dr}{R_n \int_0^{R_n} u_x^2 r dr} \tag{4.2}$$

where R_n is the burner nozzle equivalent radius while u_x and u_θ represent the axial and azimuthal velocity components. The afore-mentioned swirl number fluctuations $S'/\hat{S}$ can be deduced from the ratio of the azimuthal and axial momentum flow rates, spatially integrated over the burner nozzle exit plane and shown in Figure 4.8. Other hydrodynamic phenomena such as a PVC or periodic vortex shedding have also been linked to the swirl-induced axial and azimuthal momentum in the past. These can have a significant impact on the local heat release, viz. by directly modulating the flame's 'surface area' or enhancing the mixing of fuel and oxidiser. The potential formation of coherent vortical structures is therefore investigated below.

4.3.2 Large-scale vortical structures

Local low pressure iso-surfaces are utilised to visualise the excitation and suppression of large-scale vortices (Poinsot and Veynante, 2005) inside the combustion chamber as shown

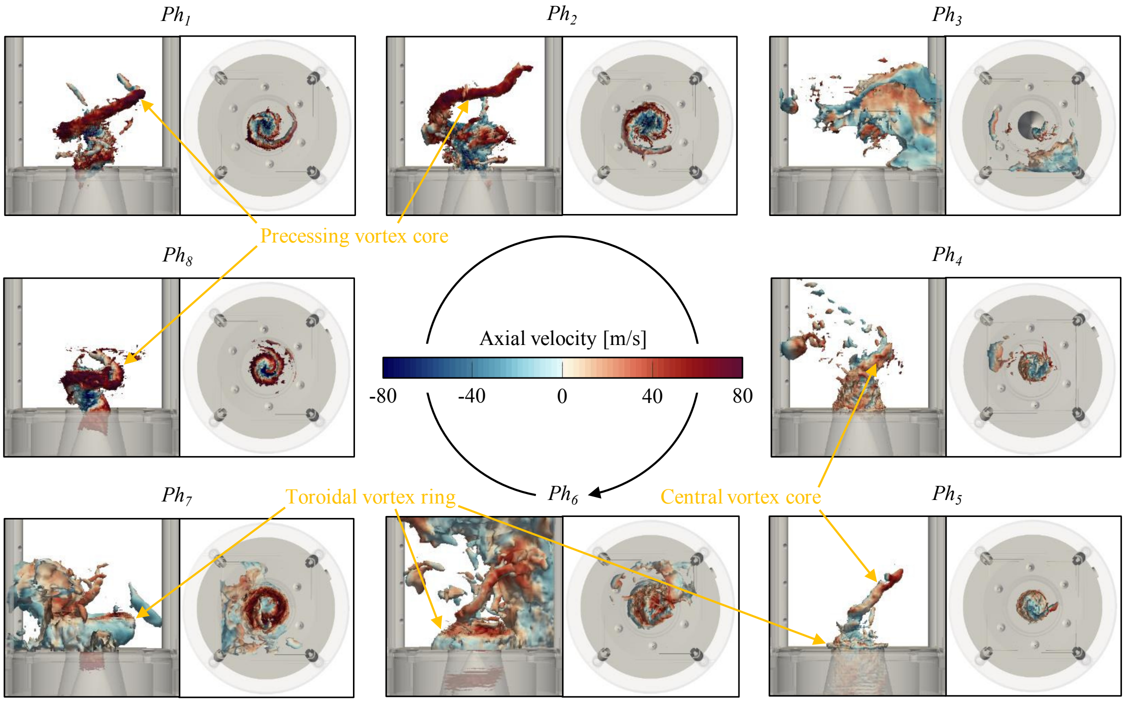

Figure 4.9: Periodic formation and suppression of large-scale coherent vortex structures inside the combustion chamber (top and side view) visualised by local low pressure iso-surfaces and coloured by axial velocity.

in Figure 4.9. At Ph_3, the axial and azimuthal momentum flow rate entering the combustion chamber reaches its minimum (cf. Figure 4.8) and no distinct hydrodynamic structure can be detected in the region of interest. A central vortex core (CVC) is observed throughout the rest of the oscillation cycle ($Ph_{4\text{-}2}$) sustained by the azimuthal momentum induced in the swirler unit. The steadily increasing axial momentum from Ph_5 leads to the development of a vortex ring adjacent to the outer rim of the burner nozzle. This vortex ring continues to gain in size until it is eventually shed from the rim after Ph_6 and convected downstream in the shape of a toroid. Between $Ph_{8\text{-}2}$, a helical PVC structure is excited by the rapidly increasing azimuthal velocity generated from the vorticity wave exiting the burner nozzle. The ratio between azimuthal and axial momentum flow rate is largest at this point and may be related to a high instantaneous swirl number (cf. Eq. (4.2)). The PVC performs an almost 180° rotation while increasing its axial and radial extension into the combustion chamber until it finally breaks down and vanishes before Ph_3. This periodic loop of hydrodynamic interactions is repeated in each oscillation cycle showing its strong coupling with the predominant thermo-acoustic mode.

Prior to the present work, Steinberg et al. (2013) experimentally detected a PVC and symmetric vortex shedding in a parametric study of the PRECCINSTA combustor. Both phenomena however, did not co-exist at identical combustor operating conditions. The symmetric shedding of toroidal vortices was obtained at lower thermal powers, whereas higher thermal powers led to the formation of the PVC. In the current work, periods of reduced heat release during the oscillation cycle ($Ph_{5\text{-}8}$; cf. Figure 4.2) can be associated with lower thermal powers promoting vortex shedding. As the global HRR increases ($Ph_{8\text{-}2}$) - corresponding to an operating condition with higher thermal power - the PVC is excited instead. A higher limit-cycle amplitude compared to the experiments conducted with the loosely-fitted quartz glass combustion chamber walls further contributes to this effect by enhancing the fluctuation intensity. The simultaneous existence of both phenomena at the same operating condition can thereby be explained.

4.3.3 PVC and toroidal vortex shedding

Swirl-induced vortex breakdown is typically used to ensure flame stabilisation by creating an inner and outer recirculation zone, Lucca-Negro and O’Doherty (2001) responsible for transporting hot combustion products back to the flame front. In some cases, this vortex breakdown can become asymmetric leading to a displacement of the IRZ and precession of the vortex core around the central burner axis. The resulting helical flow motion is usually referred to as a PVC and its existence has been confirmed for a number of swirl-stabilised combustor configurations, see e.g. Syred (2006). Although various numerical works have

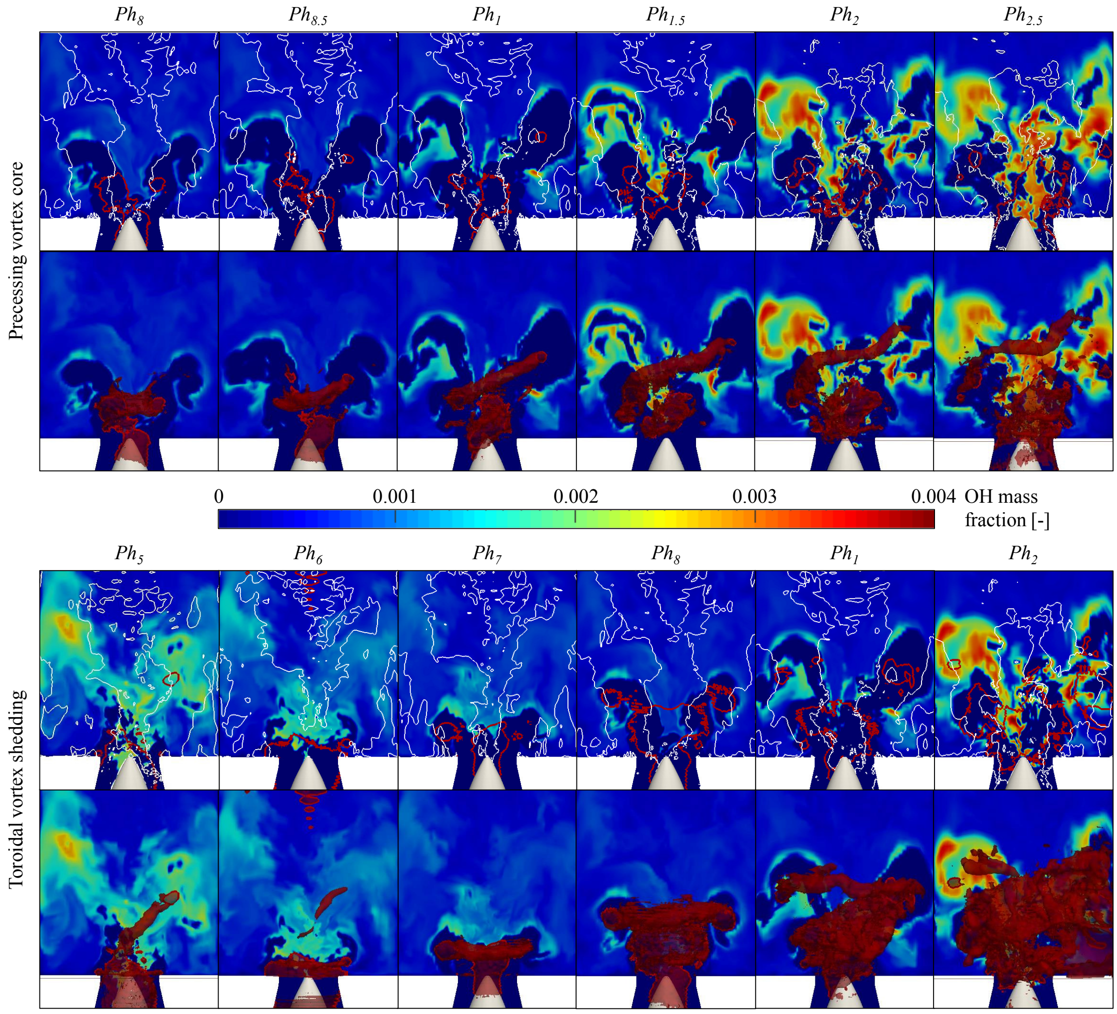

Figure 4.10: Periodic evolution of the PVC (top) and toroidal vortex shedding (bottom) and their respective interaction with the flame front - visualised by OH concentration. Red iso-contours delineate the vortical structures via low isobaric values whereas white iso-contours indicate the zero velocity line.

detected vortex core precession in isothermal flow cases, e.g. Bulat et al. (2015b); Roux et al. (2005); Selle et al. (2004), it is often reportedly damped once combustion is activated. Hence, only very few simulations have successfully identified a PVC under reacting flow conditions: Chen et al. (2019a); Duwig and Fuchs (2007); Hermeth et al. (2014); Wang et al. (2007).

Figure 4.10 shows the periodic evolution of the PVC and its interaction with the flame front in the present case. The flame generally stabilises in between the ISL and OSL, except for instances when it is locally displaced by the PVC (visible at Ph_2), consequently generating asymmetric combustion. The PVC itself is situated along the zero velocity line, as expected, separating the annular jet of reactants and the IRZ (Syred, 2006) while causing a characteristic deformation of the latter. It becomes clear that the vortex core precession coincides with flame detachment and lift-off from the burner nozzle cone as previously observed, e.g. by Hermeth et al. (2014); Karlis et al. (2019a); Terhaar et al. (2015). The PVC appears to play a role in this detachment mechanism by increasing the fluid strain rate leading to local flame extinction, An and Steinberg (2019). The resulting region of unburnt, low viscosity gases with a fairly uniform density distribution serves as a favourable environment for PVC formation. Schönborn et al. (2014) have recently suggested that flame eccentricity caused by vortex core precession can be detrimental to upstream flame propagation and thus effective in inhibiting flame flashback. However, as a result of the increasing reverse flow from Ph_2, the inner flame front eventually surges back upstream towards the burner nozzle cone. Enhanced fuel-air mixing induced by the PVC possibly accelerates this process by promoting upstream flame propagation in the region, Ahmed and Birouk (2018). The PVC base is incidentally 'blown off' the burner nozzle cone and pushed outward allowing the inner flame front to reattach. This in turn generates strong radial density/temperature gradients, which have proven to be critical in suppressing vortex core precession, Oberleithner et al. (2015). The entire PVC structure ultimately vanishes after $Ph_{2.5}$ as the flame begins to flash back into the burner nozzle.

A description of the periodic vortex shedding mechanism is carried out based on the lower half of Figure 4.10. As mentioned above, from Ph_5 a low pressure ring vortex develops on the outer rim of the burner nozzle due to flow separation stemming from an increased mass flow rate entering the combustion chamber. This ring vortex consistently grows in size and appears to assist local quenching of the flame base around the OSL, which eventually leads to complete flame detachment from the outer rim. The ring structure itself is shed between $Ph_{6\text{-}7}$, forming a toroidal vortex that is convected downstream along the OSL at the bulk flow velocity. It continues to grow under the influence of vortex stretching, exothermicity and volumetric expansion (Fureby, 2000) while interacting with the flame's reaction layers.

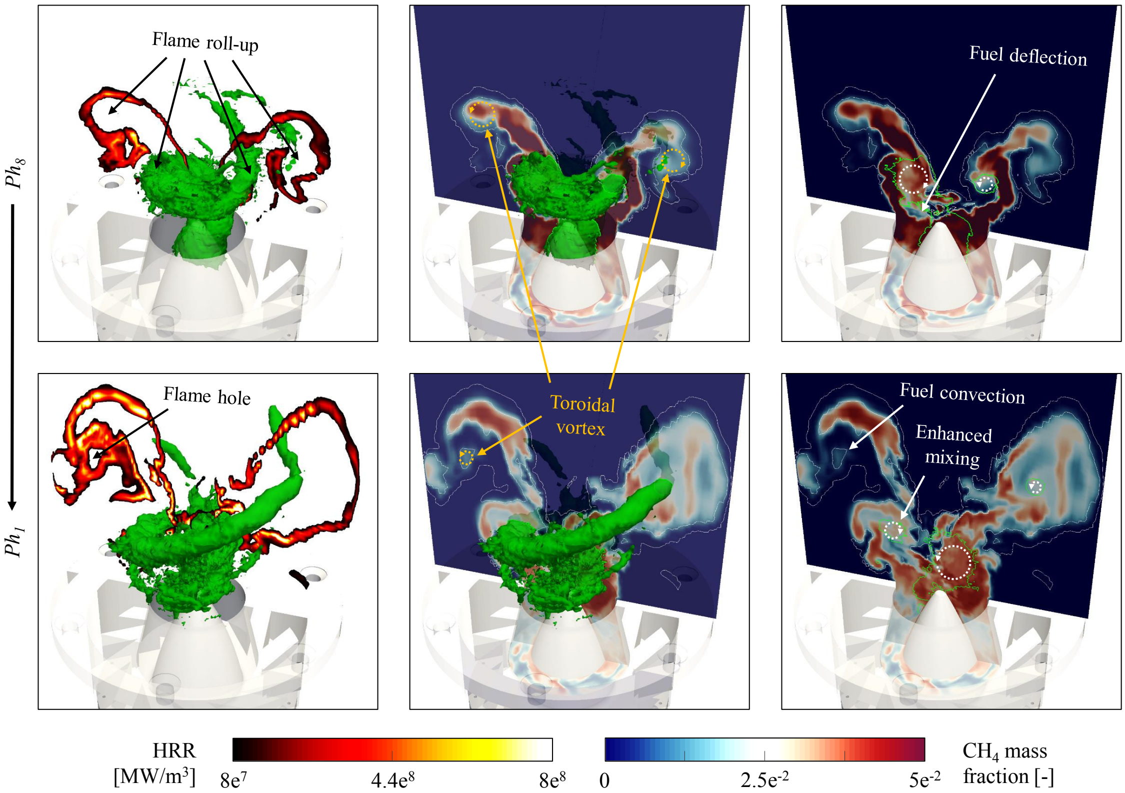

Figure 4.11: Typical instantaneous interaction of the PVC and toroidal vortex with the flame front and the incoming annular jet at Ph_8 (top) and Ph_1 (bottom). Green iso-contours delineate the vortical structures via low isobaric values. White iso-contours indicate a constant local heat release rate of 80 MW/m^3 corresponding to about 5% of its maximum value during this period of the oscillation cycle.

At Ph_1, the toroidal vortex collides with the helical PVC structure resulting in its partial destruction before it eventually breaks down and dissipates after Ph_2.

A more detailed representation of the typical instantaneous interaction between the flame, flow and large-scale vortices is provided in Figure 4.11. The PVC and toroidal vortex both visibly roll up the flame front, thereby directly modulating its overall ‘surface area’ and generating unsteady heat release in an asymmetric or axisymmetric manner, respectively. However, Balachandran et al. (2005) have shown that vortices induced by inlet velocity fluctuations may not only generate ‘surface area’ when the flame front wraps around them, but can also lead to its destruction through flame annihilation events. A distinct hole in the flame sheet is created by the toroidal vortex enclosing unburnt reactants within its core. These trapped reactants are convected downstream and consumed after a time delay governed by the vortex break-up time. Steinberg et al. (2011) investigated the re-ignition of flame holes due to edge-flame propagation around the perimeter of such vortical structures, indicating well-mixed pockets of fuel and oxidiser. A rapid growth in heat release once these pockets of trapped reactants are consumed by flame fronts converging towards their centres was reported by Ghoniem et al. (2005). Flame-wall interaction in the present case appears to form additional reactant pockets that are entrained between the flame front and combustion chamber side walls and therefore also subject to delayed consumption. The PVC may further influence combustion by enhancing the local mixing of fuel and oxidiser, Froud et al. (1995) and, due to its positioning along the ISL, supplying heat and radicals from the recirculating burnt gases to the incoming stream of unburnt reactants, Stöhr et al. (2011). The incoming stream is moreover radially deflected by the PVC (Steinberg et al., 2010) in proximity of the burner nozzle resulting in asymmetric heat release downstream. This deflection can assist upstream flame propagation by reducing the flame-normal approach speed of the incoming annular jet, Ranjan et al. (2019).

4.4 Combined oscillation cycle

Finally, the interaction and coupling between the different instability mechanisms is examined yielding a comprehensive description of the combined oscillation cycle. In a simple analysis investigating vortex shedding without swirl, Venkataraman et al. (1999) have revealed that heat release oscillations are associated with both flame ‘area’ and equivalence ratio fluctuations. This finding has since also been confirmed for configurations involving swirling flames, see e.g. a recent LES study by Tachibana et al. (2015). In order to quantify these two parameters, the instantaneous flame ‘sheet’ is extracted in the current work by introducing a local HRR threshold of 1.5×10^8 W/m^3. This value corresponds to about 5% of the

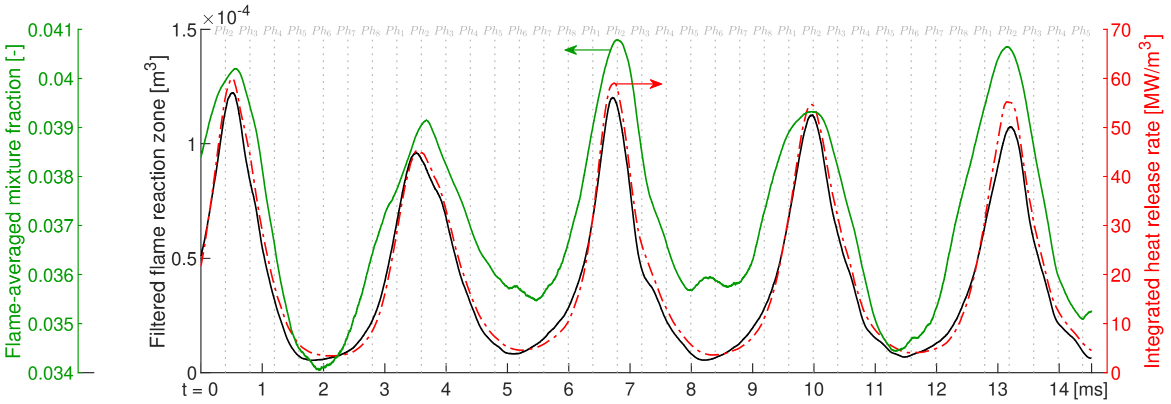

Figure 4.12: Time signals of the filtered flame reaction zone (spatially integrated using a threshold of 150 MW/m^3 on the local heat release rate), flame-averaged mixture fraction and global heat release rate.

maximum generated at any point in the chamber over the entire oscillation period. An approximation to the flame's 'surface area' is then obtained from the three-dimensional volume in which this threshold is exceeded - the filtered flame reaction zone volume. The mixture fraction can then be spatially integrated over this reaction zone volume leading to a measure of the flame-averaged mixture fraction (or equivalence ratio).

Figure 4.12 shows both the flame 'surface area' and flame-averaged mixture fraction quantified over multiple oscillation cycles alongside the global HRR. The corresponding periodic evolution of the instantaneous flame topology is displayed in Figure 4.13, based on iso-surfaces of the HRR coloured by mixture fraction. All three quantities shown in Figure 4.12 visibly fluctuate in phase, indicating that the heat release oscillation is indeed controlled by variations of both the reaction rate per unit flame 'area' and the flame 'surface area' itself. The former are modulated by the equivalence ratio oscillation mechanism resulting from periodic fuel accumulation in the swirler unit. The latter can be related to the periodic generation and destruction of flame 'surface' due to large-scale elongation and corrugation of the flame front, ignition of unburnt reactants, and local flame extinction, Caux-Brisebois et al. (2014). In the present work, these phenomena arise from hydrodynamic flame-flow-vortex interactions as well as the observed total mixture mass flow rate oscillation, and appear to have a larger effect on the HRR fluctuations compared to variations in the reaction rate per unit flame 'area'. Wrinkling of the reaction layers introduced by small-scale turbulence is an additional factor weighing into potential perturbations of the flame's 'surface area', though this may not be directly correlated with the prevailing limit-cycle oscillation. Random turbulent events can however act as an initial trigger mechanism for self-excited combustion instabilities.

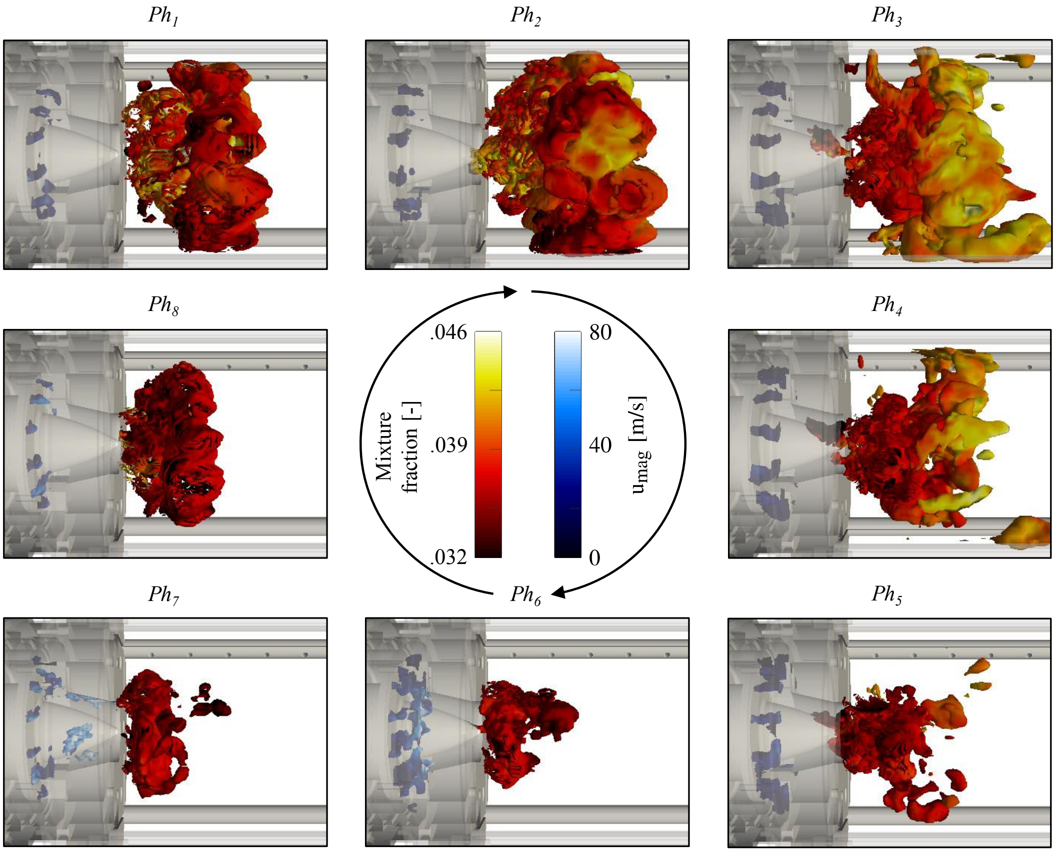

Figure 4.13: Periodic evolution of the instantaneous flame topology and fuel injection represented by iso-surfaces of a constant local heat release rate of 150 MW/m^3 and CH_4 mass fraction of 0.1, respectively. The former is coloured by mixture fraction, the latter by velocity magnitude.

Prior studies have also suggested that helical PVC structures conventionally do not contribute to fluctuations of the global HRR, implying that any local influence cannot be detected in the spatially integrated signal. This is related to their non-axisymmetric azimuthal mode shape - i.e. $m \neq 0$, when expressed as a flow disturbance in normal form, see e.g. Monkewitz (1988), using cylindrical coordinates:

$$\Upsilon'(x,r,\theta,t) = \sum_{m=0}^{\infty} \check{\Upsilon}_m(r)\exp[i(kx+m\theta-\omega t)] \tag{4.3}$$

where Υ' represents any disturbance quantity, $\check{\Upsilon}_m$ is the azimuthal disturbance amplitude, k and m are the axial and azimuthal wave number, respectively, and ω is the frequency of the disturbance. In this formulation, the PVC corresponds to a helical mode of $m = 1$, and thus exerts a non-axisymmetric modulation of the flame 'surface area'. The associated fluctuations in local heat release must therefore be strongly asymmetric and have previously been shown to cancel out in space over the oscillation period, Acharya et al. (2013); Moeck et al. (2012). However, such a spatial cancellation can only occur for a consistently active disturbance that constantly rotates about the central burner axis. In the current case, the PVC is periodically excited and suppressed, resulting in a phase-specific influence on the global HRR. The toroidal vortex, on the other hand, represents an axisymmetric mode ($m = 0$). It therefore modulates the local heat release in an axisymmetric manner through flame quenching and roll-up, causing fluctuations of the global HRR at the vortex shedding frequency. Hence, the successive formation of toroidal vortices and helical PVCs induces flame 'surface' disturbances with an $m = 0$ to $m = 1$ mode shape transition. Due to their favourable timing within the oscillation cycle, both hydrodynamic phenomena amplify the global instability by increasing heat release in phase with the dominant thermo-acoustic mechanism, thereby feeding acoustic energy into the system.

The overall sequence of periodic amplification and attenuation can be summarised as follows: Ph_4 - the global HRR, flame 'surface area' and flame-averaged mixture fraction all decrease rapidly; Ph_5 - the flame approaches its minimum spreading angle, consequently reducing the reaction rate per unit flame 'area'; the developing vortex ring leads to additional flame 'surface' destruction by quenching the outer flame base; Ph_6 - the growing mass flow rate of incoming reactants enhances combustion and elongates the flame front; the combination of low flame-averaged mixture fraction and increased stretch rates from higher velocities provokes partial extinction of the flame base, Ju et al. (1997); Ph_7 - the subsequent rise in local mixture equivalence ratio reaches the flame front elevating its reaction rate; the shed toroidal vortex gains in size and strength as it is convected downstream generating flame 'surface' by rolling up the flame front; Ph_8 - the helical PVC structure is formed inducing

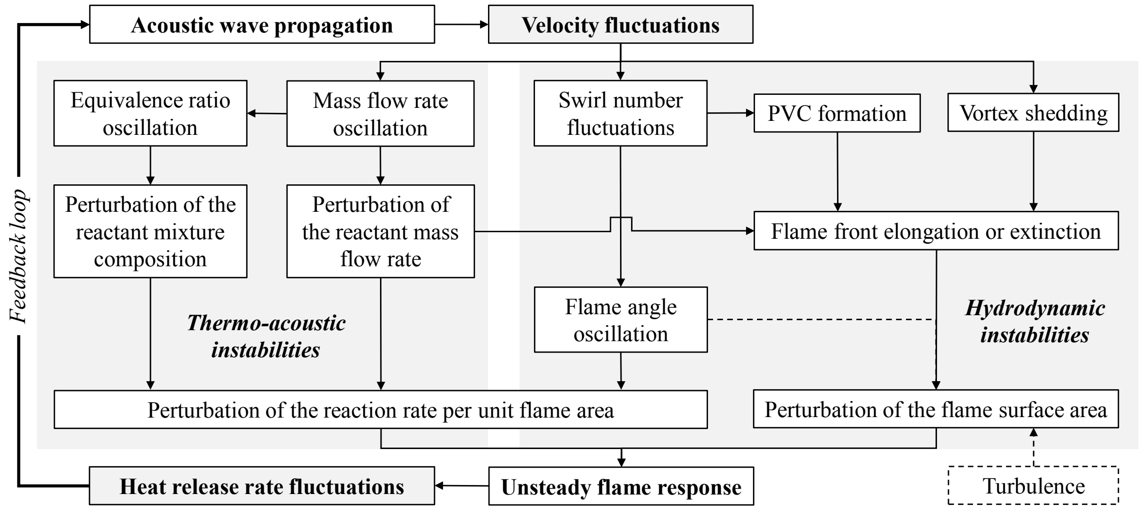

Figure 4.14: Schematic overview of the different thermo-acoustic and hydrodynamic instability mechanisms and their role in sustaining the governing feedback loop underlying the limit-cycle oscillation.

additional non-axisymmetric flame roll-up; Ph_1 - the flame angle becomes maximum, further increasing the reaction rate per unit flame ‘area’; Ph_2 - the global HRR reaches its peak while the local mixture mass flow rate and equivalence ratio begin to decrease again; Ph_3 - the toroidal vortex and PVC are both completely suppressed and the entire sequence of events repeats itself from Ph_4. The full governing feedback loop including the various instability mechanisms identified in the above sections is summarised schematically in Figure 4.14.

4.5 Concluding remarks

The combined effects of self-excited thermo-acoustic and hydrodynamic instabilities in gas turbines were investigated using LES. These types of instabilities are often encountered in the late design stages of modern low-emission combustors and need to be systematically prevented. The targeted PRECCINSTA combustor involves a partially premixed, swirl-stabilised flame and has previously been shown to exhibit combustion-driven instabilities under certain operating conditions. Major findings are:

- In line with previous experimental observations, the conducted LES successfully captured a fully self-excited limit-cycle oscillation without any external forcing.
- The global heat release rate and combustion chamber pressure were found to fluctuate in phase, thereby globally satisfying the Rayleigh criterion.

- The frequency and amplitude of the dominant thermo-acoustic mode (300 Hz) as well as its first harmonic were in excellent agreement with available measurement data.
- A superposition of mass flow rate and equivalence ratio oscillations - governed by a periodically varying pressure drop between the air plenum and combustion chamber - was identified as the main driving mechanism underlying the feedback loop.
- Phase-averaged radial profiles of the velocity, temperature and species mass fractions were used to quantify the dynamic behaviour of the flame and flow field.
- Acoustic waves impinging on the swirler unit led to the formation of various hydrodynamic phenomena, i.e. flame angle oscillation, toroidal vortex shedding and a precessing vortex core, by generating swirl number fluctuations. These phenomena arose and evolved periodically, thus establishing a direct link to the dominant thermo-acoustic mode.
- The precessing vortex core and toroidal vortex shedding mechanism were found to play a vital role in local flame extinction and mixing of fuel and oxidiser. Both were furthermore shown to roll up the flame front, thereby modulating its instantaneous ‘surface area’ and local heat release.
- The combined oscillation cycle featured regular flashback and lift-off events as well as the periodic transition between an attached **V**-shape and a lifted **M**-shape flame.
- An in-phase relationship of the flame’s ‘surface area’, flame-averaged mixture fraction and global heat release rate was observed and quantified.
- The overall sequence of amplification and attenuation was summarised, revealing the coupling between the different feedback mechanisms.

In conclusion, the computational method’s capability to compute complex, partially premixed, reacting flow problems undergoing self-excited combustion instabilities was demonstrated, laying out a basis for future work, which will include more detailed time-resolved analyses of the different instability phenomena.

Chapter 5

Longitudinal and azimuthal instabilities in the SGT-100 combustor

Chapter 5 covers the final test case surrounding self-excited combustion instabilities in a full-scale, can-type industrial gas turbine combustor. In particular, the effects of different operating pressures on the combustor's thermo-acoustic behaviour are examined by means of compressible LES. Experimentally, such cases are rarely considered as they require special high pressure test rigs and introduce added complexity, including e.g. rapid window degradation, which impairs the accuracy of optical measurement techniques. Nevertheless, Buschhagen et al. (2019) recently conducted high pressure experiments of a single jet flame combustor observing a rotating transverse instability mode. The present LES investigation is one of the first of its kind to study self-exited transverse modes in a swirl-stabilised combustor operated at elevated pressures. Previous simulations of these types of modes at atmospheric pressure include the work of Ghani et al. (2015) who examined the superposition of longitudinal and transverse modes in an afterburner-type configuration. Selle et al. (2006) also identified an azimuthal mode in a swirl-stabilised configuration comparable to the SGT-100 combustor studied here.

The contents of this chapter have been submitted for publication in Fredrich et al. (2020c).

5.1 Test case formulation

With a power of up to 1 MW, the SGT-100 Dry Low Emissions (DLE) combustor is the smallest burner from the commercial range of industrial Siemens gas turbine (SGT) combustion chambers. It is capable of operating in either the partially premixed or diffusion burning regime and uses a swirling flow configuration with inner and outer recirculation zones to stabilise the flame front.

5.1.1 Measurement campaign

A comprehensive measurement campaign of the original-sized DLE combustor was carried out by Stopper et al. (2013) as part of the TurChemi (**Tur**bulence and **Chemi**stry Interaction) project. The combustor was operated with German Natural Gas at different fuel-lean, partially premixed operating conditions and elevated pressures between 3 and 6 bar - labelled Cases A through D with bulk Reynolds numbers in the range of 39,000–120,000. The test rig comprised a cylindrical air plenum and flow conditioner, which supplied preheated air into the radial swirler unit. The latter was made up of 12 rectangular vanes with multiple fuel injection holes each and was succeeded by a circular pre-chamber for enhanced mixing of fuel and oxidiser. The ensuing dump expansion (defined as the combustion chamber entry plane $\mathbf{x} = 0$ mm) led into an approximately 0.5 m long, square cross-section combustion chamber with quartz glass side walls enabling optical access for laser-based measurements. Details of the optical and laser-optical set-ups including particle image velocimetry (PIV), one-dimensional laser Raman scattering, OH* chemiluminescence, OH PLIF and acoustic measurements can be found in Stopper et al. (2010, 2009); along with the estimated measurement uncertainties shown in Table 5.1. The combustion chamber ended in a duct contraction converging into a short circular pipe. It was followed by a 1 m long circular exhaust pipe and subsequent spray water section connected to the atmosphere.

The main objective of this experimental investigation was to gain a better understanding of gas turbine combustion under realistic conditions and to provide a comprehensive experi-

Table 5.1: Estimated total errors of the experimental PIV and Raman measurements, Stopper et al. (2013).

	Vel. [%]	T [%]	CH_4 [%]	O_2 [%]	N_2 [%]	CO_2 [%]	H_2O [%]
Reactants	5	6	4	6	5	-	-
Products	5	13	-	21	6	20	14

mental database for the validation of numerical methods. However, during the measurements, self-excited thermo-acoustic flame oscillations were reported for the 6 bar case, which were accompanied by an axial motion of the IRZ, as well as vortex shedding from the burner rim. These oscillations were attributed to periodic variations of the reactants' mixture fraction induced by different acoustic impedances of the fuel and air supply streams. Karlis et al. (2019b) recently analysed the original measurement data from Cases A and B to further investigate the combustor's unstable thermo-acoustic behaviour. They applied phase-averaging to characterise the limit-cycle perpetuation mechanism, including the shedding of toroidal vortices. A dynamic mode decomposition (DMD) analysis was employed to examine the occurrence of periodic, asymmetric combustion in the ORZ. Flame kernels appearing in this region were argued to be the result of mixture Lewis number non-uniformities, which in combination with high strain rates along the OSL, can lead to a locally increased heat release.

5.1.2 Previous numerical works

Previous numerical works in the literature have specifically targeted the SGT-100 combustor to evaluate the performance of different chemical reaction mechanisms, Abou-Taouk et al. (2013); Bulat et al. (2015a) and LES combustion models, Abou-Taouk et al. (2016, 2013); Bulat et al. (2013, 2014); Fedina et al. (2017); Jaravel et al. (2017); Langella et al. (2018) based on Case A (3 bar). An isothermal flow case was simulated by Bulat et al. (2015b), who identified both a PVC and an exit vortex core (EVC) inside of the combustion chamber, whereas Xia et al. (2018a) studied the dispersion of artificially induced entropy perturbations. The actual combustor geometry deployed in gas turbines was investigated by Bulat et al. (2009) and Sadasivuni et al. (2012) using SAS methods.

Xia et al. (2019, 2018b, 2017) recently applied a coupled approach combining incompressible LES with a low order acoustic network solver to study the thermo-acoustically unstable Case B (6 bar). The combustor's FDF was extracted by periodically forcing the inflow velocity at different frequencies and amplitudes, while measuring the subsequent heat release response. A governing limit-cycle oscillation was identified by feeding the obtained FDF back into the acoustic solver, providing the dominant modes and growth rates. The predicted oscillation was found to be driven by a longitudinal thermo-acoustic mode at a frequency of about 209 Hz - closely matching the experimentally measured value.

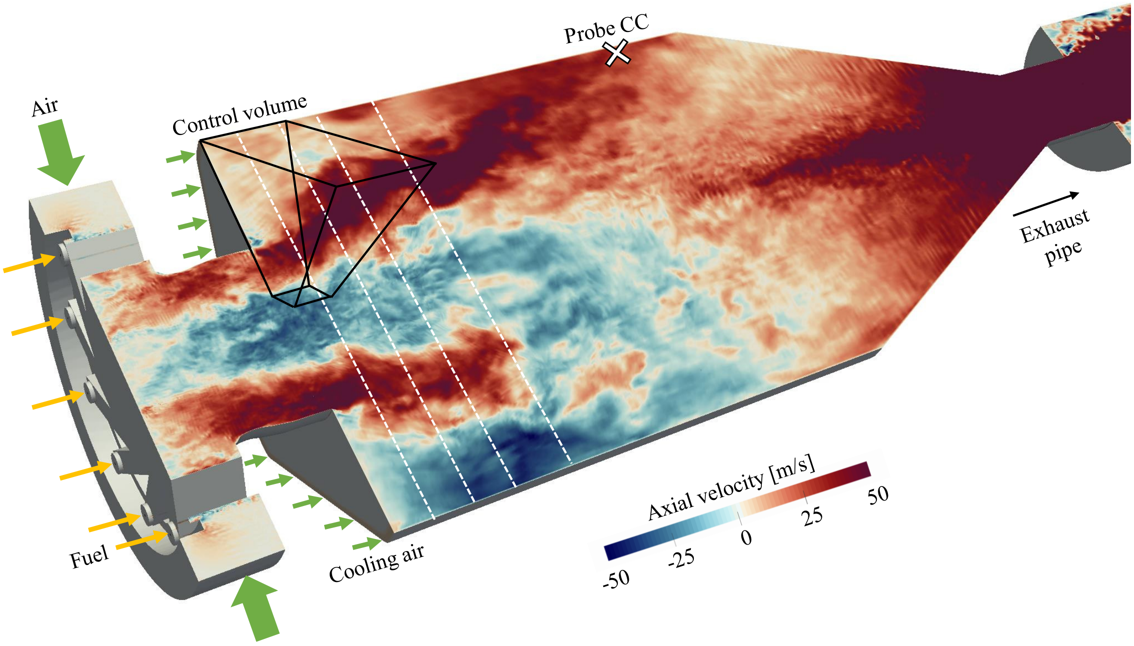

Figure 5.1: Vertical cut through the combustor geometry indicating the locations of all computational inflows as well as probe CC. Overlaid by an instantaneous snapshot of the axial velocity from the 6 bar case.

Table 5.2: Summary of the simulated combustor operating conditions (Cases A and B) based on the experiments, Stopper et al. (2013).

Case	p_{mean} [bar]	T_{air} [K]	T_{fuel} [K]	U_{air} [m/s]	$\dot{m}_{\mathrm{air}}$ [g/s]	$\dot{m}_{\mathrm{fuel}}$ [g/s]	Φ_{glob} [-]	Z_{glob} [-]	P_{th} [kW]
A	3	682	305	167	4.99	6.24	0.60	.033	335
B	6	683	304	320	4.78	12.8	0.63	.035	685

Table 5.3: Simplified fuel composition used in the current LES - in accordance with previous work, Bulat et al. (2014).

	CH_4 [%]	C_2H_6 [%]	C_3H_8 [%]	C_4H_{10} [%]	CO_2 [%]	N_2 [%]
Exp.	96.97	1.55	0.35	0.10	0.27	0.75
LES	98.97	-	-	-	0.27	0.75

5.2 Computational set-up

In the present work, compressible LES is utilised for the first time to investigate the unstable behaviour of the SGT-100 combustor shown in Fig. 5.1. The full-scale combustor geometry from the experiments by Stopper et al. (2013) is preserved using a computational mesh of about 8.3 million grid points. The mesh is derived from the work of Bulat et al. (2015b) and has been extended further downstream to incorporate the full length of the exhaust pipe. A non-reflective outflow boundary condition is applied to emulate the acoustic energy dissipation introduced by the test rig's spray water section. On the upstream end, the complex geometry of the air plenum and the perforated plate installed as a flow conditioner are excluded from the simulation domain. Instead, the computational inflow is located just upstream of the radial swirler inlet. The small holes of the perforated plate are assumed to impose a high impedance, thus both the velocity and density (i.e. mass flow rate) of the incoming air stream are fixed based on the experimental operating conditions specified in Table 5.2. Note that the bulk flow velocity and global equivalence ratio remain approximately constant between Cases A and B. The mass flow rates of the small fuel jets located inside the swirler unit are also fixed. In accordance with Bulat et al. (2014), a marginally simplified fuel composition is used by combining all higher hydrocarbons into methane as summarised in Table 5.3. The cooling air stream injected around the outermost radius of the combustor base plate in the experimental set-up is also included as shown in Fig. 5.1. Isothermal temperatures of 1300 K and 700 K are prescribed on the combustion chamber side and base plate walls, respectively, to account for heat loss through the walls, whereas radiative heat transfer is neglected. The chemistry is represented via the 15-step / 19 species methane mechanism proposed by Lu and Law (2008).

5.3 Results and discussion

The combustor's operating behaviour is examined based on selected results from Cases A and B; with a specific focus on the latter. This is followed by a more detailed description of the observed azimuthally spinning instability mode and its underlying driving mechanism. Finally, time-averaged statistics are presented to further elaborate on the simulation's agreement with the experimental measurements.

5.3.1 Thermo-acoustic behaviour

In order to characterise the combustor's thermo-acoustic behaviour, fluctuations of the local pressure and global HRR are shown in Figs. 5.2 and 5.3 for the 3 and 6 bar case, respectively.

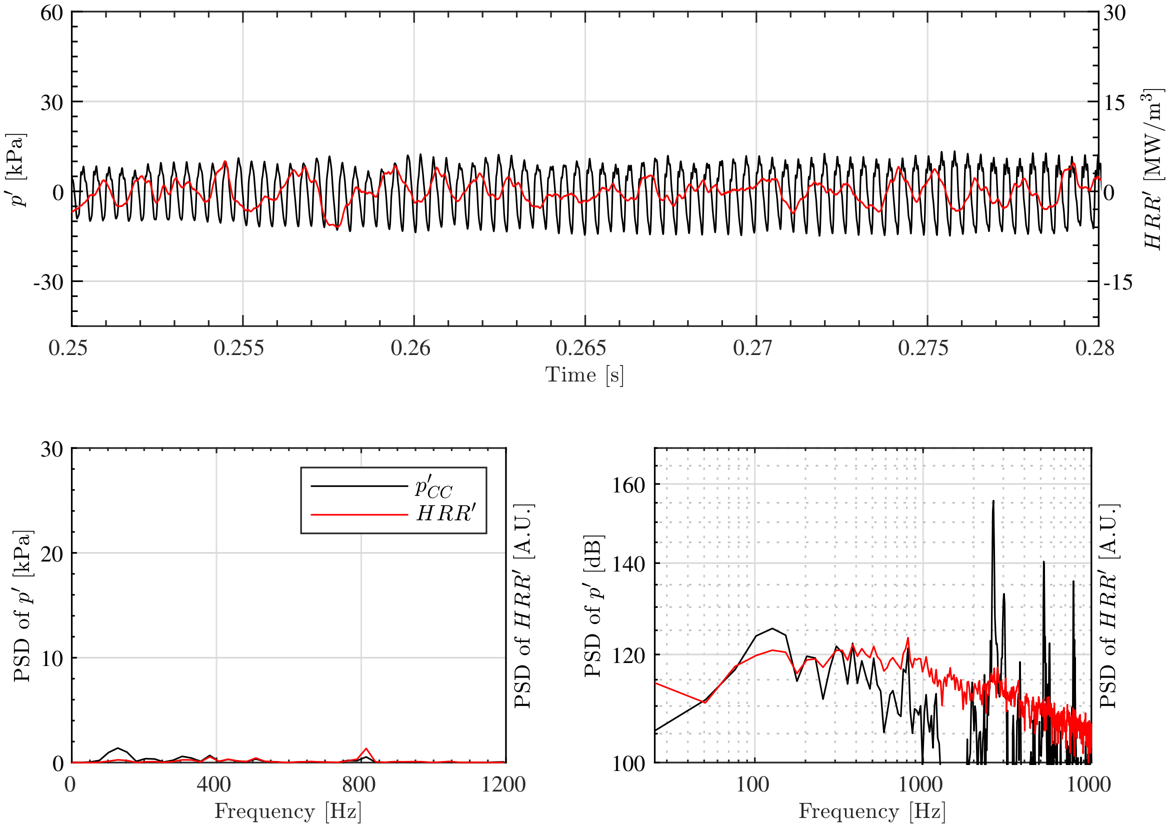

Figure 5.2: Thermo-acoustic behaviour of the 3 bar case. Top: Time signals of the global heat release rate and the local pressure fluctuations recorded at probe CC. Bottom: Their respective power spectral densities.

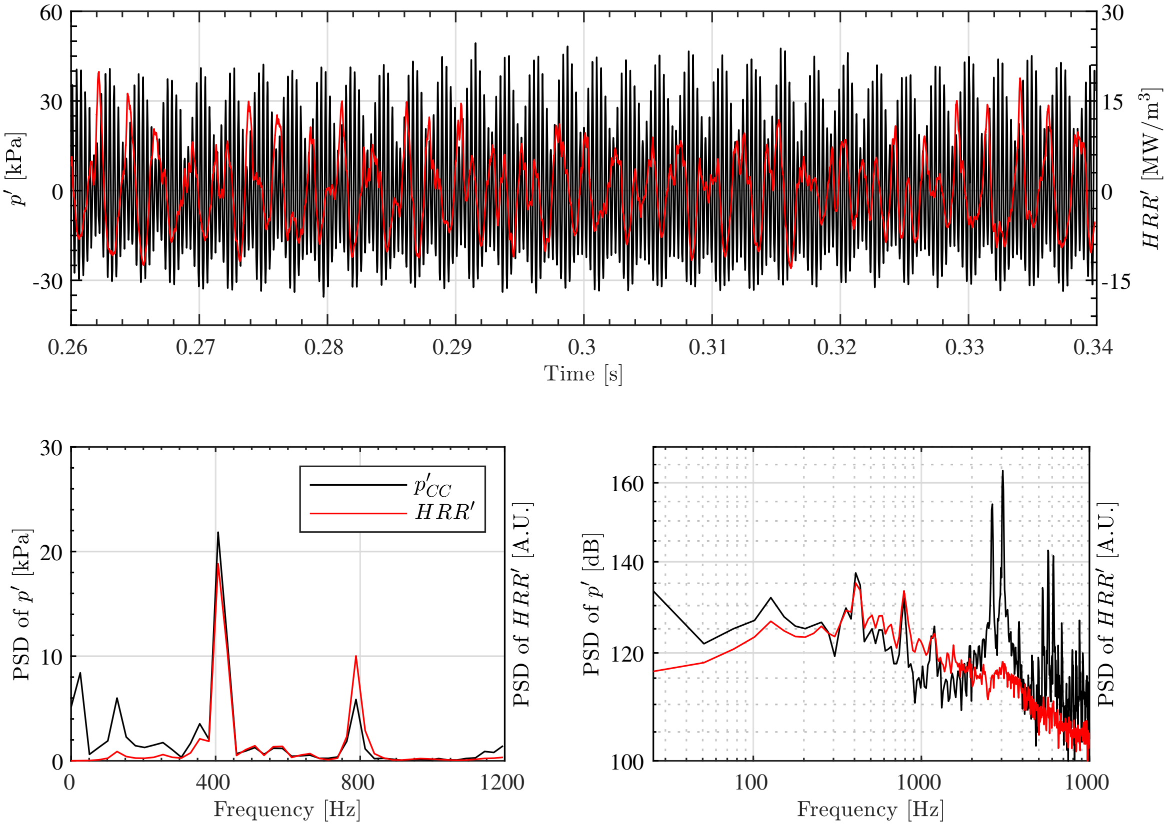

Figure 5.3: Thermo-acoustic behaviour of the 6 bar case. Top: Time signals of the global heat release rate and the local pressure fluctuations recorded at probe CC. Bottom: Their respective power spectral densities.

The local pressure was monitored at probe CC (see Fig. 5.1), positioned 231 mm downstream of the combustion chamber entry plane; identical to the location of the experimental pressure transducer. In addition, the global HRR was spatially integrated over the entirety of the computed domain. Case A exhibits pressure fluctuations with a relative amplitude of about 6% compared to its mean operating pressure of 3 bar. This value is considered to be fairly low and matches the maximum amplitude reported in the measurements, Karlis et al. (2019b). A PSD analysis is employed to quantify the signals' power distribution over the frequency spectrum. For the pressure, two dominant peaks at a frequency of around 2800 Hz are revealed, supplemented by their respective higher harmonics. In contrast, the power spectrum of the HRR shows no pronounced peaks, demonstrating the thermo-acoustically stable operating behaviour of Case A - as first reported in the experiments, Stopper et al. (2013).

Upon raising the mean operating pressure to 6 bar (Case B), the relative amplitude of the pressure fluctuation increases considerably to about 12%. In absolute terms, this value is approximately four times higher than in Case A, while the HRR fluctuations are up to two and a half times as high. Examining the PSD of both signals, the previously identified high frequency pressure modes of about 3000 Hz can be observed again. However, the spectrum also displays another fundamental peak at 400 Hz, as well as its first two harmonics. This second mode represents a low frequency longitudinal mode, which propagates up- and downstream within the domain. Its PSD amplitude of just over 20 kPa is found to be in very good agreement with the measurements. A minor over-prediction of the pressure fluctuation amplitude is generally to be expected in LES, due to the additional acoustic damping effects that often appear in experimental set-ups. More crucially, the HRR spectrum in Case B also shows a peak at 400 Hz, revealing the thermo-acoustic coupling between the longitudinal pressure mode and the global flame response. The perpetuation of a limit-cycle oscillation with respect to the longitudinal direction can therefore be concluded, as previously stated by Karlis et al. (2019b) and Xia et al. (2019). However, compared to these two prior works, the oscillation frequency in the current simulation is increased by a factor of two. Note that the 400 Hz mode was also predicted by Xia et al. (2019), albeit with a negative growth rate. An improved boundary condition treatment, i.e. more realistic acoustic impedances, may ultimately lead to a more accurate frequency prediction. In fact, Xia et al. (2019) did use a much smaller upstream reflection coefficient based on modelling of the acoustics and achieved very good agreement with the experiments.

5.3.2 Azimuthally spinning mode

The physical nature of the obtained high frequency peaks is examined next, based on the 6 bar case. They are found to represent a transverse - or more specifically an azimuthal -

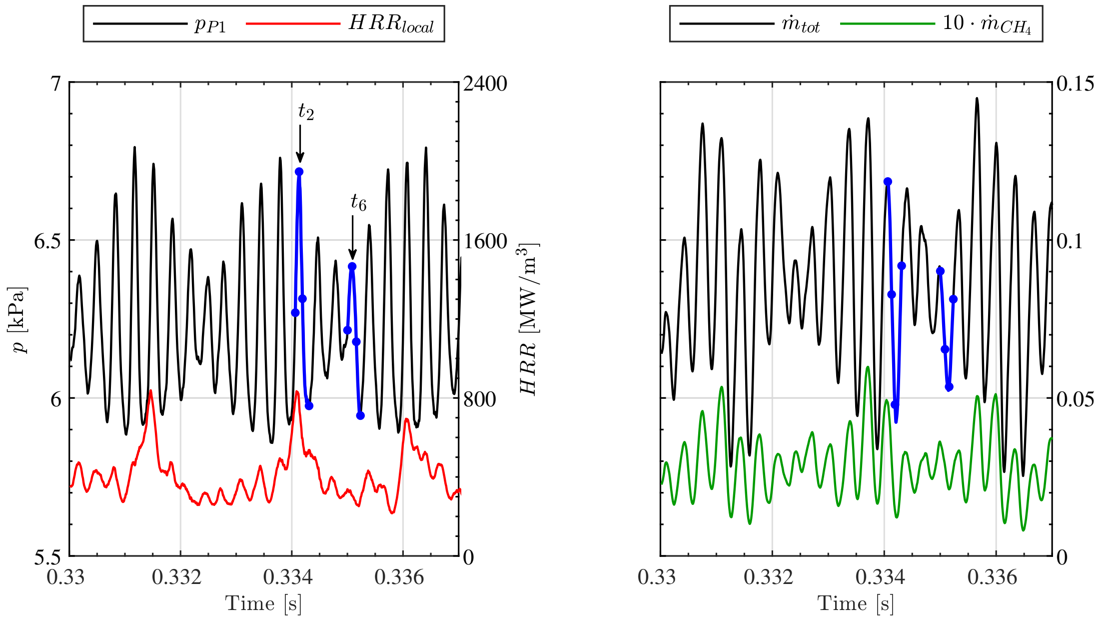

Figure 5.4: Left: Temporal evolution of the HRR, locally integrated over the control volume, and the local pressure at probe P1. Right: Temporal evolution of $\dot{m}_{CH_4}$, scaled by a factor of 10, and $\dot{m}_{tot}$ entering the control volume at $\mathbf{x} = 0$ mm. The blue markers indicate different instants of time from t_1 to t_8.

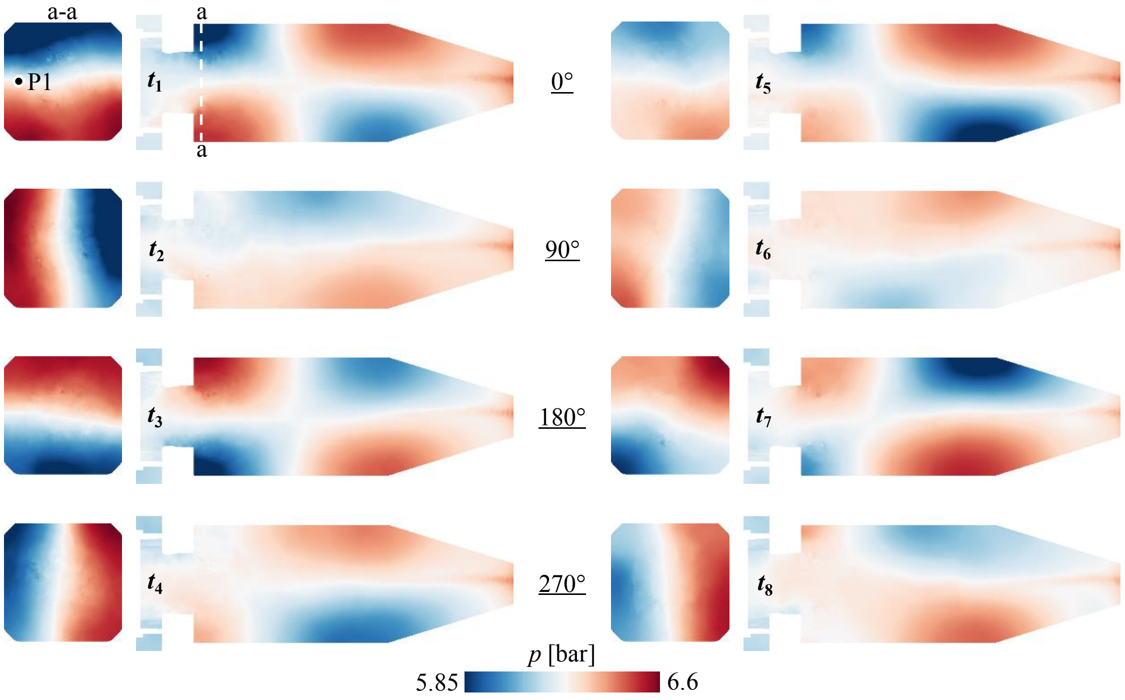

Figure 5.5: Instantaneous snapshots of pressure in an axial and a vertical plane showing two full periods of the azimuthal mode as it is locally amplified (t_{1-4}) and attenuated (t_{5-8}) by the superimposed longitudinal mode.

mode, that rotates about the central burner axis at the speed of sound. The observed splitting of the azimuthal modal peaks may be attributed to the influence of the mean azimuthal flow velocity on the co- and counter-rotating acoustic waves, i.e. $c \pm u_\theta$.

As evident from the above HRR signals, the azimuthal mode has no direct effect on the global flame response. It may however, impact the spatial heat release distribution in the transverse direction and provoke thermo-acoustic coupling by locally satisfying the Rayleigh criterion. This can be shown by spatially integrating the HRR over a control volume (see Fig. 5.1) representing one quarter sector of the combustion chamber. Figure 5.4 displays the resulting HRR signal over time and compares it to the local pressure recorded at probe P1; in the approximate centre of this control volume. The two quantities clearly oscillate in phase, indicating the instability is locally perpetuated. The associated asymmetric modulation of the flame's heat release cancels out circumferentially and is thus not detectable in the global HRR signal. In order to determine the underlying feedback mechanism of this azimuthal instability, both the fuel and total mixture mass flow rates entering the control volume are also shown in Fig. 5.4. Their respective oscillations are directly controlled by the local pressure fluctuations, thereby modulating the supply of unburnt reactants to the flame. The subsequent unsteady flame response generates periodic heat release fluctuations that drive the spinning pressure structure. The superposition of this azimuthal feedback loop with the low frequency longitudinal mode leads to the characteristic pressure signal obtained in Figs. 5.3 and 5.4. The corresponding evolution of the pressure field is shown in Fig. 5.5 for eight different instants of time, t_{1-8} (cf. Fig. 5.4). These represent two periods of the azimuthal oscillation superimposed by, respectively, the maximum (t_{1-4}) and minimum (t_{5-8}) pressure phase of the longitudinal mode. The resulting local amplification or attenuation of the spinning pressure structure is clearly visible.

5.3.3 Time-averaged statistics

Figures 5.6 and 5.7 show radial profiles of, respectively, the axial and radial velocity components as well as the temperature and mixture fraction. These are plotted for four different downstream locations - indicated by white dashed lines in Fig. 5.1 - and compared against the corresponding experimental data by Stopper et al. (2013). In terms of the velocities, both the time-averaged and RMS results obtained from the simulation are in good agreement with the measurements, i.e. the location and strength of the IRZ, ORZ and annular jet of unburnt reactants are accurately captured. A minor under-prediction of the jet's spreading angle can be deduced from the slight inwards shift of the two velocity maxima and thus narrower IRZ. Looking at the time-averaged temperature profiles, it becomes clear that the flame length is significantly underestimated. This is consistent with previous LES studies of the SGT-100

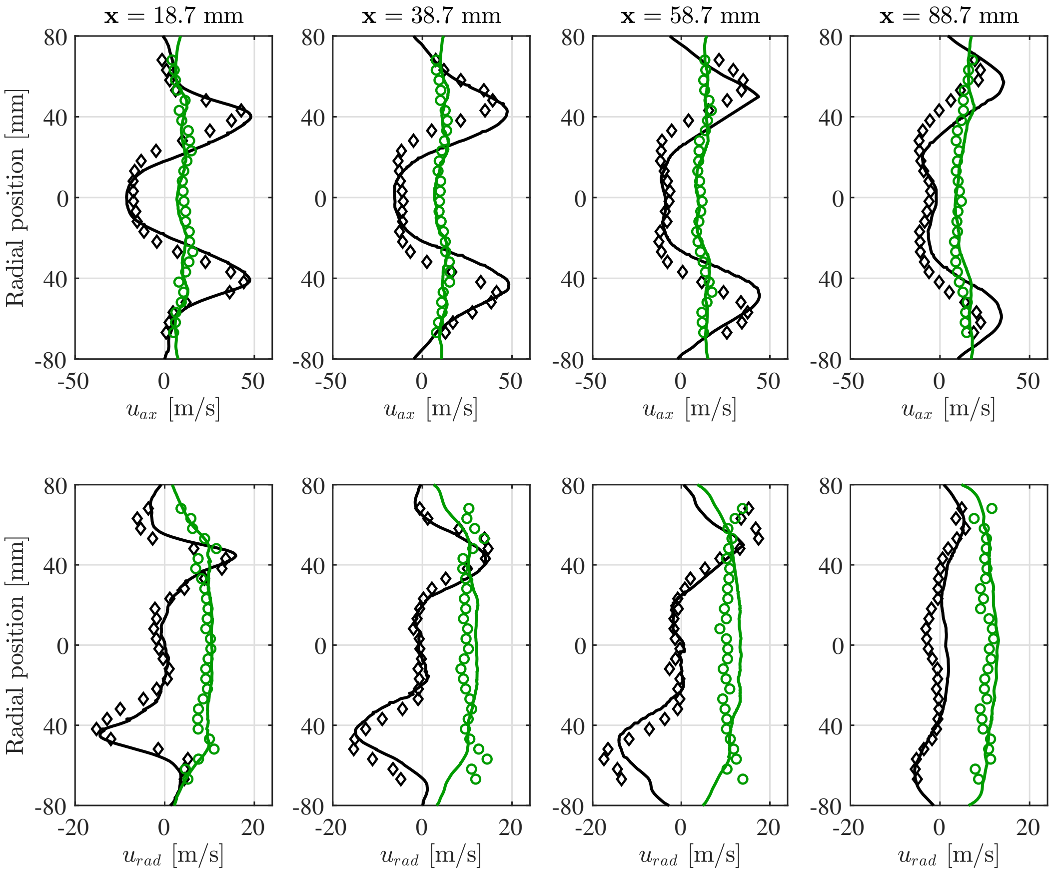

Figure 5.6: Radial profiles of the time-averaged (black) and RMS (green) axial and radial velocity components, u_{ax} and u_{rad}, at four different downstream locations $\mathbf{x}$ - lines: simulation, symbols: experiment.

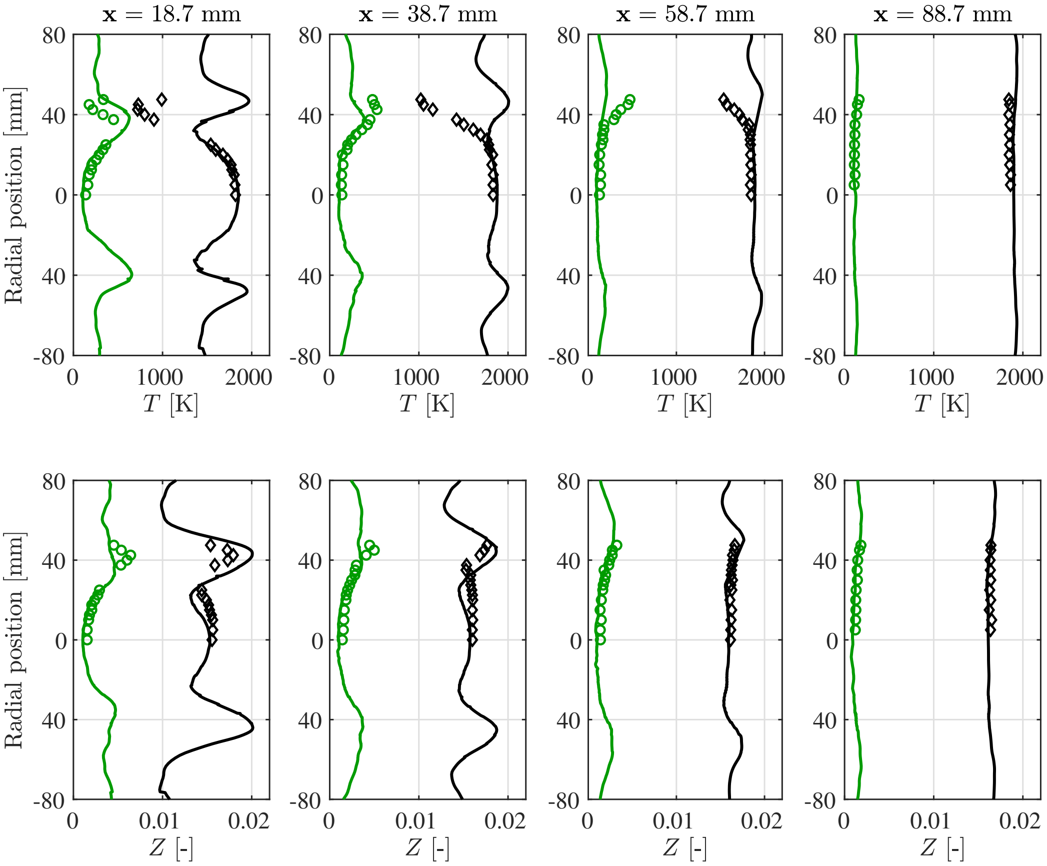

Figure 5.7: Radial profiles of the time-averaged (black) and RMS (green) temperature T and mixture fraction Z at four different downstream locations $\mathbf{x}$ - lines: simulation, symbols: experiment.

combustor, though the exact reasons for the shortening are unclear. The temperatures within the IRZ, on the other hand, are well predicted and the inner flame front is correctly situated around the ISL at $r \approx 20$ mm. High temperatures along the OSL ($r \approx 60$ mm) suggest that the outer flame front does not lift off in the simulation. Such flame lift-off was observed in the experiments and attributed to the mixture's local ignition delay time, Stopper et al. (2013). Nevertheless, radial profiles of the time-averaged mixture fraction are in overall good agreement and results at the final downstream position indicate that the global equivalence ratio, adiabatic flame temperature and wall heat loss are adequately represented in the LES. Finally, RMS profiles of both the temperature and mixture fraction are shown to be well captured also. Although previous numerical works had been unable to reproduce elevated fluctuation levels within the IRZ, the azimuthally spinning mode predicted in the current work is likely responsible for generating increased RMS values in this region.

5.4 Concluding remarks

The effect of operating pressure on the thermo-acoustic behaviour of an industrial gas turbine combustor was studied using compressible LES. For this purpose, two different combustor operating conditions - named Cases A (3 bar) and B (6 bar) - were simulated, both of which exhibited fluctuations of the local pressure and global HRR. In line with prior experimental observations, the respective fluctuation amplitudes increased significantly when raising the operating pressure from 3 to 6 bar. A high frequency, azimuthally spinning mode of about 2800-3000 Hz was identified in both cases and determined to have virtually no impact on the global flame response. At a mean pressure of 6 bar, this azimuthal mode was superimposed by an additional longitudinal mode with a lower frequency of approximately 400 Hz. The latter was shown to be thermo-acoustically coupled to the global HRR, therefore driving a limit-cycle oscillation in the longitudinal direction. The governing feedback mechanism of the azimuthal mode was subsequently examined in more detail. Its spinning pressure structure was found to locally modulate the fuel and total mixture mass flow rates entering the main flame region. This variation of the incoming reactant stream led to fluctuations of the local HRR, which in turn drove the pressure perturbation, thereby closing the feedback loop. Finally, time-averaged and RMS radial profiles of the velocity and mixture fraction were shown to be in good agreement with the available experimental data. Results of the temperature, however, indicated an under-predicted flame length in accordance with previous numerical studies. Future work will include the simulation of modified geometries in an attempt to find ways of damping the observed thermo-acoustic instability, e.g. by breaking the combustor's axisymmetry.

Chapter 6

Conclusion

Modern low-emission aero-engine and stationary gas turbine combustors typically operate under lean, partially premixed conditions and employ swirling flows for flame stabilisation purposes. However, despite being highly effective in the reduction of environmentally harmful pollutant emissions, these state-of-the-art combustor configurations are often prone to the onset of undesirable, self-excited combustion instabilities, which must be systematically prevented at engine level. Within this framework, the present work aimed at devising an accurate and reliable LES method capable of predicting combustion instabilities in the early design stages of novel gas turbine combustors. The feedback mechanisms of both thermo-acoustic and hydrodynamic instability phenomena were then investigated to gain a better understanding of their underlying physics. This final chapter recaps the main conclusions drawn from the work carried out as part of this thesis and provides an outlook on potential developments in the field, as well as future work associated with the conducted research.

6.1 Summary of key findings

A broad range of test cases from basic non-reacting, inviscid flow problems in simple geometries, to more complex, turbulent reacting flows in sophisticated, lab-scale model and full-scale industrial gas turbine combustors were covered throughout this work. Key findings from these studies with respect to the overall solver capabilities and the study of combustion instabilities are summarised in the following sections.

6.1.1 Overall solver capabilities

A fully compressible LES code (called BOFFIN) for the simulation of turbulent reacting flows was successfully derived. The code incorporates a modelled transported *pdf* equation, which is solved via the Eulerian stochastic fields method to represent turbulence-chemistry interactions. This approach provides a burning regime independent description of turbulent flames and can be easily complemented with any suitable chemical mechanism. The results of this work have shown that the employed LES-*pdf* methodology may be applied to a wide variety of flow problems in complicated geometries without any adjustment, or tuning of model parameters, i.e. it has wide ranging applicability. The importance of wall heat transfer and the mixing process of fuel and air were furthermore underlined and should thus be generally accounted for in the modelling.

In its compressible formulation, BOFFIN was proven to be capable of accurately resolving acoustic wave propagation including both longitudinal and transverse (azimuthal) modes. This allowed for the reproduction of complex self-excited thermo-acoustic and hydrodynamic instabilities, which are known to be extremely difficult to study due to their highly non-linear behaviour. For this purpose, a non-reflective outflow boundary condition was implemented into the code and subsequently shown to effectively reduce acoustic wave reflection at the domain outlets. The novel, fully compressible LES method may ultimately provide a cost-effective tool in the development process of modern gas turbines, in particular to examine the thermo-acoustic behaviour of prospective combustor designs, to confirm their stability or otherwise.

6.1.2 Combustion instabilities

Two partially premixed, swirl-stabilised gas turbine combustor configurations were investigated in this work, both of which are known to become thermo-acoustically unstable at certain operating conditions. The main observations from these studies are listed below:

- A distinct limit-cycle oscillation driven by various self-excited thermo-acoustic and hydrodynamic instability phenomena was identified in the PRECCINSTA model combustor.
- These phenomena were shown to be governed by a periodically varying pressure drop between the combustion chamber and air plenum due to acoustic wave propagation.
- The resulting mass flow rate and equivalence ratio oscillations controlled the supply of unburnt reactants to the flame front and thereby modulated its global heat release response.
- The interaction of acoustic waves with the swirler unit generated swirl number fluctuations, which furthermore led to flame angle oscillations as well as the periodic formation of a precessing vortex core and toroidal vortex shedding.

- A comprehensive description of the combined feedback loop featuring an in-phase relationship between the global heat release rate, flame ‘surface area’ and flame-averaged mixture fraction was finally provided.
- Combustion instabilities simulated in the industrial SGT-100 combustor, on the other hand, were found to be driven by the superposition of a low frequency longitudinal mode and a high frequency azimuthally spinning mode.
- The former was directly linked to oscillations of the global heat release rate. The latter was thermo-acoustically coupled in the transverse direction and only satisfied the Rayleigh criterion locally, therefore not impacting the global flame response.
- In line with prior experimental results, the overall instability amplitude was shown to be amplified upon increasing the combustor’s mean operating pressure from 3 to 6 bar.

In summary, the work carried out in this thesis constitutes one of the first in-depth computational research efforts to study the physical mechanisms of self-excited, combustion-driven instabilities in gas turbines.

6.2 Outlook and future work

Future work will involve the ongoing investigation of combustion instability mechanisms based on the PRECCINSTA test case. One potential scope is to quantify the effect large-scale vortical structures exert on the flame’s heat release and ‘surface area’. This can be done e.g., by spatially tracking the position of the precessing vortex core over time and correlating it to the local heat release rate. For this purpose, a perfectly premixed case will need to be considered in order to eliminate the influence of equivalence ratio oscillations. The observed hydrodynamic phenomena can thereby be isolated, as previously done in several experiments. BOFFIN also allows to modify certain parameters of the combustor geometry and study the subsequent thermo-acoustic response, e.g. control the time lag linked to fuel accumulation and convection by changing the distance between the point of fuel injection and the flame front. Additional phase-averaging, though very useful for a better understanding of the oscillating flow behaviour, will have to be weighed against its high computational costs. The use of proper orthogonal decomposition (POD) or dynamic mode decomposition (DMD) techniques may provide valuable knowledge of the dominant instability modes including their spatial and temporal evolution.

POD / DMD might also be able to further qualify the different instability modes, i.e. longitudinal and azimuthal, identified in the SGT-100 combustor. Moreover, given the significant mismatch between the predicted and measured frequency of the longitudinal mode in this case, an adjusted boundary treatment needs to be considered. This implies either a modification of the computed domain by incorporating extended parts of the test rig geometry, i.e. the upstream air plenum and / or the downstream water spray section, or, the prescription of more realistic acoustic impedances at the current inflow and outflow boundaries. Finally, it is possible to carry out a parameter study of different design features to explore ways of damping the observed thermo-acoustic instability, e.g. by breaking the combustor's axisymmetry.

Given BOFFIN's flexibility with respect to combustion regimes and chemical mechanisms, other possible applications in related fields may also be considered. This includes evaluating the feasibility of hydrogen-enriched combustion in gas turbines - an idea receiving increased attention as of late. Hydrogen (H_2) production is currently discussed as a potential means for energy storage, e.g. at times when the local power grid is saturated and excess energy generated from renewable sources could be used to produce H_2. This H_2 can then subsequently be added to conventional fuel blends in low proportions and burned in gas turbines for power generation purposes when needed. However, the high energy density and burning rate associated with H_2 is known to affect flame stability and potentially increase the risk of flame flashback. The present work has shown that both flame instability and flashback events can be predicted with the current, fully compressible LES-*pdf* approach, making it a viable option for future research in this field. Preliminary studies of hydrogen-enriched combustion are currently being carried out for both the PRECCINSTA and SGT-100 case. However, with increased H_2 concentrations in the fuel, non-unity Lewis number effects need to be addressed in the modelling.

Bibliography

Abou-Taouk, A., Farcy, B., Domingo, P., Vervisch, L., Sadasivuni, S., and Eriksson, L. E. (2016). Optimized reduced chemistry and molecular transport for large eddy simulation of partially premixed combustion in a gas turbine. *Combust. Sci. Technol.*, 188(1):21–39.

Abou-Taouk, A., Sadasivuni, S., Loerstad, D., and Eriksson, L. E. (2013). Evaluation of Global Mechanisms for LES Analysis of SGT-100 DLE Combustion System. In *Proc. ASME Turbo Expo 2013 Turbine Tech. Conf. Expo.*, pages 1–13.

Acharya, V. S., Shin, D. H., and Lieuwen, T. (2013). Premixed flames excited by helical disturbances: Flame wrinkling and heat release oscillations. *J. Propuls. Power*, 29(6):1282–1291.

Ahmed, M. M. and Birouk, M. (2018). Effect of fuel nozzle geometry and airflow swirl on the coherent structures of partially premixed methane flame under flashback conditions. *Exp. Therm. Fluid Sci.*, 99(April):304–314.

An, Q., Kwong, W. Y., Geraedts, B. D., and Steinberg, A. M. (2016). Coupled dynamics of lift-off and precessing vortex core formation in swirl flames. *Combust. Flame*, 168:228–239.

An, Q. and Steinberg, A. M. (2019). The role of strain rate, local extinction, and hydrodynamic instability on transition between attached and lifted swirl flames. *Combust. Flame*, 199:267–278.

Angelberger, C., Veynante, D., and Egolfopoulos, F. (2000). LES of chemical and acoustic forcing of a premixed dump combustor. *Flow, Turbul. Combust.*, 65(2):205–222.

Ansari, N., Strakey, P. A., Goldin, G. M., and Givi, P. (2015). Filtered density function simulation of a realistic swirled combustor. *Proc. Combust. Inst.*, 35(2):1433–1442.

Balachandran, R., Ayoola, B., Kaminski, C., Dowling, A., and Mastorakos, E. (2005). Experimental investigation of the nonlinear response of turbulent premixed flames to imposed inlet velocity oscillations. *Combust. Flame*, 143:37–55.

Barlow, R. S., Karpetis, A. N., Frank, J. H., and Chen, J. Y. (2001). Scalar profiles and NO formation in laminar opposed-flow partially premixed methane/air flames. *Combust. Flame*, 127(3):2102–2118.

Bauerheim, M., Staffelbach, G., Worth, N. A., Dawson, J. R., Gicquel, L. Y., and Poinsot, T. (2015). Sensitivity of LES-based harmonic flame response model for turbulent swirled flames and impact on the stability of azimuthal modes. *Proc. Combust. Inst.*, 35(3):3355–3363.

Baum, J. D. and Levine, J. N. (1982). Numerical techniques for solving nonlinear instability problems in solid rocket motors. *AIAA J.*, 20(7):955–961.

Beér, J. M. and Chigier, N. A. (1983). *Combustion Aerodynamics*. Krieger Publishing Company, reprint edition.

Benard, P., Lartigue, G., Moureau, V., and Mercier, R. (2019). Large-Eddy Simulation of the lean-premixed PRECCINSTA burner with wall heat loss. *Proc. Combust. Inst.*, 37(4):5233–5243.

Berger, F. M., Hummel, T., Hertweck, M., Kaufmann, J., Schuermans, B., and Sattelmayer, T. (2017). High-frequency thermoacoustic modulation mechanisms in swirl-stabilized gas turbine combustors-part I: Experimental investigation of local flame response. *J. Eng. Gas Turbines Power*, 139(7):1–9.

Bloxsidge, G., Dowling, A. P., and Langhorne, P. J. (1988). Reheat buzz: an acoustically coupled combustion instability. Part 2. Theory. *J. Fluid Mech.*, 193:445–473.

Bourgouin, J. F., Durox, D., Moeck, J. P., Schuller, T., and Candel, S. (2013). Self-sustained instabilities in an annular combustor coupled by azimuthal and longitudinal acoustic modes. In *Proc. ASME Turbo Expo 2013 Turbine Tech. Confrence Expo.*, pages GT2013–95010.

Bourgouin, J. F., Durox, D., Moeck, J. P., Schuller, T., and Candel, S. (2015). A new pattern of instability observed in an annular combustor: The slanted mode. *Proc. Combust. Inst.*, 35(3):3237–3244.

Boxx, I., Arndt, C. M., Carter, C. D., and Meier, W. (2012). High-speed laser diagnostics for the study of flame dynamics in a lean premixed gas turbine model combustor. *Exp. Fluids*, 52(3):555–567.

Branley, N. and Jones, W. (2001). Large Eddy simulation of a turbulent non-premixed flame. *Combust. Flame*, 127(1-2):1914–1934.

Brauner, T. (2017). *Large eddy simulation of premixed and stratified turbulent combustion*. PhD thesis, Imperial College London.

Brauner, T., Jones, W. P., and Marquis, A. J. (2016). LES of the Cambridge Stratified Swirl Burner using a Sub-grid pdf Approach. *Flow, Turbul. Combust.*, 96(4):965–985.

Bulat, G. (2012). *Large eddy simulations of reacting swirling flows in an industrial burner*. PhD thesis, Imperial College London.

Bulat, G., Fedina, E., Fureby, C., Meier, W., and Stopper, U. (2015a). Reacting flow in an industrial gas turbine combustor: LES and experimental analysis. *Proc. Combust. Inst.*, 35(3):3175–3183.

Bulat, G., Jones, W. P., and Marquis, A. J. (2013). Large Eddy Simulation of an industrial gas-turbine combustion chamber using the sub-grid PDF method. *Proc. Combust. Inst.*, 34(2):3155–3164.

Bulat, G., Jones, W. P., and Marquis, A. J. (2014). NO and CO formation in an industrial gas-turbine combustion chamber using LES with the Eulerian sub-grid PDF method. *Combust. Flame*, 161(7):1804–1825.

Bulat, G., Jones, W. P., and Navarro-Martinez, S. (2015b). Large eddy simulations of isothermal confined swirling flow in an industrial gas-turbine. *Int. J. Heat Fluid Flow*, 51:50–64.

Bulat, G., Stopford, P., Turrell, M., Frach, D., Buchanan, E., and Stöhr, M. (2009). Prediction of aerodynamic frequencies in a gas turbine combustor using transient CFD. In *Proc. ASME Turbo Expo 2009 Power Land, Sea Air*, pages 1–10.

Buschhagen, T., Gejji, R., Philo, J., Tran, L., Bilbao, J. E. P., and Slabaugh, C. D. (2019). Self-excited transverse combustion instabilities in a high pressure lean premixed jet flame. *Proc. Combust. Inst.*, 37(4):5181–5188.

Candel, S., Durox, D., Schuller, T., Bourgouin, J.-F., and Moeck, J. P. (2014). Dynamics of swirling flames. *Annu. Rev. Fluid Mech.*, 46:147–173.

Caux-Brisebois, V., Steinberg, A. M., Arndt, C. M., and Meier, W. (2014). Thermo-acoustic velocity coupling in a swirl stabilized gas turbine model combustor. *Combust. Flame*, 161(12):3166–3180.

Chen, Z. X., Langella, I., Swaminathan, N., Stöhr, M., Meier, W., and Kolla, H. (2019a). Large Eddy Simulation of a dual swirl gas turbine combustor: Flame/flow structures and stabilisation under thermoacoustically stable and unstable conditions. *Combust. Flame*, 203:279–300.

Chen, Z. X., Swaminathan, N., Stöhr, M., and Meier, W. (2019b). Interaction between self-excited oscillations and fuel–air mixing in a dual swirl combustor. *Proc. Combust. Inst.*, 37(2):2325–2333.

Clayton, D. J. and Jones, W. P. (2008). Large Eddy Simulation of a Methane–Air Diffusion Flame. *Flow, Turbul. Combust.*, 81(4):497–521.

Colucci, P. J., Jaberi, F. a., Givi, P., and Pope, S. B. (1998). Filtered density function for large eddy simulation of turbulent reacting flows. *Phys. Fluids*, 10(2):499–515.

Ćosić, B., Terhaar, S., Moeck, J. P., and Paschereit, C. O. (2015). Response of a swirl-stabilized flame to simultaneous perturbations in equivalence ratio and velocity at high oscillation amplitudes. *Combust. Flame*, 162(4):1046–1062.

Crocco, L. (1969). Research on combustion instability in liquid propellant rockets. *Symp. Combust.*, 12(1):85–99.

Crocco, L. and Cheng, S.-I. (1956). *Theory of Combustion Instability in Liquid Propellant Rocket Motors*. Butterworths Scientific Publications.

Cumpsty, N. A. and Marble, F. E. (1977). The interaction of entropy fluctuations with turbine blade rows; a mechanism of turbojet engine noise. *Proc. R. Soc. Lond. Ser. A.*, 357:323–344.

Dopazo, C. (1975). Probability density function approach for a turbulent axisymmetric heated jet - Centerline evolution. *Phys. Fluids*, 18(June 1974):397–404.

Dopazo, C. (1979). Relaxation of initial probability density functions in the turbulent convection of scalar fields. *Phys. Fluids*, 22(1):20.

Dopazo, C. and O'Brien, E. E. (1974). Functional formulation of nonisothermal turbulent reactive flows. *Phys. Fluids*, 17(11):1968–1975.

Dowling, A. P. (1997). Nonlinear self-excited oscillations of a ducted flame. *J. Fluid Mech.*, 346:271–290.

Dowling, A. P. (1999). A kinematical model of ducted flame. *J. Fluid Mech.*, 294:51–72.

Dowling, A. P. and Morgans, A. S. (2005). Feedback control of combustion oscillations. *Annu. Rev. Fluid Mech.*, 37:151–182.

Duwig, C. and Fuchs, L. (2007). Large eddy simulation of vortex breakdown/flame interaction. *Phys. Fluids*, 19(7).

Engquist, B. and Majda, A. (1977a). Absorbing boundary conditions for acoustic and elastic wave equations. *Math. Comput*, 31:629–651.

Engquist, B. and Majda, A. (1977b). Absorbing boundary conditions for numerical simulation of waves (artificial boundaries/numerical approximation). *Appl. Math. Sci.*, 74(5):1765–1766.

Erlebacher, G., Hussaini, M. Y., Speziale, C. G., and Zang, T. A. (1992). Toward the large-eddy simulation of compressible turbulent flows. *J. Fluid Mech.*, 238:155–185.

Farisco, F., Panek, L., and Kok, J. B. (2017). Thermo-acoustic cross-talk between cans in a can-annular combustor. *Int. J. Spray Combust. Dyn.*, 9(4):452–469.

Fedina, E., Fureby, C., Bulat, G., and Meier, W. (2017). Assessment of Finite Rate Chemistry Large Eddy Simulation Combustion Models. *Flow, Turbul. Combust.*, 99(2):385–409.

Ferziger, J. H. and Peric, M. (2012). *Computational methods for fluid dynamics*. Springer Science & Business Media.

Fiorina, B., Vicquelin, R., Auzillon, P., Darabiha, N., Gicquel, O., and Veynante, D. (2010). A filtered tabulated chemistry model for LES of premixed combustion. *Combust. Flame*, 157(3):465–475.

Fleifil, M., Annaswamy, A. M., Ghoneim, Z. A., and Ghoniem, A. F. (1996). Response of a laminar premixed flame to flow oscillations: A kinematic model and thermoacoustic instability results. *Combust. Flame*, 106(4):487–510.

Franzelli, B., Riber, E., Gicquel, L. Y. M., and Poinsot, T. (2012). Large Eddy Simulation of combustion instabilities in a lean partially premixed swirled flame. *Combust. Flame*, 159(2):621–637.

Fredrich, D., Jones, W. P., and Marquis, A. J. (2019a). Application of the Eulerian subgrid Probability Density Function method in the Large Eddy Simulation of a partially premixed swirl flame. *Combust. Sci. Technol.*, 191(1):137–150.

Fredrich, D., Jones, W. P., and Marquis, A. J. (2019b). The stochastic fields method applied to a partially premixed swirl flame with wall heat transfer. *Combust. Flame*, 205:446–456.

Fredrich, D., Jones, W. P., and Marquis, A. J. (2020a). Self-excited thermo-acoustic and hydrodynamic instabilities in gas turbines. *Combust. Flame*. In review.

Fredrich, D., Jones, W. P., and Marquis, A. J. (2020b). Thermo-acoustic instabilities in the PRECCINSTA combustor investigated using a compressible LES-pdf approach. *Flow, Turbul. and Combust.* In review.

Fredrich, D., Jones, W. P., Marquis, A. J., and Bulat, G. (2020c). Prediction of longitudinal and azimuthal instabilities in a gas turbine combustor. *Proc. Combust. Inst.* In review.

Froud, D., O'Doherty, T., and Syred, N. (1995). Phase averaging of the precessing vortex core in a swirl burner under piloted and premixed combustion conditions. *Combust. Flame*, 100(3):2–11.

Fureby, C. (2000). A computational study of combustion instabilities due to vortex shedding. *Proc. Combust. Inst.*, 28(1):783–791.

Fureby, C. (2010). LES of a multi-burner annular gas turbine combustor. *Flow, Turbul. Combust.*, 84(3):543–564.

Gallot-Lavallée, S. (2018). *Liquid fuel spray atomisation, ignition and combustion dynamics*. PhD thesis, Imperial College London.

Galpin, J., Naudin, A., Vervisch, L., Angelberger, C., Colin, O., and Domingo, P. (2008). Large-eddy simulation of a fuel-lean premixed turbulent swirl-burner. *Combust. Flame*, 155(1-2):247–266.

Gao, F. and O'Brien, E. E. (1993). A large-eddy simulation scheme for turbulent reacting flows. *Phys. Fluids A*, 5(6):1282–1284.

Gardiner, C. (1985). *Handbook of Stochastic Methods*. Springer-Verlag, New York.

Ghani, A., Poinsot, T., Gicquel, L., and Staffelbach, G. (2015). LES of longitudinal and transverse self-excited combustion instabilities in a bluff-body stabilized turbulent premixed flame. *Combust. Flame*, 162(11):4075–4083.

Ghirardo, G., Di Giovine, C., Moeck, J. P., and Bothien, M. R. (2019). Thermoacoustics of can-annular combustors. *J. Eng. Gas Turbines Power*, 141(1):1–10.

Ghirardo, G. and Juniper, M. P. (2013). Azimuthal instabilities in annular combustors: Standing and spinning modes. *Proc. R. Soc. A Math. Phys. Eng. Sci.*, 469(2157).

Ghoniem, A. F., Park, S., Wachsman, A., Annaswamy, A., Wee, D., and Murat Altay, H. (2005). Mechanism of combustion dynamics in a backward-facing step stabilized premixed flame. *Proc. Combust. Inst.*, 30(2):1783–1790.

Giauque, A., Selle, L., Gicquel, L., Poinsot, T., Buechner, H., Kaufmann, P., and Krebs, W. (2005). System identification of a large-scale swirled partially premixed combustor using LES and measurements. *J. Turbul.*, 6(21):1–20.

Gicquel, L. Y., Staffelbach, G., and Poinsot, T. (2012). Large Eddy Simulations of gaseous flames in gas turbine combustion chambers. *Prog. Energy Combust. Sci.*, 38(6):782–817.

Gövert, S., Mira, D., Kok, J. B., Vázquez, M., and Houzeaux, G. (2018). The Effect of Partial Premixing and Heat Loss on the Reacting Flow Field Prediction of a Swirl Stabilized Gas Turbine Model Combustor. *Flow, Turbul. Combust.*, 100(2):503–534.

Guedot, L., Lartigue, G., and Moureau, V. (2015). Design of implicit high-order filters on unstructured grids for the identification of large-scale features in large-eddy simulation and application to a swirl burner. *Phys. Fluids*, 27(4):045107.

Han, X., Li, J., and Morgans, A. S. (2015). Prediction of combustion instability limit cycle oscillations by combining flame describing function simulations with a thermoacoustic network model. *Combust. Flame*, 162(10):3632–3647.

Hauser, M., Lorenz, M., and Sattelmayer, T. (2011). Influence of transversal acoustic excitation of the burner approach flow on the flame structure. *J. Eng. Gas Turbines Power*, 133:041501.

Hedstrom, G. (1979). Nonreflecting Boundary Conditions for Nonlinear Hyperbolic Systems. *J. Comput. Phys.*, 30:222–237.

Hermeth, S., Staffelbach, G., Gicquel, L. Y., Anisimov, V., Cirigliano, C., and Poinsot, T. (2014). Bistable swirled flames and influence on flame transfer functions. *Combust. Flame*, 161(1):184–196.

Hermeth, S., Staffelbach, G., Gicquel, L. Y. M., and Poinsot, T. (2013). LES evaluation of the effects of equivalence ratio fluctuations on the dynamic flame response in a real gas turbine combustion chamber. *Proc. Combust. Inst.*, 34(2):3165–3173.

Hoffmann, G. and Benocci, C. (1995). Approximate wall boundary conditions for large eddy simulations. In *Advances in Turbulence V*, pages 222–228. Springer.

Huang, Y. and Yang, V. (2009). Dynamics and stability of lean-premixed swirl-stabilized combustion. *Prog. Energy Combust. Sci.*, 35(4):293–364.

Jaberi, F. A., Colucci, P. J., James, S., Givi, P., and Pope, S. B. (1999). Filtered mass density function for large-eddy simulation of turbulent reacting flows. *J. Fluid Mech.*, 401:85–121.

Jaravel, T., Riber, E., Cuenot, B., and Bulat, G. (2017). Large Eddy Simulation of an industrial gas turbine combustor using reduced chemistry with accurate pollutant prediction. *Proc. Combust. Inst.*, 36(3):3817–3825.

Jones, W. P., di Mare, F., and Marquis, A. J. (2002). *LES-BOFFIN: Users Guide*. Tech. Rep., Imperial College London.

Jones, W. P., Marquis, A. J., and Prasad, V. N. (2012). LES of a turbulent premixed swirl burner using the Eulerian stochastic field method. *Combust. Flame*, 159(10):3079–3095.

Jones, W. P. and Navarro-Martinez, S. (2007). Large eddy simulation of autoignition with a subgrid probability density function method. *Combust. Flame*, 150(3):170–187.

Jones, W. P. and Prasad, V. N. (2010). Large Eddy Simulation of the Sandia Flame Series (D-F) using the Eulerian stochastic field method. *Combust. Flame*, 157(9):1621–1636.

Jones, W. P. and Prasad, V. N. (2011). LES-pdf simulation of a spark ignited turbulent methane jet. *Proc. Combust. Inst.*, 33(1):1355–1363.

Ju, Y., Guo, H., Maruta, K., and Liu, F. (1997). On the extinction limit and flammability limit of non-adiabatic stretched methane–air premixed flames. *J. Fluid Mech.*, 342(1):315–334.

Jurisch, M. (2016). *On the mechanics of oscillating flames*. PhD thesis, Imperial College London.

Kailasanath, K., Gardner, J. H., Oran, E. S., and Boris, J. P. (1991). Numerical simulations of unsteady reactive flows in a combustion chamber. *Combust. Flame*, 86(1-2):115–134.

Karlis, E., Hardalupas, Y., and Taylor, A. M. (2019a). Effects of inert fuel diluents on the dynamic state of a thermoacosutically unstable gas turbine combustor. In *AIAA Scitech 2019 Forum*, pages 1–20.

Karlis, E., Hardalupas, Y., Taylor, A. M., Rogerson, J., Sadasivuni, S., Stöhr, M., and Stopper, U. (2019b). Thermoacoustic phenomena in an industrial gas turbine combustor at two different mean pressures. In *AIAA Scitech 2019 Forum*, pages 1–17.

Kaufmann, P., Krebs, W., Valdes, R., and Wever, U. (2008). 3D thermoacoustic properties of single can and multi can combustor configurations. In *Proc. ASME Turbo Expo 2008*, pages 1–12.

Kelsall, G. and Troger, C. (2004). Prediction and control of combustion instabilities in industrial gas turbines. *Appl. Therm. Eng.*, 24(11-12):1571–1582.

Kim, K. T., Lee, J. G., Lee, H. J., Quay, B. D., and Santavicca, D. A. (2010a). Characterization of Forced Flame Response of Swirl-Stabilized Turbulent Lean-Premixed Flames in a Gas Turbine Combustor. *J. Eng. Gas Turbines Power*, 132(4):041502.

Kim, K. T., Lee, J. G., Quay, B. D., and Santavicca, D. A. (2010b). Response of partially premixed flames to acoustic velocity and equivalence ratio perturbations. *Combust. Flame*, 157(9):1731–1744.

Kloeden, P. E. and Platen, E. (1999). *Numerical Solution of Stochastic Differential Equations*. Springer-Verlag.

Komarek, T. and Polifke, W. (2010). Impact of Swirl Fluctuations on the Flame Response of a Perfectly Premixed Swirl Burner. *J. Eng. Gas Turbines Power*, 132(6):061503.

Kraus, C., Selle, L., and Poinsot, T. (2018). Coupling heat transfer and large eddy simulation for combustion instability prediction in a swirl burner. *Combust. Flame*, 191:239–251.

Kuo, K. K.-y. (1986). Principles of combustion. *Combust. Flame*, 73(3):337.

Laera, D., Schuller, T., Prieur, K., Durox, D., Camporeale, S. M., and Candel, S. (2017). Flame Describing Function analysis of spinning and standing modes in an annular combustor and comparison with experiments. *Combust. Flame*, 184:136–152.

Langella, I., Chen, Z. X., Swaminathan, N., and Sadasivuni, S. K. (2018). Large-eddy simulation of reacting flows in industrial gas turbine combustor. *J. Propuls. Power*, 34(5):1269–1284.

Lecocq, G., Richard, S., Colin, O., and Vervisch, L. (2011). Hybrid presumed pdf and flame surface density approaches for Large-Eddy Simulation of premixed turbulent combustion. Part 1: Formalism and simulation of a quasi-steady burner. *Combust. Flame*, 158(6):1201–1214.

Lefebvre, A. H. (1999). *Gas Turbine Combustion*. Taylor & Francis, 2nd edition.

Libby, P. A. and Williams, F. A. (1994). *Turbulent reacting flows*. Academic press.

Lieuwen, T. and Yang, V. (2005). *Combustion Instabilities in Gas Turbine Engines*, volume 210. Progress in Astronautics and Aeronautics.

Lieuwen, T. and Zinn, B. T. (1998). The role of equivalence ratio oscillations in driving combustion instabilities in low NOx gas turbines. *Symp. Combust.*, 27:1809–1816.

Lodato, G., Domingo, P., and Vervisch, L. (2008). Three-dimensional boundary conditions for direct and large-eddy simulation of compressible viscous flows. *J. Comput. Phys.*, 227(10):5105–5143.

Lourier, J. M., Stöhr, M., Noll, B., Werner, S., and Fiolitakis, A. (2017). Scale Adaptive Simulation of a thermoacoustic instability in a partially premixed lean swirl combustor. *Combust. Flame*, 183:343–357.

Lu, T. and Law, C. K. (2008). A criterion based on computational singular perturbation for the identification of quasi steady state species: A reduced mechanism for methane oxidation with NO chemistry. *Combust. Flame*, 154(4):761–774.

Lucca-Negro, O. and O'Doherty, T. (2001). Vortex breakdown: A review. *Prog. Energy Combust. Sci.*, 27(4):431–481.

Magri, L., Bauerheim, M., and Juniper, M. P. (2016). Stability analysis of thermo-acoustic nonlinear eigenproblems in annular combustors. Part I. Sensitivity. *J. Comput. Phys.*, 325:395–410.

Malanoski, M., Aguilar, M., Acharya, V., and Lieuwen, T. (2013). Dynamics of a transversely excited swirling, lifted flame part 1: Experiments and data analysis. In *Proc. ASME Turbo Expo 2013*, pages GT2013–95358.

Martin, C., Benoit, L., Nicoud, F., and Poinsot, T. (2004). Analysis of acoustic energy and modes in a turbulent swirled combustor. In *Cent. Turbul. Res. Proc. summer Progr.*, pages 377–394.

Mazur, M., Nygård, H. T., Dawson, J. R., and Worth, N. A. (2019). Characteristics of self-excited spinning azimuthal modes in an annular combustor with turbulent premixed bluff-body flames. *Proc. Combust. Inst.*, 37(4):5129–5136.

Meier, W., Weigand, P., Duan, X. R., and Giezendanner-Thoben, R. (2007). Detailed characterization of the dynamics of thermoacoustic pulsations in a lean premixed swirl flame. *Combust. Flame*, 150(1-2):2–26.

Menon, S. and Jou, W.-H. (1991). Large-eddy simulations of combustion instability in an axisymmetric ramjet combustor. *Combust. Sci. Technol.*, 75(1-3):53–72.

Mercier, R., Moureau, V., Veynante, D., and Fiorina, B. (2015). LES of turbulent combustion: On the consistency between flame and flow filter scales. *Proc. Combust. Inst.*, 35(2):1359–1366.

Méry, Y. (2017). Impact of heat release global fluctuations and flame motion on transverse acoustic wave stability. *Proc. Combust. Inst.*, 36(3):3889–3898.

Moeck, J. P., Bourgouin, J. F., Durox, D., Schuller, T., and Candel, S. (2012). Nonlinear interaction between a precessing vortex core and acoustic oscillations in a turbulent swirling flame. *Combust. Flame*, 159(8):2650–2668.

Moeck, J. P., Durox, D., Schuller, T., and Candel, S. (2019). Nonlinear thermoacoustic mode synchronization in annular combustors. *Proc. Combust. Inst.*, 37(4):5343–5350.

Monkewitz, P. A. (1988). A note on vortex shedding from axisymmetric bluff bodies. *J. Fluid Mech.*, 192:561–575.

Moon, K., Jegal, H., Gu, J., and Kim, K. T. (2019). Combustion-acoustic interactions through cross-talk area between adjacent model gas turbine combustors. *Combust. Flame*, 202:405–416.

Moureau, V., Domingo, P., and Vervisch, L. (2011). From Large-Eddy Simulation to Direct Numerical Simulation of a lean premixed swirl flame: Filtered laminar flame-PDF modeling. *Combust. Flame*, 158(7):1340–1357.

Mustata, R., Valiño, L., Jiménez, C., Jones, W. P., and Bondi, S. (2006). A probability density function Eulerian Monte Carlo field method for large eddy simulations: Application to a turbulent piloted methane/air diffusion flame (Sandia D). *Combust. Flame*, 145(1-2):88–104.

Noh, D. (2016). *A stochastic approach towards large eddy simulation of methanol/air spray flames*. PhD thesis, Imperial College London.

Noh, D., Karlis, E., Navarro-Martinez, S., Hardalupas, Y., Taylor, A. M. K. P., Fredrich, D., and Jones, W. P. (2019). Azimuthally-driven subharmonic thermoacoustic instabilities in a swirl-stabilised combustor. *Proc. Combust. Inst.*, 37(4):5333–5341.

Noiray, N., Durox, D., Schuller, T., and Candel, S. (2008). A unified framework for nonlinear combustion instability analysis based on the flame describing function. *J. Fluid Mech.*, 615:139–167.

Noiray, N. and Schuermans, B. (2013). On the dynamic nature of azimuthal thermoacoustic modes in annular gas turbine combustion chambers. *Proc. R. Soc. A Math. Phys. Eng. Sci.*, 469(2151).

Oberleithner, K., Stöhr, M., Im, S. H., Arndt, C. M., and Steinberg, A. M. (2015). Formation and flame-induced suppression of the precessing vortex core in a swirl combustor: Experiments and linear stability analysis. *Combust. Flame*, 162(8):3100–3114.

O'Connor, J., Acharya, V., and Lieuwen, T. (2015). Transverse combustion instabilities: Acoustic, fluid mechanic, and flame processes. *Prog. Energy Combust. Sci.*, 49:1–39.

Palies, P., Durox, D., Schuller, T., and Candel, S. (2010). The combined dynamics of swirler and turbulent premixed swirling flames. *Combust. Flame*, 157(9):1698–1717.

Palies, P., Durox, D., Schuller, T., and Candel, S. (2011a). Acoustic-convective mode conversion in an aerofoil cascade. *J. Fluid Mech.*, 672:545–569.

Palies, P., Ilak, M., and Cheng, R. (2017). Transient and limit cycle combustion dynamics analysis of turbulent premixed swirling flames. *J. Fluid Mech.*, 830:681–707.

Palies, P., Schuller, T., Durox, D., Gicquel, L. Y., and Candel, S. (2011b). Acoustically perturbed turbulent premixed swirling flames. *Phys. Fluids*, 23(3):037101.

Pankiewitz, C. and Sattelmayer, T. (2002). Time Domain Simulation of Combustion Instabilities in Annular Combustors. In *Proc. ASME Turbo Expo 2002*, pages GT–2002–30063.

Paschereit, C. O., Gutmark, E., and Weisenstein, W. (2000). Excitation of thermoacoustic instabilities by interaction of acoustics and unstable swirling flow. *AIAA J.*, 38(6):1025–1034.

Paschereit, C. O., Schuermans, B., Polifke, W., and Mattson, O. (2002). Measurement of transfer matrices and source terms of premixed flames. *J. Eng. Gas Turbines Power*, 124(2):239–247.

Peters, N. (2000). *Turbulent Combustion.* Cambridge University Press.

Piomelli, U. and Balaras, E. (2002). Wall layer models for large eddy simulation. *Annu. Rev. Fluid Mech.*, 34:349–374.

Piomelli, U. and Liu, J. (1995). Large-eddy simulation of rotating channel flows using a localized dynamic model. *Phys. Fluids*, 7(4):839–848.

Pitsch, H. (2006). Large-Eddy Simulation of Turbulent Combustion. *Annu. Rev. Fluid Mech.*, 38(1):453–482.

Poinsot, T. (2017). Prediction and control of combustion instabilities in real engines. *Proc. Combust. Inst.*, 36(1):1–28.

Poinsot, T. and Veynante, D. (2005). *Theoretical and Numerical Combustion.* RT Edwards, Inc., 2nd edition.

Poinsot, T. J. and Lele, S. K. (1992). Boundary conditions for direct simulations of compressible viscous flows. *J. Comput. Phys.*, 101(1):104–129.

Poinsot, T. J., Trouve, A. C., Veynante, D. P., Candel, S. M., and Esposito, E. J. (1987). Vortex-driven acoustically coupled combustion instabilities. *J. Fluid Mech.*, 177:265–292.

Polifke, W., Poncet, A., Paschereit, C. O., and Döbbeling, K. (2001). Reconstruction of acoustic transfer matrices by instationary computational fluid dynamics. *J. Sound Vib.*, 245(3):483–510.

Prasad, V. N. (2011). *Large eddy simulation of partially premixed turbulent combustion*. PhD thesis, Imperial College London.

Prasad, V. N., Juddoo, M., Kourmatzis, A., and Masri, A. R. (2014). Investigation of lifted flame propagation under pulsing conditions using high-speed OH-LIF and LES. *Flow, Turbul. Combust.*, 93(3):425–437.

Prieur, K., Durox, D., Schuller, T., and Candel, S. (2017). A hysteresis phenomenon leading to spinning or standing azimuthal instabilities in an annular combustor. *Combust. Flame*, 175:283–291.

Ranjan, R., Ebi, D. F., and Clemens, N. T. (2019). Role of inertial forces in flame-flow interaction during premixed swirl flame flashback. *Proc. Combust. Inst.*, 37(4):5155–5162.

Rayleigh, J. W. (1877). *The Theory of Sound*. Macmillan & Co, London.

Rayleigh, L. (1878). The explanation of certain acoustic phenomena. *Nature July 18*, pages 319–321.

Raynaud, F., Eggels, R., Staufer, M., Sadiki, A., and Janicka, J. (2015). Towards unsteady simulation of combustor-turbine interaction using an integrated approach. In *Proc. ASME Turbo Expo 2015 Turbine Tech. Conf. Expo.*, pages GT2015–42110.

Rhie, C. M. and Chow, W. L. (1983). Numerical study of the turbulent flow past an airfoil with trailing edge separation. *AIAA J.*, 21(11):1525–1532.

Roux, S., Lartigue, G., Poinsot, T., Meier, U., and Bérat, C. (2005). Studies of mean and unsteady flow in a swirled combustor using experiments, acoustic analysis, and large eddy simulations. *Combust. Flame*, 141(1-2):40–54.

Rudy, D. H. and Strikwerda, J. C. (1980). A nonreflecting outflow boundary condition for subsonic navier-stokes calculations. *J. Comput. Phys.*, 36(1):55–70.

Rudy, D. H. and Strikwerda, J. C. (1981). Boundary conditions for subsonic compressible Navier-Stokes calculations. *Comput. Fluids*, 9(3):327–338.

Sabel'nikov, V. and Soulard, O. (2005). Rapidly decorrelating velocity-field model as a tool for solving one-point Fokker-Planck equations for probability density functions of turbulent reactive scalars. *Phys. Rev. E*, 72(1):1–22.

Sadasivuni, S., Bulat, G., Sanderson, V., and Swaminathan, N. (2012). Application of Scalar Dissipation Rate Model to Siemens DLE Combustors. In *Proc. ASME Turbo Expo 2012*, pages 1–10.

Sajben, M. and Said, H. (2001). Acoustic-Wave/Blade-Row Interactions Establish Boundary Conditions for Unsteady Inlet Flows. *J. Propuls. Power*, 17(5):1090–1099.

Saurabh, A. and Paschereit, C. O. (2017). Dynamics of premixed swirl flames under the influence of transverse acoustic fluctuations. *Combust. Flame*, 182:298–312.

Schmidt, H. and Schumann, U. (1989). Coherent structure of the convective boundary layer derived from large-eddy simulations. *J. Fluid Mech.*, 200:511–562.

Schmitt, P., Poinsot, T., Schuermans, B., and Geigle, K. P. (2007). Large-eddy simulation and experimental study of heat transfer, nitric oxide emissions and combustion instability in a swirled turbulent high-pressure burner. *J. Fluid Mech.*, 570:17–46.

Schönborn, A., Sayad, P., and Klingmann, J. (2014). Influence of precessing vortex core on flame flashback in swirling hydrogen flames. *Int. J. Hydrogen Energy*, 39(35):20233–20241.

Schuller, T., Durox, D., and Candel, S. (2003). A unified model for the prediction of laminar flame transfer functions: Comparisons between conical and V-flame dynamics. *Combust. Flame*, 134(1-2):21–34.

Schulz, O., Doll, U., Ebi, D., Droujko, J., Bourquard, C., and Noiray, N. (2019). Thermoacoustic instability in a sequential combustor: Large eddy simulation and experiments. *Proc. Combust. Inst.*, 37(4):5325–5332.

Selle, L., Benoit, L., Poinsot, T., Nicoud, F., and Krebs, W. (2006). Joint use of compressible large-eddy simulation and Helmholtz solvers for the analysis of rotating modes in an industrial swirled burner. *Combust. Flame*, 145(1-2):194–205.

Selle, L., Lartigue, G., Poinsot, T., Koch, R., Schildmacher, K. U., Krebs, W., Prade, B., Kaufmann, P., and Veynante, D. (2004). Compressible large eddy simulation of turbulent combustion in complex geometry on unstructured meshes. *Combust. Flame*, 137(4):489–505.

Smagorinsky, J. (1963). General Circulation Experiments with the Primitive Equations. *Mon. Weather Rev.*, 91(3):99–164.

Smith, T., Emerson, B., Proscia, W., and Lieuwen, T. (2018). Role of induced axial acoustics in transverse acoustic flame response. *Combust. Flame*, 195:140–150.

Staffelbach, G., Gicquel, L., Boudier, G., and Poinsot, T. (2009). Large Eddy Simulation of self excited azimuthal modes in annular combustors. *Proc. Combust. Inst.*, 32(2):2909–2916.

Steinberg, A. M., Arndt, C. M., and Meier, W. (2013). Parametric study of vortex structures and their dynamics in swirl-stabilized combustion. *Proc. Combust. Inst.*, 34(2):3117–3125.

Steinberg, A. M., Boxx, I., Arndt, C. M., Frank, J. H., and Meier, W. (2011). Experimental study of flame-hole reignition mechanisms in a turbulent non-premixed jet flame using sustained multi-kHz PIV and crossed-plane OH PLIF. *Proc. Combust. Inst.*, 33(1):1663–1672.

Steinberg, A. M., Boxx, I., Stöhr, M., Carter, C. D., and Meier, W. (2010). Flow-flame interactions causing acoustically coupled heat release fluctuations in a thermo-acoustically unstable gas turbine model combustor. *Combust. Flame*, 157(12):2250–2266.

Sterling, J. and Zukoski, E. (1987). Longitudinal mode combustion instabilities in a dump combustor. In *25th AIAA Aerosp. Sci. Meet.*, page 0220. American Institute of Aeronautics and Astronautics.

Stöhr, M., Boxx, I., Carter, C., and Meier, W. (2011). Dynamics of lean blowout of a swirl-stabilized flame in a gas turbine model combustor. *Proc. Combust. Inst.*, 33(2):2953–2960.

Stöhr, M., Oberleithner, K., Sieber, M., Yin, Z., and Meier, W. (2018). Experimental Study of Transient Mechanisms of Bistable Flame Shape Transitions in a Swirl Combustor. *J. Eng. Gas Turbines Power*, 140:011503.

Stöhr, M., Yin, Z., and Meier, W. (2017). Interaction between velocity fluctuations and equivalence ratio fluctuations during thermoacoustic oscillations in a partially premixed swirl combustor. *Proc. Combust. Inst.*, 36(3):3907–3915.

Stopper, U., Aigner, M., Ax, H., Meier, W., Sadanandan, R., Stöhr, M., and Bonaldo, A. (2010). PIV, 2D-LIF and 1D-Raman measurements of flow field, composition and temperature in premixed gas turbine flames. *Exp. Therm. Fluid Sci.*, 34(3):396–403.

Stopper, U., Aigner, M., Meier, W., Sadanandan, R., Stöhr, M., and Kim, I. S. (2009). Flow Field and Combustion Characterization of Premixed Gas Turbine Flames by Planar Laser Techniques. *J. Eng. Gas Turbines Power*, 131(2):021504.

Stopper, U., Meier, W., Sadanandan, R., Stöhr, M., Aigner, M., and Bulat, G. (2013). Experimental study of industrial gas turbine flames including quantification of pressure influence on flow field, fuel/air premixing and flame shape. *Combust. Flame*, 160(10):2103–2118.

Stow, S. R. and Dowling, A. P. (2009). A time-domain network model for nonlinear thermoacoustic oscillations. *J. Eng. Gas Turbines Power*, 131(3).

Straub, D. L. and Richards, G. A. (1999). Effect of Axial Swirl Vane Location on Combustion Dynamics. In *Vol. 2 Coal, Biomass Altern. Fuels; Combust. Fuels; Oil Gas Appl. Cycle Innov.*, page V002T02A014. ASME.

Sung, C. J., Law, C. K., and Chen, J. Y. (2001). Augmented reduced mechanisms for NO emission in methane oxidation. *Combust. Flame*, 125(1-2):906–919.

Syred, N. (2006). A review of oscillation mechanisms and the role of the precessing vortex core (PVC) in swirl combustion systems. *Prog. Energy Combust. Sci.*, 32(2):93–161.

Tachibana, S., Saito, K., Yamamoto, T., Makida, M., Kitano, T., and Kurose, R. (2015). Experimental and numerical investigation of thermo-acoustic instability in a liquid-fuel aero-engine combustor at elevated pressure: Validity of large-eddy simulation of spray combustion. *Combust. Flame*, 162(6):2621–2637.

Temme, J. E., Allison, P. M., and Driscoll, J. F. (2014). Combustion instability of a lean premixed prevaporized gas turbine combustor studied using phase-averaged PIV. *Combust. Flame*, 161(4):958–970.

Terhaar, S., Oberleithner, K., and Paschereit, C. O. (2015). Key parameters governing the precessing vortex core in reacting flows: An experimental and analytical study. *Proc. Combust. Inst.*, 35(3):3347–3354.

Thompson, K. W. (1987). Time dependent boundary conditions for hyperbolic systems. *J. Comput. Phys.*, 68(1):1–24.

Turns, S. R. (1996). *An introduction to combustion: concepts and applications*. McGraw-hill.

Valiño, L. (1998). A Field Monte Carlo formulation for calculating the probability density function of a single scalar in a turbulent flow. *Flow, Turbul. Combust.*, 60(2):157–172.

Venkataraman, K. K., Preston, L. H., Simons, D. W., Lee, B. J., Lee, J. G., and Santavicca, D. A. (1999). Mechanism of Combustion Instability in a Lean Premixed Dump Combustor. *J. Propuls. Power*, 15(6):909–918.

Versteeg, H. K. and Malalasekera, W. (2007). *An introduction to computational fluid dynamics: the finite volume method*. Pearson education.

Veynante, D. and Moureau, V. (2015). Analysis of dynamic models for large eddy simulations of turbulent premixed combustion. *Combust. Flame*, 162(12):4622–4642.

Volpiani, P. S., Schmitt, T., and Veynante, D. (2017). Large eddy simulation of a turbulent swirling premixed flame coupling the TFLES model with a dynamic wrinkling formulation. *Combust. Flame*, 180:124–135.

Wang, P., Fröhlich, J., Maas, U., He, Z., and Wang, C. (2016). A detailed comparison of two sub-grid scale combustion models via large eddy simulation of the PRECCINSTA gas turbine model combustor. *Combust. Flame*, 164:329–345.

Wang, S. and Yang, V. (2005). Unsteady flow evolution in swirl injectors with radial entry. II. External excitations. *Phys. Fluids*, 17(4).

Wang, S., Yang, V., Hsiao, G., Hsieh, S.-Y., and Mongia, H. C. (2007). Large-eddy simulations of gas-turbine swirl injector flow dynamics. *J. Fluid Mech.*, 583:99.

Warnatz, J., Mass, U., and Dibble, R. (2001). *Combustion*. Springer-Verlag Berlin Heidelberg, 3rd edition.

Wesseling, P. (2009). *Principles of computational fluid dynamics*, volume 29. Springer Science & Business Media.

Williams, F. A. (2018). *Combustion theory*. CRC Press.

Wolf, P., Staffelbach, G., Gicquel, L. Y., Müller, J. D., and Poinsot, T. (2012). Acoustic and Large Eddy Simulation studies of azimuthal modes in annular combustion chambers. *Combust. Flame*, 159(11):3398–3413.

Worth, N. A. and Dawson, J. R. (2013). Self-excited circumferential instabilities in a model annular gas turbine combustor: Global flame dynamics. *Proc. Combust. Inst.*, 34(2):3127–3134.

Xia, Y. (2019). *Prediction of thermoacoustic instability in gas turbine combustors*. PhD thesis, Imperial College London.

Xia, Y., Duran, I., Morgans, A. S., and Han, X. (2018a). Dispersion of Entropy Perturbations Transporting through an Industrial Gas Turbine Combustor. *Flow, Turbul. Combust.*, 100(2):481–502.

Xia, Y., Laera, D., Jones, W. P., and Morgans, A. S. (2019). Numerical Prediction of the Flame Describing Function and Thermoacoustic Limit Cycle for a Pressurized Gas Turbine Combustor. *Combust. Sci. Technol.*, 0(0):1–24.

Xia, Y., Laera, D., Morgans, A. S., Jones, W. P., and Rogerson, J. W. (2018b). Thermoacoustic Limit Cycle Predictions of a Pressurised Longitudinal Industrial Gas Turbine Combustor. In *Proc. ASME Turbo Expo 2018*, pages 1–14.

Xia, Y., Morgans, A. S., Jones, W. P., Rogerson, J., Bulat, G., and Han, X. (2017). Predicting Thermoacoustic Instability in an Industrial Gas Turbine Combustor: Combining a Low Order Network Model with Flame LES. In *Proc. ASME Turbo Expo 2017 Turbomach. Tech. Conf. Expo.*, pages 1–12.

Yamashita, H., Shimada, M., and Takeno, T. (1996). A numerical study on flame stability at the transition point of jet diffusion flames. *Symp. Combust.*, 26(1):27–34.

Yin, Z., Nau, P., and Meier, W. (2017). Responses of combustor surface temperature to flame shape transitions in a turbulent bi-stable swirl flame. *Exp. Therm. Fluid Sci.*, 82:50–57.

Yoo, C. S. and Im, H. G. (2007). Characteristic boundary conditions for simulations of compressible reacting flows with multi-dimensional, viscous and reaction effects. *Combust. Theory Model.*, 11(2):259–286.

Yoo, C. S., Wang, Y., Trouvé, A., and Im, H. G. (2005). Characteristic boundary conditions for direct simulations of turbulent counterflow flames. *Combust. Theory Model.*, 9(4):617–646.

Yu, K. H., Trouvé, A., and Daily, J. W. (1991). Low-frequency pressure oscillations in a model ramjet combustor. *J. Fluid Mech.*, 232(1):47–72.

Zellhuber, M., Schwing, J., Schuermans, B., Sattelmayer, T., and Polifke, W. (2014). Experimental and numerical investigation of thermoacoustic sources related to high-frequency instabilities. *Int. J. Spray Combust. Dyn.*, 6(1):1–34.

Zhang, R., Boxx, I., Meier, W., and Slabaugh, C. D. (2019). Coupled interactions of a helical precessing vortex core and the central recirculation bubble in a swirl flame at elevated power density. *Combust. Flame*, 202:119–131.

Appendix A

Solution algorithm

A.1 Preliminaries

If the spatial derivatives in the continuity, Navier-Stokes and stochastic fields equations are replaced by discrete approximations, then Eqs. (2.16), (2.17) and (2.29) can be written in the form:

$$\frac{\underline{\rho}^{n+1} - \underline{\rho}^{n}}{\delta t} + \nabla_d(\underline{\rho}\underline{u}) = 0 \tag{A.1}$$

$$\frac{\underline{u}^{n+1} - \underline{u}^{n}}{\delta t} = \underline{A}_u(\underline{\rho},\underline{u})\underline{u} + \underline{b}_u(\underline{u}) - \frac{1}{\rho}\nabla_d(\underline{p}) \tag{A.2}$$

$$\frac{\underline{\phi}^{n+1} - \underline{\phi}^{n}}{\delta t} = \underline{A}_\phi(\underline{\rho},\underline{u})\underline{\phi} + \underline{b}_\phi(\underline{\phi}); \quad 1 \leq \alpha \leq N_s \tag{A.3}$$

where $\nabla_d(\;)$ is the discrete form of the divergence or gradient operator. If $\underline{\phi} = h_t$, then $\underline{b}_\phi = \frac{\partial p}{\partial t}$.

The Navier-Stokes equation and stochastic fields species equations can then be approximately 'factored' to yield:

$$\underline{u}^{n+1}(\underline{I} - \underline{A}_u\delta t) = \underline{u}^n + \underline{b}_u\delta t - \frac{1}{\rho}\nabla_d(p^n)\delta t - (\underline{I} - \underline{A}_u\delta t)\frac{1}{\rho}\nabla_d(p^{n+1} - p^n)\delta t \tag{A.4}$$

$$\underline{\phi}^{n+1}(\underline{I} - \underline{A}_\phi\delta t) = \underline{\phi}^n + (\underline{I} - \underline{A}_\phi\delta t)\underline{b}_\phi\delta t; \quad 1 \leq \alpha \leq N_{sp} \tag{A.5}$$

The solution to Eq. (A.4) yields:

$$\underline{u}^{n+1} + \mathcal{O}(\delta t^2) \times \nabla_d(p^{n+1} - p^n) \tag{A.6}$$

and thus $\underline{u}^{n+1} + \mathcal{O}(\delta t^3)$, while Eq. (A.5) gives $\underline{\phi}^{n+1} + \mathcal{O}(\delta t^2)$.

A.2 Algorithm

Step (I) Stochastic fields equations:

Solve the discrete form of the stochastic fields species equations (A.5), using $\underline{\rho}^n$ and $\underline{u}^n$, as follows:

$$\begin{aligned} \hat{\underline{\phi}}^{n+1} &= \underline{\phi}^n + \underline{b}_\phi(\hat{\underline{\phi}}^{n+1})\delta t \\ (\underline{I} - \underline{A}_\phi \delta t)\underline{\phi}^{n+1} &= \hat{\underline{\phi}}^{n+1}; \quad 1 \leq \alpha \leq N_{sp} \end{aligned} \tag{A.7}$$

Solve the stochastic fields equation for total enthalpy:

$$(\underline{I} - \underline{A}_\phi \delta t)\underline{h}_t^{n+1} = \underline{h}_t^n + \frac{\partial \underline{p}^n}{\partial t}\delta t \tag{A.8}$$

The solution to Eqs. (A.7) and (A.8) can be used to obtain $\hat{\mathrm{T}}^{n+1}$ and $\underline{\rho}^* = \underline{\rho}(\hat{\mathrm{T}}^{n+1}, \hat{n}_\alpha^{n+1}, p^n)$ and $\underline{u}^*$ is set equal to $\underline{u}^n$.

Step (II) Navier-Stokes equations:

The approximate factorisation (A.4) can be complemented as follows:

$$\frac{\hat{\underline{u}}^{n+1} - \underline{u}^n}{\delta t} = \underline{A}_u(\underline{\rho}^*, \underline{u}^*)\hat{\underline{u}}^{n+1/2} + \underline{b}_u(\underline{u}^*) - \frac{1}{\rho^*}\nabla_d(p^n) \tag{A.9}$$

$$\frac{\underline{u}^{n+1} - \hat{\underline{u}}^{n+1}}{\delta t} = -\frac{1}{\rho^*}\nabla_d(p^{n+1} - p^n) \tag{A.10}$$

Eq. (A.10) can then be used to obtain:

$$\underline{u}^{n+1/2} = \hat{\underline{u}}^{n+1/2} - \frac{1}{2\rho^*}\nabla_d(p^{n+1} - p^n)\delta t \tag{A.11}$$

Step (III) Continuity equation:

The continuity equation may be written as:

$$\frac{\rho^{n+1} - \rho^n}{\delta t} + \frac{\partial}{\partial x_i}\left(\rho^{n+1/2}\underline{u}^{n+1/2}\right) = 0 \tag{A.12}$$

If the pressure dependence of the density is taken into account, the densities in Eq. (A.12) can be obtained from:

$$\begin{aligned} \rho^{n+1} &= \rho^* + \frac{\partial \rho}{\partial p}(p^{n+1} - p^n) \\ \rho^{n+1/2} &= \rho^* + \frac{1}{2}\frac{\partial \rho}{\partial p}(p^{n+1} - p^n) \end{aligned} \tag{A.13}$$

On substitution of Eqs. (A.11) and (A.13) into the continuity equation (A.12) and with the neglect of the second order terms $(p^{n+1}-p^n)\times(u^{n+1/2}-\hat{u}^{n+1/2})$ the following may be obtained:

$$\frac{\partial\rho}{\partial p}\frac{\underline{p}'}{\delta t}+\frac{1}{2}\frac{\partial}{\partial x_i}\left\{\underline{\hat{u}}^{n+1/2}\frac{\partial\rho}{\partial p}\underline{p}'-\nabla_d(\underline{p}')\delta t\right\}=-\left[\frac{\underline{\rho}^*-\underline{\rho}^n}{\delta t}+\frac{\partial}{\partial x_i}\left(\rho^*\hat{u}_i^{n+1/2}\right)\right] \tag{A.14}$$

where $p'\equiv p^{n+1}-p^n$.

On solution of Eq. (A.14) the pressure and density can be updated, viz: $p^{n+1}=p^n+p'$ and $\rho^{n+1}=\rho^*+\frac{\partial\rho}{\partial p}p'$. Finally set:

$$\begin{aligned}\underline{\rho}^*&=1/2(\rho^{n+1}+\rho^n)\\ \underline{u}^*&=1/2(\underline{u}^{n+1}+\underline{u}^n)\end{aligned} \tag{A.15}$$

Repeat Steps (II) to (III) once.

The accuracy of $\underline{\rho}^{n+1},\underline{u}^{n+1}\sim\mathcal{O}(\delta t^3)$, i.e. second order accuracy for pdes.